INTERNATIONAL JOURNAL FOR NUMERICAL METHODS IN ENGINEERING
Int. J. Numer. Meth. Engng 2000; **00**:1–6 *Prepared using* nmeauth.cls *[Version: 2002/09/18 v2.02]*

Computation of Upper and Lower Bounds in Limit Analysis using Second-order Cone Programming and Mesh Adaptivity

H. Ciria [1], J. Peraire[1]*and J. Bonet [2]

[1] *Aerospace Computational Design Laboratory, Department of Aeronautics, MIT, Cambridge, MA 02139, USA.*
[2] *Civil & Computational Engineering Centre, School of Engineering, University of Wales, Swansea, SA2 8PP, UK.*

SUMMARY

An efficient procedure to compute strict upper and lower bounds for the exact collapse multiplier in limit analysis is presented, with a formulation that explicitly considers the exact convex yield condition. The approach consists of two main steps. First, the continuous problem, under the form of the static principle of limit analysis, is discretized twice (one per bound) using particularly chosen finite element spaces for the stresses and velocities that guarantee the attainment of an upper or a lower bound. The second step consists of solving the resulting discrete nonlinear optimization problems. These are reformulated as second-order cone programs, which allows for the use of primal-dual interior point methods that optimally exploit the convexity and duality properties of the limit analysis model. To benefit from the fact that collapse mechanisms are typically highly localized, a novel method for adaptive meshing is introduced. The method first decomposes the total bound gap as the sum of positive contributions from each element in the mesh and, then refines those elements with higher contributions. The efficiency of the methodology is illustrated with applications in plane stress and plane strain problems. Copyright © 2000 John Wiley & Sons, Ltd.

KEY WORDS: limit analysis; bounds; conic programming; mesh adaptivity; finite elements

1. INTRODUCTION

Limit analysis is relevant in many practical engineering areas such as the design of mechanical structures or the analysis of soil mechanics. Assuming a rigid, perfectly-plastic solid subject to a static load distribution, the problem of limit analysis consists of finding the minimum multiple of this load distribution that will cause the body to collapse. This *collapse multiplier* results from solving an infinite dimensional saddle point problem, where the internal work rate is maximized over an admissible convex set of stresses -defined by a yield condition-

*Correspondence to: peraire@mit.edu

Contract/grant sponsor: Singapore-MIT Alliance and DARPA-AFOSR; contract/grant number: F49620-03-1-0439

Received XXXXXX
Revised XXXXXX

in equilibrium with the applied loads and minimized over the linear space of kinematically admissible velocities for which the external work rate equals unity. This saddle point problem embeds the well-known convex (and equivalent) static and kinematic principles of limit analysis [10]. The presence of the yield condition introduces nonlinearity in the problem, which represents an important difficulty.

Traditionally, the way to overcome this difficulty has been to linearize the convex yield condition, thereby obtaining a polyhedral approximation to the yield surface. With this linearization, first introduced in [24], the resulting problem reduces to a classical linear program (LP). Initially, the LP was solved using the Simplex method [2, 9, 10] and, more recently, using Interior Point Methods (IPM) [4, 13]. The first successful attempts to solve for the exact convex yield condition on fine grids were reported in [6], where the kinematic principle was discretized and then formulated as a Minimization of Sum of Norms (MSN) subject to a linear constraint. Finally, the discrete problem was solved extending the ideas of IPMs for LP to the MSN. The approach, however, required the use of very cumbersome divergence-free elements when dealing with incompressible problems. This was overcome in [12], by simultaneously approximating the static and kinematic principles with a discrete duality problem that was solved using the method reported in [5]. This work was further improved in [14], by introducing automatic mesh refinement and using the primal-dual IPM developed in [7]. Unfortunately, the refinement strategy did not rely on rigorous local error measures but in heuristic estimates, thereby limiting its performance. A common feature of the above-mentioned works, [6, 12, 14], is that they only provide approximations to the collapse multiplier, but do not yield strict bounds. In [22, 23], on the other hand, lower and upper bounds of the collapse multiplier are computed for soil mechanics problems on uniform meshes, using linear finite elements and a nonlinear two-stage, quasi-Newton optimization algorithm. The method does not require the linearization of the yield condition, but can only handle smooth yield surfaces. Duality is not exploited and the solution process is not unified, since the upper and lower bounds are obtained by different versions of the quasi-Newton method. A new approach to obtain lower bounds is presented in [19]. It uses an IPM that exploits convexity and duality, and no particular finite element discretization or yield criterion is required. This basic approach has been more recently extended to the computation of upper bounds in [20]. A similar approach has been followed in [25] and [26] using simplex elements.

The main objective of the present work is to devise a unified and efficient method to compute upper and lower bounds, for the exact convex yield condition, using an approach that incorporates the methods presented in [19], [20], [25] and [26]. The convex nature of the limit analysis problem is exploited by solving the resulting optimization problems using standard conic programming (primal-dual) interior point algorithms. This guarantees efficiency in the solution process and global convergence to the optimal solutions. More importantly, the unified evaluation of upper and lowers bounds in this work makes it possible to derive rigorous mesh adaptive procedures, based on local error measures. These measures are based on a decomposition of the difference between the upper and lower bounds, the bound gap, into positive local contributions. Areas which contribute significantly to the bound gap can then be identified and refined. The work presented here expands on the earlier results presented in [16] and [15].

2. THE LIMIT ANALYSIS PROBLEM. DUALITY AND EXACT BOUNDS

In this section, the main concepts of limit analysis, as well as its mathematical description and main results are introduced. For its simplicity and ease of interpretation, the notation adopted corresponds with that used in [10, 11].

2.1. Notation and basic concepts

Let Ω denote the domain of study and $\partial\Omega$ its boundary, which consists of a Neumann portion Γ^N and a Dirichlet part Γ^D, so that $\partial\Omega = \Gamma^N \cup \Gamma^D$. Recall that limit analysis assumes a rigid, perfectly-plastic material subject to a fixed load distribution (consisting of both surface and volume forces), and aims at computing the minimum multiple (collapse multiplier) of this load distribution that causes the collapse of the body. The work rate of the external loads (*external work rate*) associated with a velocity or plastic flow $\mathbf{u} = \mathbf{u}(\mathbf{x})$ is given by the following linear functional

$$F(\mathbf{u}) = \int_\Omega \mathbf{f} \cdot \mathbf{u}\ dV + \int_{\Gamma^N} \mathbf{g} \cdot \mathbf{u}\ dS, \tag{1}$$

where $\mathbf{f}$ denotes the volume forces and $\mathbf{g}$, the surface forces acting on Γ^N. The internal work rate associated to the stress field $\boldsymbol{\sigma} = \boldsymbol{\sigma}(\mathbf{x})$ and the velocity $\mathbf{u}$ is given by the bilinear form

$$a(\boldsymbol{\sigma}, \mathbf{u}) = \int_\Omega \sum_{i,j} \sigma_{ij}\varepsilon_{ij}(\mathbf{u})\ dV = \int_\Omega \sum_{i,j} \sigma_{ij} \frac{\partial u_i}{\partial x_j}\ dV, \tag{2}$$

where σ_{ij} and ε_{ij} denote the components of the stress and strain tensors in the $x_i,\ i = 1:3$, cartesian coordinates.

Notice that the plastic flow $\mathbf{u}$ must belong to an appropriate space $Y \equiv Y(\Omega)$ of kinematically admissible velocity fields. Likewise, the stress field $\boldsymbol{\sigma}$ is restricted to an appropriate space of symmetric stress tensors $X \equiv X(\Omega)$. The mathematical requirements on Y and X can be found in [11].

The equilibrium equation can now be expressed as the principle of virtual work:

$$a(\boldsymbol{\sigma}, \mathbf{u}) = F(\mathbf{u}), \quad \forall \mathbf{u} \in Y. \tag{3}$$

Moreover, the yield condition imposes the stress tensor $\boldsymbol{\sigma}$ to belong to a convex set[†] $B(\mathbf{x})$ of admissible stresses for the material:

$$\boldsymbol{\sigma}(\mathbf{x}) \in B(\mathbf{x}), \quad \forall \mathbf{x} \in \Omega. \tag{4}$$

To simplify the notation, the material will be assumed to be homogeneous, so that $B(\mathbf{x})$ is independent of $\mathbf{x}$ and can be denoted by B. The computational treatment of the limit analysis

[†]The set of admissible stresses, $B(\mathbf{x})$, must verify the following properties to guarantee that the collapse state is well defined:

1. $\exists\ \epsilon > 0$ for which $\sum_{ij} |\sigma_{ij}| \leq \epsilon \Rightarrow \boldsymbol{\sigma} \in B(\mathbf{x})$ (the null stress tensor lays in the strict interior of $B(\mathbf{x})$)
2. $B(\mathbf{x})$ is a convex subset of the space of stress tensors (necessary by physical assumptions)
3. $B(\mathbf{x})$ is a closed subset (any limit of admissible stresses is itself admissible)

problem presented here exploits the convexity properties of B and requires, also, that B can be expressed in the generic form

$$B = \{\boldsymbol{\sigma} \in X \mid \sum_k f_k^2(\sigma_{ij}) \leq f_0^2(\sigma_{ij}, q)\}, \tag{5}$$

where f_k and f_0 are affine functions of their arguments and q is a constant depending on the material properties. For instance, this structure is embedded in the von Mises (three-dimensional) yield condition, given by

$$B_{VM} = \{\boldsymbol{\sigma} \in X \mid (\sigma_{11}-\sigma_{22})^2 + (\sigma_{22}-\sigma_{33})^2 + (\sigma_{33}-\sigma_{11})^2 + 6\sigma_{12}^2 + 6\sigma_{23}^2 + 6\sigma_{13}^2 \leq 2\sigma_y^2\}, \tag{6}$$

where σ_y denotes the yield stress in simple tension and can be interpreted as the generic constant q. Notice that the yield set B might be unbounded, as is the case in the above example (any hydrostatic stress tensor satisfies the above inequality). The restriction of the von Mises yield condition to two-dimensional cases (either plane stress or plane strain) also satisfies the structure (5). In plane strain, the same is valid for the Tresca (T), Mohr-Coulomb (MC) or Drucker-Prager (DP) models, given by

$$B_T = \{\boldsymbol{\sigma} \in X \mid (\sigma_{11}-\sigma_{22})^2 + 4\sigma_{12}^2 \leq \sigma_y^2\}, \tag{7}$$

$$B_{MC} = \{\boldsymbol{\sigma} \in X \mid (\sigma_{11}-\sigma_{22})^2 + 4\sigma_{12}^2 \leq (2c\cos\phi - (\sigma_{11}+\sigma_{22})\sin\phi)^2\}, \tag{8}$$

$$B_{DP} = \{\boldsymbol{\sigma} \in X \mid (\sigma_{11}-\sigma_{22})^2 + 4\sigma_{12}^2 \leq (2\beta - 3\alpha(\sigma_{11}+\sigma_{22}))^2\}, \tag{9}$$

where c is the material cohesion, ϕ denotes the friction angle and α and β refer to material properties. Clearly, (7),(8) and (9) are convex sets in their variables σ_{ij} and can be expressed in the generic form (5).

2.2. The limit analysis problem, duality and exact bounds, in continuous form

Let C denote the affine hyperplane $C = \{\mathbf{u} \in Y | F(\mathbf{u}) = 1\}$, consisting of those kinematically admissible velocity fields for which the external work rate equals one. Now, the exact collapse multiplier, λ^*, which is the value to be bounded, results from solving any of the following equivalent problems:

$$\begin{aligned}
\lambda^* &= \sup \lambda \\
&\quad s.t. \begin{cases} \exists \boldsymbol{\sigma} \in B \\ a(\boldsymbol{\sigma}, \mathbf{u}) = \lambda F(\mathbf{u}), \forall \mathbf{u} \in Y \end{cases} && (10) \\
&= \sup_{\boldsymbol{\sigma} \in B} \inf_{\mathbf{u} \in C} a(\boldsymbol{\sigma}, \mathbf{u}) && (11) \\
&= \inf_{\mathbf{u} \in C} \sup_{\boldsymbol{\sigma} \in B} a(\boldsymbol{\sigma}, \mathbf{u}) && (12) \\
&= \inf_{\mathbf{u} \in C} D(\mathbf{u}). && (13)
\end{aligned}$$

Problem (10) is the so-called *static principle of limit analysis*, whereas (13) is known as the *kinematic principle of limit analysis*. The equivalence between (10) and (11) follows from the linearity in $\mathbf{u}$ of both functionals $a(\boldsymbol{\sigma}, \mathbf{u})$ and $F(\mathbf{u})$. Additionally, the equality between (11) and (12) holds thanks to strong duality, which is proved in detail in [11]. Finally, $D(\mathbf{u})$ is defined as the inner supremum in (12) and represents the total energy dissipation rate associated with $\mathbf{u}$. Moreover, [11] also shows that collapse fields $\mathbf{u}^*$ and $\boldsymbol{\sigma}^*$ exist and are a saddle point of $a(\boldsymbol{\sigma}, \mathbf{u})$.

2.3. The limit analysis problem, duality and exact bounds in discrete form

Let Ω_h denote a discretization of the domain of study, Ω, and let X_h and Y_h be finite element function spaces that approximate the continuous stress and velocity fields: $\boldsymbol{\sigma} \approx \boldsymbol{\sigma}_h \in X_h$ and $\mathbf{u} \approx \mathbf{u}_h \in Y_h$. Moreover, the discrete convex set of admissible stresses, B_h, must be such that $B_h \subseteq B \cap X_h$, and the affine hyperplane to which $\mathbf{u}_h$ is restricted, becomes now $C_h = \{\mathbf{u}_h \in Y_h | F(\mathbf{u}_h) = 1\}$. Then, the discretized version of the variational continuous limit analysis problem (10-13) reads as follows:

$$\begin{aligned}
\lambda_h^* &= \max \lambda \\
&\quad s.t. \begin{cases} \exists \boldsymbol{\sigma}_h \in B_h \\ a(\boldsymbol{\sigma}_h, \mathbf{u}_h) = \lambda F(\mathbf{u}_h), \forall \mathbf{u}_h \in Y_h \end{cases} && (14) \\
&= \max_{\boldsymbol{\sigma}_h \in B_h} \min_{\mathbf{u}_h \in C_h} a(\boldsymbol{\sigma}_h, \mathbf{u}_h) && (15) \\
&= \min_{\mathbf{u}_h \in C_h} \max_{\boldsymbol{\sigma}_h \in B_h} a(\boldsymbol{\sigma}_h, \mathbf{u}_h) && (16) \\
&= \min_{\mathbf{u}_h \in C_h} D_h(\mathbf{u}_h). && (17)
\end{aligned}$$

The above discrete duality holds for all practical discretizations (see proof in [11]). Note that thanks to discrete duality, the approximated value λ_h^* to the exact collapse multiplier, λ^*, can be obtained in several different ways. Indeed, one can compute λ_h^* by solving the discrete static principle (14) or the discrete kinematic principle (17). Also, both problems can be solved at the same time using a mixed finite element method to approximate simultaneously the collapse fields for the stresses and velocities. This is the approach that will be followed here.

In general, for a given choice of $X_h \times Y_h$, λ_h^* is only an estimate or approximation to λ^*, but not a bound. However, there exist particular combinations of appropriately-chosen interpolation spaces $X_h \times Y_h$ for both the stresses and velocities that, when used to discretize the continuous problem (10-13), lead to discretizations (14-17) whose solution, λ_h^*, is guaranteed to be either a lower bound ($\lambda_h^{*LB} \leq \lambda^*$) or an upper bound ($\lambda^* \leq \lambda_h^{*UB}$) of the true collapse multiplier, λ^* (and not only an estimate). In particular, the combination of spaces that guarantee the attainment of lower bounds will be named *purely static spaces*, whereas those that yield upper bounds will be named *purely kinematic spaces*. The requirements on these particular spaces are given next.

Purely static spaces: $X_h \times Y_h$ is said to be a combination of purely static spaces, and denoted by $X_h^{LB} \times Y_h^{LB}$, if the following two conditions hold:

1. Satisfaction of the discrete equilibrium equation on X_h^{LB} implies the continuous equilibrium equation. This is equivalent to the following implication for any $\boldsymbol{\sigma}_h \in X_h^{LB}$:

$$a(\boldsymbol{\sigma}_h, \mathbf{u}_h) = \lambda F(\mathbf{u}_h),\ \forall \mathbf{u}_h \in Y_h^{LB} \implies a(\boldsymbol{\sigma}_h, \mathbf{u}) = \lambda F(\mathbf{u}),\ \forall \mathbf{u} \in Y. \tag{18}$$

2. Satisfaction of the membership condition $\boldsymbol{\sigma}_h \in B_h^{LB} \subseteq B \cap X_h^{LB}$ in some discrete or test points directly implies that $\boldsymbol{\sigma}_h \in B$ over the continuum.

Thus, the advantage of using purely static spaces is that, by only forcing discrete satisfaction of equilibrium and membership, one can guarantee equilibrium and membership over the whole domain. Therefore, the constraints in the maximization problem (10) are satisfied exactly,

which means that the inner infimum in (11) is also computed exactly for all the stresses belonging to an appropriate set. Note that the above conditions imply that:

$$\max_{\boldsymbol{\sigma}\in B_h}\inf_{\mathbf{u}\in C} a(\boldsymbol{\sigma},\mathbf{u}) = \max_{\boldsymbol{\sigma}\in B_h}\min_{\mathbf{u}\in C_h} a(\boldsymbol{\sigma},\mathbf{u}) \tag{19}$$

and therefore the use of purely static spaces provides a computable strict lower bound as:

$$\lambda^* = \sup_{\boldsymbol{\sigma}\in B}\inf_{\mathbf{u}\in C} a(\boldsymbol{\sigma},\mathbf{u}) \geq \max_{\boldsymbol{\sigma}\in B_h}\inf_{\mathbf{u}\in C} a(\boldsymbol{\sigma},\mathbf{u}) = \max_{\boldsymbol{\sigma}\in B_h}\min_{\mathbf{u}\in C_h} a(\boldsymbol{\sigma},\mathbf{u}) \equiv \lambda_h^{*LB} \tag{20}$$

Purely kinematic spaces: $X_h \times Y_h$ is said to be a combination of purely kinematic spaces, and denoted by $X_h^{UB} \times Y_h^{UB}$, if the discrete energy dissipation rate, $D_h(\mathbf{u}_h)$, is exact on Y_h^{UB}:

$$\max_{\boldsymbol{\sigma}_h\in B_h} a(\boldsymbol{\sigma}_h,\mathbf{u}_h) = \sup_{\boldsymbol{\sigma}\in B} a(\boldsymbol{\sigma},\mathbf{u}_h),\ \forall \mathbf{u}_h \in Y_h. \tag{21}$$

and therefore, a computable strict upper bound is obtained as:

$$\lambda^* = \inf_{\mathbf{u}\in C}\sup_{\boldsymbol{\sigma}\in B} a(\boldsymbol{\sigma},\mathbf{u}) \leq \min_{\mathbf{u}\in C_h}\sup_{\boldsymbol{\sigma}\in B} a(\boldsymbol{\sigma},\mathbf{u}) = \min_{\mathbf{u}\in C_h}\max_{\boldsymbol{\sigma}\in B_h} a(\boldsymbol{\sigma},\mathbf{u}) \equiv \lambda_h^{*UB} \tag{22}$$

Hence, the use of purely kinematic spaces results in an upper bound method. Figure 1 summarizes graphically the above explanations.

3. SECOND-ORDER CONE PROGRAMMING WITHIN THE GENERAL FRAMEWORK OF CONIC PROGRAMMING

Interior point methods for the efficient solution of convex optimization problems have been developed in recent years. Therefore, recognizing the convex structure of the problem is important since it guarantees an efficient solution process. A particular class of convex problems are the so-called conic programs (CP) [8]. Any CP problem can be written in the following canonical primal (P) or dual (D) forms:

$$(P) \qquad \min\left\{c^T x \mid Ax = b,\ x \in \mathcal{K}\right\}, \tag{23}$$

$$(D) \qquad \max\left\{b^T y \mid A^T y + s = c,\ s \in \mathcal{K}_*\right\}, \tag{24}$$

where $x \in \Re^n$ is the vector of decision variables, $c \in \Re^n$, $b \in \Re^m$, $A \in \Re^{m\times n}$ are given data, $s \in \Re^n$ is a vector of slack variables, $\mathcal{K} \subset \Re^n$ is a pointed and closed convex cone with a nonempty interior and $\mathcal{K}_* = \left\{s \in \Re^n \mid s^T x \geq 0,\ \forall x \in \mathcal{K}\right\}$ is the dual cone to $\mathcal{K}$ and is also a closed convex pointed cone with a nonempty interior. The most relevant cones satisfying these properties are the so-called canonical cones: the Positive orthant, $\Re^n_+$, the Lorentz (or second order or ice-cream) cone, $\mathcal{L}^n$, and the Positive semidefinite cone, $\mathcal{S}^n_+$. In particular, a Lorentz cone is defined as:

$$\mathcal{K} \equiv \mathcal{L}^n = \left\{ x \in \Re^n \mid x_1 \geq \sqrt{\sum_{i=2}^{n} x_i^2} \right\}. \tag{25}$$

When the cone $\mathcal{K}$ is one of the canonical cones, then the following important subclasses of conic programming arise: Linear Programming (LP) when $\mathcal{K} \equiv \Re^n_+$, Second-order Cone (or

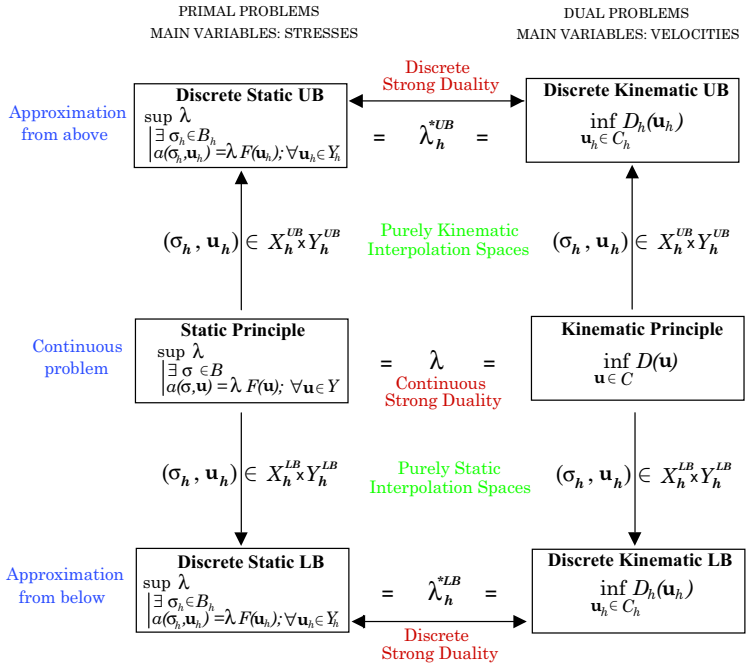

Figure 1. The use of purely static and purely kinematic spaces to obtain lower and upper bounds

Conic Quadratic) Programming (SOCP) when $\mathcal{K} \equiv \mathcal{L}^n$ and Semidefinite Programming (SDP) when $\mathcal{K} \equiv \mathcal{S}^n_+$. Notice that LP is a particular case of SOCP which, in turn, can always be cast as a SDP program.

The canonical cones are self-dual, that is, $(\Re^n_+)_* = \Re^n_+, (\mathcal{L}^n)_* = \mathcal{L}^n, (\mathcal{S}^n_+)_* = \mathcal{S}^n_+$. In general, the cones $\mathcal{K}$ and $\mathcal{K}_*$ are not exclusively one of the cones presented, but a cartesian product of many of them, say r. Thus, above definitions can be generalized with $\mathcal{K} = \mathcal{K}^1 \times \ldots \times \mathcal{K}^r$ and $\mathcal{K}_* = \mathcal{K}^1_* \times \ldots \times \mathcal{K}^r_*$. When the cones involved are of different nature, the resulting problem is named a *mixed conic program*, for which (P) and (D) are still valid.

The most fundamental result of Conic Programming is the conic duality theorem, over which the interior point algorithms used in the solution process are built. Provided that either (P) or (D) is strictly feasible and bounded, the main practical implication of the theorem is that an optimal primal-dual feasible pair (x^*, y^*) exists and the optimal values of (P) and (D) are equal to each other, that is, $b^T y^* = c^T x^*$ (zero duality gap).

CP problems are generally solved using IPMs (see [27] for an extensive and deep treatment). These methods, whose foundations were laid in [18], are polynomial-time methods and constitute, nowadays, the state of the art in convex optimization with deep theoretical and practical results. IPMs look for an optimal solution while moving in the interior of the feasible set, instead of restricting the search at the boundaries. To prevent the algorithm from reaching the boundary, a barrier function is added to the cost function. The nice convergence properties of IPMs are directly related to the existence of appropriate barriers for the cones under

consideration. In particular, the existence of self-concordant barriers makes the scheme a polynomial time one!. Those barriers exist for the three canonical self-dual cones previously presented, under the form of logarithmic barriers.

Currently, the primal-dual path-following IPM (with its variants) is the method of choice in commercial implementations, thanks to its excellent performance in large scale applications and, especially, in the presence of sparsity. The method is based on duality, and search directions for optimality are computed in both the primal and the dual feasible spaces. Typically, the search directions used in CP are AHO [1], HKM [17] and NT [28]. In particular, for SOCP, the NT option is the one that generally offers the best computational performance. Notice finally that SOCP is slower to solve than LP problems, but notably faster than SDP problems, especially if sparsity is exploited.

4. BOUND PROBLEMS: METHODOLOGY, IMPLEMENTATION AND SOLUTION

This section presents the methodology that has been used to compute bounds to the exact collapse multiplier, λ^*. The bound problems solved here correspond to the two-dimensional version of the limit analysis problem (10-13), and both the plane stress and the plane strain models are addressed. Only the von Mises model has been used but the method could be extended to other criteria satisfying criteria 5. Its restriction to plane stress, B_1, and plane strain, B_2, expressed in the format of 5 reads as follows:

$$B_1 = \{\boldsymbol{\sigma} \in X \mid (\sigma_{11}-\sigma_{22})^2 + \sigma_{11}^2 + \sigma_{22}^2 + 6\sigma_{12}^2 \leq 2\sigma_y^2\}, \tag{26}$$

$$B_2 = \{\boldsymbol{\sigma} \in X \mid (\sigma_{11}-\sigma_{22})^2 + 4\sigma_{12}^2 \leq \frac{4}{3}\sigma_y^2\}. \tag{27}$$

Let $\mathcal{T}_h$ denote a triangulation consisting of E triangular elements, Ω^e, that form a partition of the body. The boundary of the element Ω^e is denoted by $\partial\Omega^e$. Let $\mathcal{E}$ be the set of all the edges in the mesh, which is decomposed into the following three disjoint sets: $\mathcal{E} = \mathcal{E}^{\mathcal{O}} \cup \mathcal{E}^{\mathcal{D}} \cup \mathcal{E}^{\mathcal{N}}$, where $\mathcal{E}^{\mathcal{O}} = \{\xi_e^{e'} \mid \xi_e^{e'} = \partial\Omega^e \cap \partial\Omega^{e'};\ \forall e, e' \in \mathcal{T}_h\}$ (set of interior edges), $\mathcal{E}^{\mathcal{D}} = \{\xi_e^D \mid \xi_e^D = \partial\Omega^e \cap \Gamma^D;\ \forall e \in \mathcal{T}_h\}$ (set of edges associated to Dirichlet boundaries) and $\mathcal{E}^{\mathcal{N}} = \{\xi_e^N \mid \xi_e^N = \partial\Omega^e \cap \Gamma^N;\ \forall e \in \mathcal{T}_h\}$ (set of edges associated to Neumann boundaries). For simplicity of presentation it will be assumed that a given edge is either of Dirichlet or Neumann type. The extension to mixed boundary conditions is straight forward.

4.1. The Lower Bound Problem

4.1.1. Purely Static Spaces For both the plane stress and the plane strain cases, one can show that a possible purely static formulation results from approximating the stress field with piecewise discontinuous stresses that are linearly interpolated within the elements, and the velocity field with constants on each element together with additional linear interpolations along the inter-element boundaries. These stresses can be expressed as:

$$\sigma_{hi}^e(x_1, x_2) = \sum_{a=1}^{3} \sigma_i^{a,e} N_a^e(x_1, x_2), \quad i = 1:3, \tag{28}$$

where $a = 1:3$ refers to a local numbering of each of the three nodes of the element, $\sigma_i^{a,e}$ ($\sigma_1 \equiv \sigma_{11}$, $\sigma_2 \equiv \sigma_{22}$, $\sigma_3 \equiv \sigma_{12}$) are the nodal stress values and $N_a^e(\mathbf{x})$ is a linear shape function valuing 1 at the node a and 0 at the other two nodes. Clearly, the interpolation space introduces 9 stress variables or unknowns per triangle ($\sigma_i^a; i = 1:3, a = 1:3$), thereby enabling different stress tensors to arise in each node of the mesh, as many as elements sharing that node.

The approximation of the velocity field, $\mathbf{u}_h \in Y_h^{LB} \subset Y$, Y_h^{LB} introduces 2 unknowns per triangle (constant approximation for each element) and 4 additional degrees of freedom per edge (linear approximation). This is shown in the following (global and local) interpolations:

$$u_{hi}(x_1, x_2) = \sum_{e=1}^{E} u_i^e \psi_e(x_1, x_2), \quad i = 1:2, \tag{29}$$

$$u_{hi}^{\xi}(s) = \sum_{\alpha=1}^{2} u_i^{\alpha,\xi} N_\alpha^\xi(s), \quad i = 1:2, \tag{30}$$

where $\psi_e(\mathbf{x}) = 1$, $\forall \mathbf{x} \in \Omega^e$ and $\psi_e(\mathbf{x}) = 0$ otherwise, $N_\alpha^\xi(s)$ is a linear shape function over the edge ξ, s denotes a local coordinate and $\alpha = 1:2$ are the two nodes of the edge. Assuming that the body forces, $\mathbf{f}$, are constant and the tractions, $\mathbf{g}$, vary at most linearly, then the interpolation space Y_h^{LB} is rich enough, when compared to X_h^{LB}, to force equilibrium point by point. The proof is detailed in Appendix A.1.

The stress field $\boldsymbol{\sigma}_h$ is required to belong to the set of admissible stresses, $B_{\delta,h}$, in every point of the domain Ω, that is, $\boldsymbol{\sigma}_h(\mathbf{x}) \in B_{\delta,h}$, $\forall \mathbf{x} \in \Omega$; where $B_{\delta,h} = B_\delta \cap X_h^{LB}$ and $\delta = 1:2$ (plane stress or plane strain). Fortunately, this general pointwise condition can be satisfied by just forcing the membership constraint to hold over the nodes of each triangle, which translates into $3 \times E$ nodal inequalities. This nice property is due to the choice of a piecewise linear interpolation of the stresses and the use of triangular elements. The proof is given, for the plane stress model, in Appendix A.1.2. For the plane strain case, the proof is simpler and completely analogous. Notice that, for other element types such as quadratic or bi-quadratic elements, the yield condition might be violated between nodes even if it is satisfied at all nodes.

4.1.2. Discretization Process Recall that the attainment of a lower or an upper bound only depends on the interpolation spaces used and not on the particular version of the limit analysis problem that is discretized (see Figure 1). In particular, the *static principle of limit analysis*, (10), has been chosen to be the problem to discretize, using the (previously described) purely static spaces, $X_h^{LB} \times Y_h^{LB}$. This choice corresponds to the lower left branch of Figure 1, leading to the formulation of the *"Discrete Static LB"* problem.

The static principle (14) can be exclusively expressed in terms of stresses belonging to the space X_h^{LB}, as follows:

$$\max \ \lambda \quad s.t. \begin{cases} \nabla \cdot \boldsymbol{\sigma}_h^e + \lambda \mathbf{f}^e = \mathbf{0}, & \text{in } \Omega^e, \forall e \in \mathcal{T}_h \\ (\boldsymbol{\sigma}_h^e - \boldsymbol{\sigma}_h^{e'}) \cdot \mathbf{n}^{\xi_e^{e'}} = \mathbf{0}, & \forall \xi_e^{e'} \in \mathcal{E}^{\mathcal{O}} \\ \boldsymbol{\sigma}_h^e \cdot \mathbf{n}^{\xi_e^N} = \lambda \mathbf{g}^{\xi_e^N}, & \forall \xi_e^N \in \mathcal{E}^{\mathcal{N}} \\ \boldsymbol{\sigma}_h^e \in B_{\delta,h}, & \text{in } \Omega^e, \ \forall e \in \mathcal{T}_h \end{cases} \tag{31}$$

Next, the discretization of each of the above constraints is addressed.

- **Elemental equilibrium constraints.** For each triangle Ω^e, the local interpolation (28) is inserted into the vectorial equation $\nabla \cdot \boldsymbol{\sigma}^e + \lambda \mathbf{f}^e = \mathbf{0}$. Grouping all the nodal stress components into a single vector and using the following notation for the (constant) derivatives of the (linear) shape functions $N^e_{a,i} = \frac{\partial N^e_a(\mathbf{x})}{\partial x_i}$, where $i = 1:2$, the following matrix equation emerges:

$$\begin{pmatrix} N^e_{1,1} & 0 & N^e_{1,2} & N^e_{2,1} & 0 & N^e_{2,2} & N^e_{3,1} & 0 & N^e_{3,2} \\ 0 & N^e_{1,2} & N^e_{1,1} & 0 & N^e_{2,2} & N^e_{2,1} & 0 & N^e_{3,2} & N^e_{3,1} \end{pmatrix} \begin{pmatrix} \sigma_1^{1,e} \\ \sigma_2^{1,e} \\ \sigma_3^{1,e} \\ \sigma_1^{2,e} \\ \sigma_2^{2,e} \\ \sigma_3^{2,e} \\ \sigma_1^{3,e} \\ \sigma_2^{3,e} \\ \sigma_3^{3,e} \end{pmatrix} + \lambda \begin{pmatrix} f_1^e \\ f_2^e \end{pmatrix} = \begin{pmatrix} 0 \\ 0 \end{pmatrix}, \tag{32}$$

  or, equivalently in compact form,

$$\underline{\underline{B}}^e \underline{\sigma}^e_h + \lambda \underline{F}^{eq1,e}_h = \underline{0}. \tag{33}$$

  Now, let $\underline{\sigma}_h$ denote a global vector collecting the $9 \times E$ nodal stress components for all the elements in the mesh, and $\underline{F}^{eq1}_h$ be a $2 \times E$ global volume force vector. Likewise, a $(2 \times E, 9 \times E)$ global matrix $\underline{\underline{A}}^{eq1}$, consisting of the elemental matrices $\underline{\underline{B}}^e$, is built. The assembly process is straightforward since the equations for the elements are uncoupled. Consequently, $\underline{\underline{A}}^{eq1}$ results in a very sparse block diagonal matrix:

$$\underline{\underline{A}}^{eq1} = \begin{pmatrix} \underline{\underline{B}}^1 & \underline{\underline{0}} & \cdots & \cdots & \underline{\underline{0}} \\ \underline{\underline{0}} & \underline{\underline{B}}^2 & \underline{\underline{0}} & \cdots & \underline{\underline{0}} \\ \vdots & & \ddots & & \vdots \\ \vdots & & & \ddots & \vdots \\ \underline{\underline{0}} & \cdots & \cdots & \cdots & \underline{\underline{B}}^E \end{pmatrix}, \tag{34}$$

  where $\underline{\underline{0}}$ is a zero matrix of dimensions $(2, 9)$. Finally, the global discrete system of equations corresponding to the elemental equilibrium constraint is given by:

$$\underline{\underline{A}}^{eq1} \underline{\sigma}_h + \underline{F}^{eq1}_h \lambda = \underline{0}. \tag{35}$$

- **Inter-element and boundary equilibrium constraints** The restriction of the linear interpolation (28) to an edge, ξ, can be written as follows:

$$\sigma_i(s) = \sum_{\alpha=1}^{2} \sigma_i^\alpha N^\xi_\alpha(s), \quad i = 1:3. \tag{36}$$

  Now, inserting interpolation (36) into the equations $(\boldsymbol{\sigma}^e_h - \boldsymbol{\sigma}^{e'}_h) \cdot \mathbf{n}^{\xi^{e'}_e} = \mathbf{0}$, $\forall \xi^{e'}_e \in \mathcal{E}^{\mathcal{O}}$ and $\boldsymbol{\sigma}^e_h \cdot \mathbf{n}^{\xi^N_e} = \lambda \mathbf{g}^{\xi^N_e}$, $\forall \xi^N_e \in \mathcal{E}^{\mathcal{N}}$, one obtains, after some simple algebra, a system of 4 scalar equations for each vector equation. The 4 equations imposed in each interior edge,

$\xi_e^{e'} \in \mathcal{E}^{\mathcal{O}}$, are:

$$(\sigma_1^{1,e} - \sigma_1^{1,e'})n_1^\xi + (\sigma_3^{1,e} - \sigma_3^{1,e'})n_2^\xi = 0 \tag{37}$$
$$(\sigma_1^{2,e} - \sigma_1^{2,e'})n_1^\xi + (\sigma_3^{2,e} - \sigma_3^{2,e'})n_2^\xi = 0 \tag{38}$$
$$(\sigma_3^{1,e} - \sigma_3^{1,e'})n_1^\xi + (\sigma_2^{1,e} - \sigma_2^{1,e'})n_2^\xi = 0 \tag{39}$$
$$(\sigma_3^{2,e} - \sigma_3^{2,e'})n_1^\xi + (\sigma_2^{2,e} - \sigma_2^{2,e'})n_2^\xi = 0 \tag{40}$$

Likewise, the following 4 equations are imposed on each boundary edge, $\xi_e^N \in \mathcal{E}^{\mathcal{N}}$:

$$\sigma_1^{1,e} n_1^\xi + \sigma_3^{1,e} n_2^\xi = \lambda g_1^\xi \tag{41}$$
$$\sigma_1^{2,e} n_1^\xi + \sigma_3^{2,e} n_2^\xi = \lambda g_1^\xi \tag{42}$$
$$\sigma_3^{1,e} n_1^\xi + \sigma_2^{1,e} n_2^\xi = \lambda g_2^\xi \tag{43}$$
$$\sigma_3^{2,e} n_1^\xi + \sigma_2^{2,e} n_2^\xi = \lambda g_2^\xi \tag{44}$$

Clearly, the total number of edge equations is $4 \times (|\mathcal{E}^{\mathcal{O}}| + |\mathcal{E}^{\mathcal{N}}|)$. The systems of equations (37-40) and (41-44) can be combined into a global matrix linear equation, as follows:

$$\underline{\underline{A}}^{eq2} \underline{\sigma}_h + \underline{F}_h^{eq2} \lambda = \underline{0}, \tag{45}$$

where $\underline{\sigma}_h$ is the $9 \times E$ vector of unknown nodal stresses previously used. Moreover, $\underline{\underline{A}}^{eq2}$ is a $(4 \times (|\mathcal{E}^{\mathcal{O}}| + |\mathcal{E}^{\mathcal{N}}|), 9 \times E)$ matrix, whose entries are either zero or the components n_1^ξ, n_2^ξ of the unit vectors normal to the edges with the appropriate sign. Finally, $\underline{F}_h^{eq2}$ is a vector consisting of zeros, for the equations associated to the interior edges, or minus the components g_1^ξ, g_2^ξ of the external surface loads, for the Neumann boundary edges.

- **Membership constraints. Formulation as multiple Second-order Cones** Appendix A.1.2 shows that the yield condition is not violated at any point of the domain if the inequality

$$(\sigma_1^{a,e} - \sigma_2^{a,e})^2 + (\sigma_1^{a,e})^2 + (\sigma_2^{a,e})^2 + 6(\sigma_3^{a,e})^2 \leq 2\sigma_y^2 \qquad (\delta = 1, \text{plane stress}) \tag{46}$$
$$\text{or} \qquad (\sigma_1^{a,e} - \sigma_2^{a,e})^2 + 4(\sigma_3^{a,e})^2 \leq \frac{4}{3}\sigma_y^2 \qquad (\delta = 2, \text{plane strain}) \tag{47}$$

is satisfied at every node, a, of each element, e, of the mesh ($3 \times E$ inequalities). A convenient way to impose inequality (46) or (47) is to force the vector $(\sqrt{2}\sigma_y, \sigma_1^{a,e}, \sigma_2^{a,e}, \sqrt{6}\sigma_3^{a,e}, \sigma_1^{a,e} - \sigma_2^{a,e})$ (plane stress) or $(\frac{2}{\sqrt{3}}\sigma_y, 2\sigma_3^{a,e}, \sigma_1^{a,e} - \sigma_2^{a,e})$ (plane strain) to belong to the Lorentz cone $\mathcal{L}^n$, where $n = 5$ for plane stress and $n = 3$ for plane strain. Since second-order cone constraints are directly imposed through the decision variables (see section 3), it is convenient to introduce a vector of additional variables, $\underline{x}^{a,e}$, as follows:

$$\text{plane stress} \begin{cases} x_1^{a,e} = \sqrt{2}\sigma_y \\ -\sigma_1^{a,e} + x_2^{a,e} = 0 \\ -\sigma_2^{a,e} + x_3^{a,e} = 0 \\ -\sqrt{6}\sigma_3^{a,e} + x_4^{a,e} = 0 \\ -\sigma_1^{a,e} + \sigma_2^{a,e} + x_5^{a,e} = 0 \end{cases}, \quad \text{plane strain} \begin{cases} x_1^{a,e} = \frac{2}{\sqrt{3}}\sigma_y \\ -2\sigma_3^{a,e} + x_2^{a,e} = 0 \\ -\sigma_1^{a,e} + \sigma_2^{a,e} + x_3^{a,e} = 0 \end{cases} \tag{48}$$

Now, each vector $\underline{x}^{a,e}$ is forced to belong to $\mathcal{L}^n$. The imposition of (48) over all the mesh requires $3n \times E$ equations (n equations per node and 3 nodes per element). In matrix notation, the global system can be written as follows:

$$\underline{\underline{A}}_{\delta}^{soc}\underline{\sigma}_h + \underline{\underline{I}}_{\delta}\underline{x}_{\delta}^{soc} = \underline{b}_{\delta}^{soc}, \tag{49}$$

where $\underline{\sigma}_h$ is the usual vector of unknown nodal stresses, $\underline{\underline{I}}_{\delta}$ is a $(3n \times E, 3n \times E)$ identity matrix, $\underline{x}_{\delta}^{soc}$ is a vector of $3n \times E$ additional variables ordered in the same way as $\underline{\sigma}_h$, and $\underline{b}_{\delta}^{soc}$ and $\underline{\underline{A}}_{\delta}^{soc}$ are, respectively, a $3n \times E$ vector and a $(3n \times E, 9 \times E)$ block diagonal matrix of the following forms:

$$\underline{b}_{\delta}^{soc} = \begin{pmatrix} \underline{b}_{\delta}^{a,e} \\ \underline{b}_{\delta}^{a,e} \\ \vdots \\ \vdots \\ \underline{b}_{\delta}^{a,e} \end{pmatrix}, \quad \underline{\underline{A}}_{\delta}^{soc} = \begin{pmatrix} \underline{\underline{M}}_{\delta} & \underline{\underline{0}} & \cdots & \cdots & \underline{\underline{0}} \\ \underline{\underline{0}} & \underline{\underline{M}}_{\delta} & \underline{\underline{0}} & \cdots & \underline{\underline{0}} \\ \vdots & & \ddots & & \vdots \\ \vdots & & & \ddots & \vdots \\ \underline{\underline{0}} & \cdots & \cdots & \cdots & \underline{\underline{M}}_{\delta} \end{pmatrix}; \quad \delta = 1:2 \tag{50}$$

where

$$\underline{b}_1^{a,e} = \begin{pmatrix} \sqrt{2}\sigma_y \\ 0 \\ 0 \\ 0 \end{pmatrix}, \quad \underline{\underline{M}}_1 = \begin{pmatrix} 0 & 0 & 0 \\ -1 & 0 & 0 \\ 0 & -1 & 0 \\ 0 & 0 & -\sqrt{6} \\ -1 & 1 & 0 \end{pmatrix}; \quad \underline{b}_2^{a,e} = \begin{pmatrix} \frac{2}{\sqrt{3}}\sigma_y \\ 0 \\ 0 \end{pmatrix}, \quad \underline{\underline{M}}_2 = \begin{pmatrix} 0 & 0 & 0 \\ 0 & 0 & -2 \\ -1 & 1 & 0 \end{pmatrix}. \tag{51}$$

4.1.3. The Lower Bound Problem as a SOCP Expressing the previous matrix constraints (35), (45) and (49) in a single matrix equation, the discretization of the lower bound problem (31) is given by:

$$\lambda_h^{*LB} \equiv \max \lambda \quad s.t. \begin{cases} \overbrace{\begin{pmatrix} \underline{\underline{A}}^{eq1} & \vdots & \underline{\underline{F}}_h^{eq1} & \vdots & \underline{\underline{0}} \\ \underline{\underline{A}}^{eq2} & \vdots & \underline{\underline{F}}_h^{eq2} & \vdots & \underline{\underline{0}} \\ \underline{\underline{A}}_{\delta}^{soc} & \vdots & \underline{\underline{0}} & \vdots & \underline{\underline{I}}_{\delta} \end{pmatrix}}^{9\times E \;+\; 1 \;+\; 3n\times E} \begin{pmatrix} \underline{\sigma}_h \\ \lambda \\ \underline{x}_{\delta}^{soc} \end{pmatrix} = \begin{pmatrix} \underline{0} \\ \underline{0} \\ \underline{b}_{\delta}^{soc} \end{pmatrix} \begin{matrix} m_1 = 2 \times E \\ m_2 = 4 \times (|\mathcal{E}^{\mathcal{O}}| + |\mathcal{E}^{\mathcal{N}}|) \\ m_3 = 3n \times E \end{matrix} \\ \underline{\sigma}_h \text{ free}, \; \lambda \text{ free}, \; \underline{x}_{\delta}^{soc} \in \mathcal{K} \end{cases} \tag{52}$$

where $\mathcal{K} = \overbrace{\mathcal{L}^n \times \cdots \times \mathcal{L}^n}^{3\times E}$. The sparsity of the above global matrix, for both the plane stress and plane strain cases, is shown in Figure 2 for a test example consisting of only 18 elements.

Notice that this problem is a conic program and has the standard form required by most optimization packages. From section 3, and given that the lower bound problem has a strictly feasible interior, it is clear that strong duality holds. Therefore, λ_h^{*LB} can also be obtained by

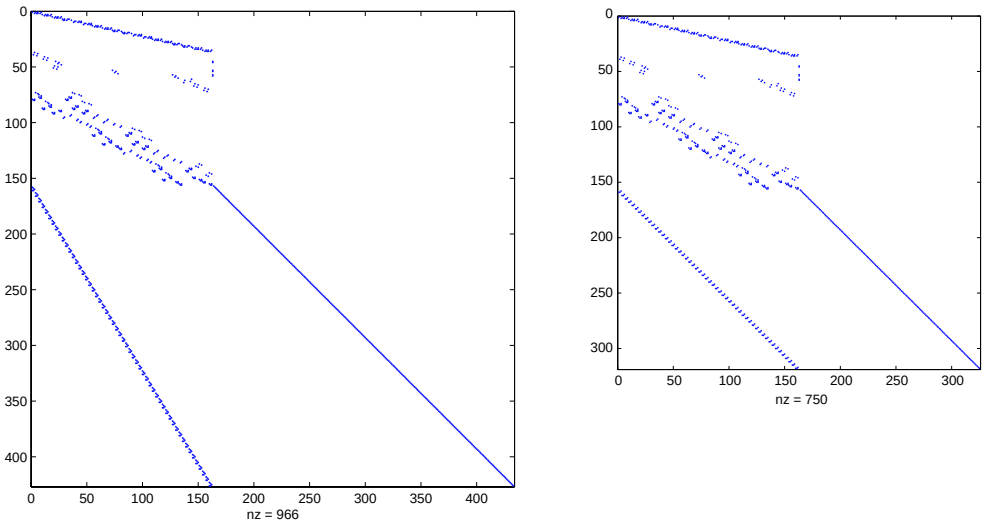

plane stress plane strain

Figure 2. Illustration of the structure and sparsity of the global matrix for the lower bound problem

solving the dual problem to (52), which takes the following form:

$$\lambda_h^{*LB} \equiv \min \underline{b}_\delta^{soc^T} \underline{y}$$
$$s.t. \left\{ \begin{array}{l} \left(\begin{array}{ccc} \underline{\underline{A}}^{eq1^T} & \underline{\underline{A}}^{eq2^T} & \underline{\underline{A}}_\delta^{sos^T} \\ \underline{F}_h^{eq1^T} & \underline{F}_h^{eq2^T} & \underline{0}^T \end{array} \right) \left(\begin{array}{c} \underline{u}^1 \\ \underline{u}^2 \\ \underline{y} \end{array} \right) = \left(\begin{array}{c} \underline{0} \\ 1 \end{array} \right) \Big\} \begin{array}{l} 9 \times E \\ 1 \end{array} \\ \underline{u}^1,\ \underline{u}^2 \text{ free},\ \underline{y} \in \mathcal{K} \end{array} \right. \tag{53}$$

where $\underline{u}^1 \in \Re^{m_1}$, $\underline{u}^2 \in \Re^{m_2}$, $\underline{y} \in \Re^{m_3}$. The interpretation of these equations and variables will become more transparent when the upper bound problem is described below.

4.1.4. Reduction of the dimensions of the global problem and transformation into a pure SOCP The lower bound matrix defined in (52) has dimensions $((9+3n)E+1;\ (2+3n)E+4(|\mathcal{E}^{\mathcal{O}}|+|\mathcal{E}^{\mathcal{N}}|))$ and involves the vector of nodal stresses, $\underline{\sigma}_h$, the collapse multiplier, λ, and the vector of additional variables, $\underline{x}^{soc}$. While it was natural and easy to build the linear system of equations using those variables, they are not optimal for solving the lower bound problem since they lead to matrices that are much larger than strictly required. To optimize the computational cost, one can introduce a change of variables that reduces substantially the number of equations and variables involved.

The idea is very simple. In problem (52), $\underline{\sigma}_h$ appears in the equilibrium equations as a "free" vector, that is, the nodal stresses are not restricted to any particular cone. On the other hand, some affine combinations of the stresses, which correspond to the additional variables $\underline{x}^{soc}$, are forced to belong to the Lorentz cone $\mathcal{L}^n$. It is possible to eliminate the nodal stress variables, $\underline{\sigma}_h$, by directly formulating the equilibrium equations in terms of the additional variables, $\underline{x}^{soc}$. The details of this change of variables and the consequent reformulation are given in Appendix

B.

The transformed version of (52) results in the following problems, which are the ones actually solved. For **plane stress**:

$$\lambda_h^{*LB} \equiv \max \lambda \quad s.t. \begin{cases} \overbrace{\begin{pmatrix} \underline{F}_h^{eq1} & \vdots & \underline{\underline{A}}^{eq1}\underline{Q} \\ \underline{F}_h^{eq2} & \vdots & \underline{\underline{A}}^{eq2}\underline{Q} \\ \underline{0} & \vdots & \underline{\underline{R}} \end{pmatrix}}^{\begin{matrix}1 & 15\times E\end{matrix}} \begin{pmatrix} \lambda \\ \underline{x}_1^{soc} \end{pmatrix} = \begin{pmatrix} \underline{0} \\ \underline{0} \\ \underline{\tilde{b}}_1^{soc} \end{pmatrix} \Bigg\} \begin{matrix} 2\times E \\ 4\times(|\mathcal{E}^{\mathcal{O}}|+|\mathcal{E}^{\mathcal{N}}|) \\ 6\times E \end{matrix} \\ \lambda \text{ free},\ \underline{x}_1^{soc} \in \mathcal{K} \end{cases} \tag{54}$$

For **plane strain**:

$$\lambda_h^{*LB} \equiv \max \lambda \quad s.t. \begin{cases} \overbrace{\begin{pmatrix} \underline{F}_h^{eq1} & \vdots & \underline{\underline{A}}^{eq1}\underline{\underline{P}} & \vdots & \underline{\underline{A}}^{eq1}\underline{Q} \\ \underline{F}_h^{eq2} & \vdots & \underline{\underline{A}}^{eq2}\underline{\underline{P}} & \vdots & \underline{\underline{A}}^{eq2}\underline{Q} \\ \underline{0} & \vdots & \underline{0} & \vdots & \underline{\underline{R}} \end{pmatrix}}^{\begin{matrix}1 & 3\times E & 9\times E\end{matrix}} \begin{pmatrix} \lambda \\ \underline{x}_4 \\ \underline{x}_2^{soc} \end{pmatrix} = \begin{pmatrix} \underline{0} \\ \underline{0} \\ \underline{\tilde{b}}_2^{soc} \end{pmatrix} \Bigg\} \begin{matrix} 2\times E \\ 4\times(|\mathcal{E}^{\mathcal{O}}|+|\mathcal{E}^{\mathcal{N}}|) \\ 3\times E \end{matrix} \\ \lambda \text{ free},\ \underline{x}_4 \text{ free},\ \underline{x}_2^{soc} \in \mathcal{K} \end{cases} \tag{55}$$

Notice that (54) involves $9\times E$ less unknowns and equations (plane stress), whereas (55) gives a reduction of $6\times E$ (plane strain). This represents a considerable gain in terms of computational performance. Figure 3 illustrates the reduction obtained in the problem size, when applied to the test example in plane stress.

4.2. The Upper Bound Problem

4.2.1. Purely Kinematic Spaces To obtain an upper bound, λ_h^{*UB}, the use of purely kinematic spaces is required. In this case, and unlike the lower bound problem, different finite element spaces are used to solve the plane stress and the plane strain models.

In **plane stress**, a continuous, piecewise linear, function element space, $Y_{h,1}^{UB} \subset Y$, is chosen to approximate the velocity field: $\mathbf{u} \approx \mathbf{u}_h \in Y_{h,1}^{UB}$ as:

$$u_i(x_1,x_2) = \sum_{A=1}^{N} u_i^A \phi_A(x_1,x_2), \quad i=1:2, \tag{56}$$

$$u_i^e(x_1,x_2) = \sum_{a=1}^{3} u_i^{a,e} N_a^e(x_1,x_2), \quad i=1:2, \tag{57}$$

where $\phi_A(\mathbf{x})$ are the linear, hat shape functions and $N_a^e(\mathbf{x})$ their restriction to the element e. The index $A=1:N$ represents a global numbering of the N nodes of the mesh; whereas a is its local counterpart. From (56), it should be clear that $Y_{h,1}^{UB}$ introduces $2\times N$ degrees of freedom in the displacement rates. Notice that there exists a mapping that relates the superscript a,e

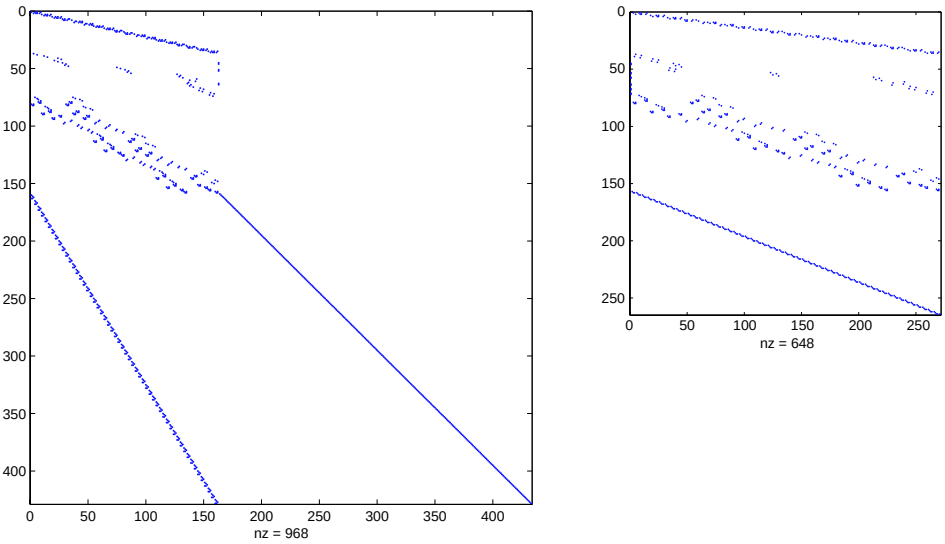

Figure 3. Comparison of the size of the global lower bound matrix for problems (52) and (54)

with the global numbering A. Consequently, for a given global node, A, shared by two adjacent elements, e and e', the following holds: $u_i^A = u_i^{a,e} = u_i^{b,e'}$ for a certain value of a and b from one to three. For the stresses, a piecewise constant function element space, $X_{h,1}^{UB} \subset X$, is chosen. The global interpolation is given by:

$$\sigma_i(x_1, x_2) = \sum_{e=1}^{E} \sigma_i^e \psi_e(x_1, x_2), \quad i = 1:3, \tag{58}$$

where $\psi_e(\mathbf{x}) = 1, \ \forall \mathbf{x} \in \Omega^e$ and 0 otherwise.

In **plain strain**, the velocity field is approximated by a discontinuous, piecewise linear, finite element space, $Y_{h,2}^{UB} \subset Y$, so that $\mathbf{u} \approx \mathbf{u}_h \in Y_{h,2}^{UB}$. Therefore, the displacements $\mathbf{u}_h$ are linear and continuous within an element, but discontinuities are allowed between elements. Clearly, $Y_{h,2}^{UB}$ introduces $6 \times E$ velocity unknowns. The choice of this interpolation is due to the necessity to introduce enough degrees of freedom so that incompressibility can be satisfied. The incompressibility condition, $\nabla \cdot \mathbf{u}_h = 0$, is a requirement in plane strain because the von Mises yield set, B_2, is unbounded (hydrostatic pressure has no influence on yield), which means that only incompressible flow fields have finite energy dissipation rate. In this case, it is convenient to work with a local interpolation, which is given by

$$u_i^e(x_1, x_2) \quad = \quad \sum_{a=1}^{3} u_i^{a,e} N_a^e(x_1, x_2), \quad i = 1:2, \tag{59}$$

Notice that (59) looks exactly like (57), but here each global node, A, does not have a single velocity vector associated to it.

For the stresses, a piecewise constant interpolation is used, as in the plane stress case:

$$\sigma_i(x_1, x_2) = \sum_{e=1}^{E} \sigma_i^e \psi_e(x_1, x_2), \quad i = 1:3, \tag{60}$$

However, an additional internal traction field, denoted by $\mathbf{t}_h$, needs also to be introduced. This field represents the tractions acting on the internal edges of the mesh and is independently parameterized from the stress field, $\boldsymbol{\sigma}_h$. These tractions are allowed to vary linearly along the internal edges as:

$$t_{i'}^{\xi_e^{e'}}(s) = \sum_{\alpha=1}^{2} t_{i'}^{\alpha,\xi_e^{e'}} N_\alpha^{\xi_e^{e'}}(s), \quad i' = 1':2'. \tag{61}$$

For convenience, the tractions will be expressed in a local coordinate system, $x_{1'}, x_{2'}$, different for each edge. To be consistent, let e denote the element on the left of the edge $\xi_e^{e'}$ and e', the element on the right, when one moves from the node $\alpha = 1$ of the edge to the node $\alpha = 2$. Then, $x_{1'}$ is normal to the edge and points towards e', whereas $x_{2'}$ follows the edge pointing towards the node $\alpha = 2$. For simplicity, $X_{h,2}^{UB}$ will denote the interpolation spaces chosen for both the stresses and the tractions.

Finally, to prove the purely kinematic nature of the interpolation spaces just introduced, one needs to show that when the continuous problem (10-13) is discretized using $X_{h,1}^{UB} \times Y_{h,1}^{UB}$ (plane stress) or $X_{h,2}^{UB} \times Y_{h,2}^{UB}$ (plane strain), the condition (22), or the less general condition (21), holds. This is shown in Appendix A.2.

4.2.2. Discretization Process Upper bounds are typically computed using the *kinematic principle of limit analysis* (13): $\lambda^* = \inf_{\mathbf{u}\in C} D(\mathbf{u})$. This principle is formulated in terms of velocities which, are implicitly required to satisfy the flow rule. The resulting problem is highly nonlinear and the approach does not exploit convexity nor duality in an explicit manner. Going back to Figure 1, the conventional approach corresponds to discretizing the kinematic principle with a flow interpolation and, then, solving exclusively the problem shown in the figure as *"Discrete Kinematic UB"*.

Here, a different approach has been chosen whereby the *static principle of limit analysis* (14) is discretized. Recall that, as shown in (14-17), the static and kinematic principles are dual each other and completely equivalent. Moreover, purely kinematic interpolation spaces are used for both the stresses and the velocities. Thus, the approach formulates the *"Discrete Static UB"*, which corresponds to the upper left branch of Figure 1. Additionally, the solution process is based on a primal-dual interior point method (see section 3), thereby explicitly considering the dual form. Note that following this approach there is no need to impose any restriction on the velocity field (like the flow rule or the normalization of the external work rate to unity), since the dual problem directly takes care of this. In summary, the approach computes an upper bound by discretizing the static principle of limit analysis by means of a purely kinematic discretization. This may not be the natural way of thinking, but mathematically is simpler and more efficient.

- **Equilibrium constraint in plane stress** To discretize the weak form of equilibrium, $a(\boldsymbol{\sigma}, \mathbf{u}) = \lambda F(\mathbf{u}), \forall \mathbf{u} \in Y$, one replaces the continuum fields $\boldsymbol{\sigma}$ and $\mathbf{u}$ by the global interpolations (56) and (58), respectively. The result of the discretization is given by the

following global matrix equation (see details in appendix C.1):

$$\underline{\underline{A}}^{eq}\underline{\tilde{\sigma}}_h = \lambda \underline{F}_h^{eq}, \tag{62}$$

where $\underline{\underline{A}}^{eq}$ is a matrix of dimensions $(2\times N, 3\times E)$, $\underline{F}_h^{eq}$ is a $2\times N$ vector of nodal forces and $\underline{\tilde{\sigma}}_h$ is a $3\times E$ vector of elemental stresses. Notice that the rows of $\underline{\underline{A}}^{eq}$ associated to the Dirichlet boundary nodes have been removed.

- **Equilibrium constraint in plane strain** In plane strain, discontinuities in the velocities between elements are allowed. Consequently, the definition of the internal work rate needs to be extended to consider the work occurring in the inter-element boundaries. Thus, the weak form of equilibrium reads as follows:

$$\begin{aligned} a(\boldsymbol{\sigma},\mathbf{t},\mathbf{u}) &= \lambda F(\mathbf{u}),\ \forall \mathbf{u}\in Y \\ \sum_{i,j=1}^{2}\int_\Omega \sigma_{ij}\frac{\partial u_i}{\partial x_j}\,dV + \sum_{\xi_e^{e'}\in\mathcal{E}^{\mathcal{O}}}\sum_{i'=1}^{2}\int_{\xi_e^{e'}} t_{i'}^{\xi_e^{e'}}\,(u_{i'}^{e'}-u_{i'}^{e})\,dS &= \lambda\sum_{i=1}^{2}\left(\int_\Omega f_i u_i\,dV + \int_{\Gamma^N} g_i u_i\,dS\right),\ \forall \mathbf{u}\in Y \end{aligned} \tag{63}$$

To discretize (63), the continuum spaces $X\times Y$ are replaced by the interpolation spaces $X_{h,2}^{UB}\times Y_{h,2}^{UB}$ defined by (59), (60) and (61). The details of the discretization process are given in Appendix C.2. Finally, the discrete version of the weak equilibrium equation (63) corresponds to the following global matrix equation:

$$\underline{\underline{\tilde{A}}}^{eq1}\underline{\tilde{\sigma}}_h + \underline{\underline{\tilde{A}}}^{eq2}\underline{t}_h = \lambda \underline{\tilde{F}}_h^{eq}, \tag{64}$$

where $\underline{\underline{\tilde{A}}}^{eq1}$ is a matrix of dimensions $(6\times E, 3\times E)$, $\underline{\underline{\tilde{A}}}^{eq2}$ has dimensions $(6\times E, 4\times|\mathcal{E}^{\mathcal{O}}|)$, $\underline{\tilde{\sigma}}_h$ is the usual $3\times E$ vector of elemental stresses, $\underline{t}_h$ is a $4\times|\mathcal{E}^{\mathcal{O}}|$ vector collecting the nodal tractions for each interior edge, and $\underline{\tilde{F}}_h^{eq}$ is a vector of $6\times E$ discontinuous nodal forces. Here also, the rows of $\underline{\underline{\tilde{A}}}^{eq1}$ and $\underline{\underline{\tilde{A}}}^{eq2}$ associated to the Dirichlet boundary nodes need to be removed.

- **Membership constraints. Formulation as multiple Second-order Cones** Discretizing the constraint $\boldsymbol{\sigma}\in B_\delta$ is straightforward, since X_h^{UB} consists of elementally constant stresses. It is therefore only necessary to impose, in each element, that the uniform stress tensor belongs to the admissible set:

$$(\sigma_1^e-\sigma_2^e)^2 + (\sigma_1^e)^2 + (\sigma_2^e)^2 + 6(\sigma_3^e)^2 \le 2\sigma_y^2 \qquad (\delta=1, \text{plane stress}) \tag{65}$$

$$(\sigma_1^e-\sigma_2^e)^2 + 4(\sigma_3^e)^2 \le \frac{4}{3}\sigma_y^2 \qquad (\delta=2, \text{plane strain}) \tag{66}$$

The above elemental constraints are exactly the same as the inequalities (46) and (47) in the lower bound problem, which were imposed in each of the three nodes of the element. Here, however, only E inequalities need to be imposed. For each inequality, the vectors $(\sqrt{2}\sigma_y, \sigma_1^e, \sigma_2^e, \sqrt{6}\sigma_3^e, \sigma_1^e-\sigma_2^e)$ or $(\frac{2}{\sqrt{3}}\sigma_y, 2\sigma_3^e, \sigma_1^e-\sigma_2^e)$ are forced to belong to the Lorentz cone $\mathcal{L}^n$, where $n=5$ for plane stress and $n=3$ for plane strain. This can be imposed by introducing a n-tuple elemental vector $\underline{\tilde{x}}^e$ of additional variables that satisfies the equations (48). Globally, this translates into $n\times E$ equations that are given, in matrix form, by the following equation:

$$\underline{\underline{\tilde{A}}}_\delta^{soc}\underline{\tilde{\sigma}}_h + \underline{\tilde{I}}_\delta\underline{\tilde{x}}_\delta^{soc} = \underline{\tilde{\tilde{b}}}_\delta^{soc}, \tag{67}$$

where $\underline{\tilde{\sigma}}_h$ is the usual $3 \times E$ vector of unknown elemental stresses, $\underline{\underline{\tilde{I}}}_\delta$ is a $(n \times E, n \times E)$ identity matrix, $\underline{\tilde{x}}^{soc}$ is a vector of $n \times E$ additional variables ordered in the same way as $\underline{\tilde{\sigma}}_h$, and $\underline{\tilde{\tilde{b}}}_\delta^{soc}$ and $\underline{\underline{\tilde{A}}}_\delta^{soc}$ are a $n \times E$ vector and a $(n \times E, 3 \times E)$ block diagonal matrix of the forms (51), respectively.

For plane strain, the condition $\mathbf{t}_h \in \tilde{B}_{2,h}$ must also be imposed, where $\tilde{B}_{2,h}$ is a set that places no restriction on the components of $\mathbf{t}_h$ that are normal to the inter-element edges, but forces the parallel components to satisfy the von Mises plane strain condition, $B_{2,h}$. The idea is to let the tangential tractions be as big as possible (in absolute value) within $B_{2,h}$, which is equivalent to restrict them to a pure shear state. Notice that, in the local coordinates $x_{1'}, x_{2'}$, a pure shear state makes the tangential tractions coincide with the shear stresses, σ_{12}. Clearly, $B_{2,h} \subset \tilde{B}_{2,h}$, as was required to obtain a purely kinematic discretization and, consequently, an upper bound. The motivation for this new set of admissible stresses is to guarantee that the resulting velocity field is kinematically admissible. Indeed, the fact that the normal tractions are not restricted will force the normal jump in the velocities to vanish in each internal edge.

To impose the constraint $\mathbf{t}_h \in \tilde{B}_{2,h}$, the components of $\mathbf{t}_h$ parallel to the edges must satisfy, for each edge $\xi_e^{e'}$ (denoted ξ in the next expressions), the following inequality: $(t_{2'}^{\alpha,\xi})^2 \leq \frac{1}{3}\sigma_y^2$, for $\alpha = 1:2$ or, equivalently, $-\frac{1}{\sqrt{3}}\sigma_y \leq t_{2'}^{\alpha,\xi} \leq \frac{1}{\sqrt{3}}\sigma_y$. These inequalities are imposed through the following equations:

$$\begin{cases} t_{2'}^{1,\xi} + s_1 = \frac{1}{\sqrt{3}}\sigma_y; & -t_{2'}^{1,\xi} + s_2 = \frac{1}{\sqrt{3}}\sigma_y; & s_1 \geq 0, s_2 \geq 0 & (\alpha = 1) \\ t_{2'}^{2,\xi} + s_3 = \frac{1}{\sqrt{3}}\sigma_y; & -t_{2'}^{2,\xi} + s_4 = \frac{1}{\sqrt{3}}\sigma_y; & s_3 \geq 0, s_4 \geq 0 & (\alpha = 2) \end{cases} \tag{68}$$

In matrix form, (68) reads as follows:

$$\begin{pmatrix} 0 & 1 & 0 & 0 \\ 0 & -1 & 0 & 0 \\ 0 & 0 & 0 & 1 \\ 0 & 0 & 0 & -1 \end{pmatrix} \begin{pmatrix} t_{1'}^{1,\xi} \\ t_{2'}^{1,\xi} \\ t_{1'}^{2,\xi} \\ t_{2'}^{2,\xi} \end{pmatrix} + \begin{pmatrix} 1 & 0 & 0 & 0 \\ 0 & 1 & 0 & 0 \\ 0 & 0 & 1 & 0 \\ 0 & 0 & 0 & 1 \end{pmatrix} \begin{pmatrix} s_1 \\ s_2 \\ s_3 \\ s_4 \end{pmatrix} = \frac{1}{\sqrt{3}}\sigma_y \begin{pmatrix} 1 \\ 1 \\ 1 \\ 1 \end{pmatrix}, \quad \text{or} \tag{69}$$

$$\underline{\underline{A}}_\xi^t \underline{t}_h^\xi + \underline{\underline{I}}^\xi \underline{s}^\xi = \underline{b}_\xi^t; \ \underline{s}^\xi \geq \underline{0}^\xi. \tag{70}$$

Finally, after the assembly process, (70) results in the following global equation:

$$\underline{\underline{A}}^t \underline{t}_h + \underline{\underline{I}}^t \underline{s} = \underline{b}^t; \quad \underline{s} \geq \underline{0}, \tag{71}$$

where $\underline{\underline{A}}^t$ is a block diagonal matrix of dimensions $(4 \times |\mathcal{E}^{\mathcal{O}}|, 4 \times |\mathcal{E}^{\mathcal{O}}|)$, $\underline{\underline{I}}^t$ is an identity matrix of the same dimensions, $\underline{t}_h$ is the previously introduced $4 \times |\mathcal{E}^{\mathcal{O}}|$ traction vector and s is a $4 \times |\mathcal{E}^{\mathcal{O}}|$ vector of slack variables.

4.2.3. The Upper Bound Problem as a SOCP Considering the equations (62) and (67) for plane stress, and (64), (67) and (71) for plane strain, the discretization of the upper bound problem (14) is obtained. For **plane stress** this gives:

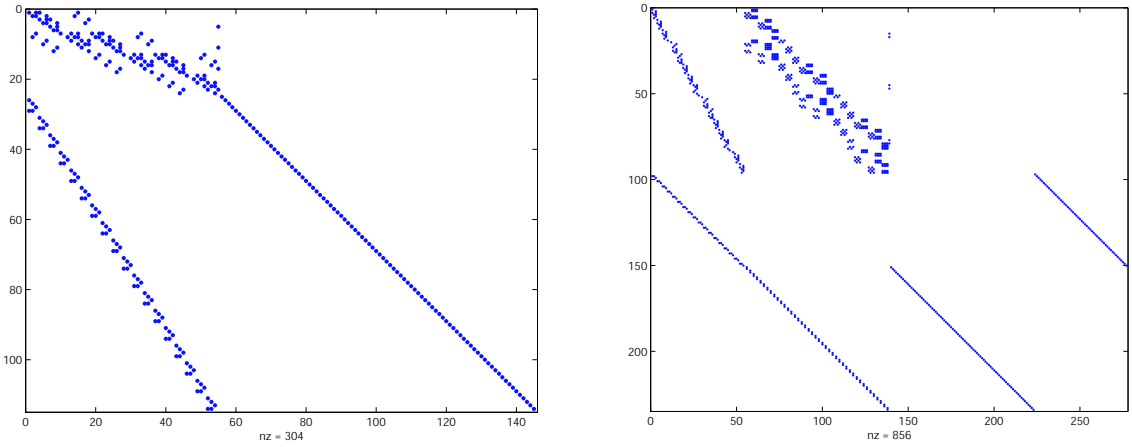

Plane stress Plane strain

Figure 4. Illustration of the structure and sparsity of the global matrix for the upper bound problem in plane stress and plane strain.

$$\lambda_h^{*UB} \equiv \max \lambda$$

$$s.t. \left\{ \begin{array}{l} \overbrace{\left(\begin{array}{ccccc} \underline{\underline{A}}^{eq} & \vdots & -\underline{\underline{F}}_h^{eq} & \vdots & \underline{\underline{0}} \\ \tilde{\underline{\underline{A}}}_1^{soc} & \vdots & \underline{\underline{0}} & \vdots & \tilde{\underline{\underline{I}}}_1 \end{array} \right)}^{3\times E \quad + \quad 1 \quad + \quad 5\times E} \left(\begin{array}{c} \tilde{\underline{\sigma}}_h \\ \lambda \\ \tilde{\underline{x}}_1^{soc} \end{array} \right) = \left(\begin{array}{c} \underline{0} \\ \tilde{\underline{b}}_1^{soc} \end{array} \right) \left\} \begin{array}{l} m_1 = 2 \times (N - N^{\mathcal{D}}) \\ m_2 = 5 \times E \end{array} \right. \\ \tilde{\underline{\sigma}}_h \text{ free}, \ \lambda \text{ free}, \ \tilde{\underline{x}}_1^{soc} \in \tilde{\mathcal{K}} \end{array} \right. \tag{72}$$

whereas for **plane strain**:

$$\lambda_h^{*UB} \equiv \max \lambda \tag{73}$$

$$s.t. \left\{ \begin{array}{l} \overbrace{\left(\begin{array}{ccccccc} \tilde{\underline{\underline{A}}}^{eq1} & \vdots & \tilde{\underline{\underline{A}}}^{eq2} & \vdots & -\tilde{\underline{\underline{F}}}_h^{\,eq} & \vdots & \underline{\underline{0}} \\ \tilde{\underline{\underline{A}}}_2^{soc} & \vdots & \underline{\underline{0}} & \vdots & \underline{\underline{0}} & \vdots & \underline{\underline{0}} \\ \underline{\underline{0}} & \vdots & \underline{\underline{A}}^{t} & \vdots & \underline{\underline{0}} & \vdots & \underline{\underline{I}}^{t} \end{array} \right.}^{3\times E \ + \ 4\times|\mathcal{E}^{\mathcal{O}}| \ + \ 1 \ + \ 4\times|\mathcal{E}^{\mathcal{O}}| \ + \ 3\times E} \left. \begin{array}{ccc} \vdots & \underline{\underline{0}} \\ \vdots & \tilde{\underline{\underline{I}}}_2 \\ \vdots & \underline{\underline{0}} \end{array} \right) \left(\begin{array}{c} \tilde{\underline{\sigma}}_h \\ \underline{t}_h \\ \lambda \\ \underline{s} \\ \tilde{\underline{x}}_2^{soc} \end{array} \right) = \left(\begin{array}{c} \underline{0} \\ \tilde{\underline{b}}_2^{soc} \\ \underline{b}^t \end{array} \right) \left\} \begin{array}{l} r_1 = 6 \times E - 4 \times |\mathcal{E}^{\mathcal{D}}| \\ r_2 = 3 \times E \\ r_3 = 4 \times |\mathcal{E}^{\mathcal{O}}| \end{array} \right. \\ \tilde{\underline{\sigma}}_h \text{ free}, \underline{t}_h \text{ free}, \ \lambda \text{ free}, \ \underline{s} \geq 0, \ \tilde{\underline{x}}_2^{soc} \in \tilde{\mathcal{K}} \end{array} \right.$$

where $\tilde{\mathcal{K}} = \overbrace{\mathcal{L}^n \times \cdots \times \mathcal{L}^n}^{E}$ ($n = 5$ for plane stress and $n = 3$ for plane strain) and $N^{\mathcal{D}}$ is the total number of Dirichlet nodes. Notice that the above problems present the canonical form of a conic program. The sparsity of their global matrices is illustrated, for the test example, in Figure 4. Thanks to strong duality, λ_h^{*UB} is also the solution of the problems dual to (72)

and (73). For **plane stress**, the dual to (72) is:

$$\lambda_h^{*UB} \equiv \min \tilde{\tilde{\underline{b}}}_1^{soc^T} \tilde{\underline{y}}$$
$$s.t. \left\{ \begin{array}{l} \left(\begin{array}{cc} \tilde{\tilde{\underline{A}}}^{eq^T} & \tilde{\tilde{\underline{A}}}_1^{soc^T} \\ -\underline{F}_h^{eq^T} & \underline{0}^T \end{array} \right) \left(\begin{array}{c} \underline{u} \\ \tilde{\underline{y}} \end{array} \right) = \left(\begin{array}{c} \underline{0} \\ 1 \end{array} \right) \left\} \begin{array}{l} 3 \times E \\ 1 \end{array} \right. \\ \underline{u} \text{ free}, \ \tilde{\underline{y}} \in \tilde{\mathcal{K}} \end{array} \right. , \tag{74}$$

where $\underline{u} \in \Re^{m_1}$, $\tilde{\underline{y}} \in \Re^{m_2}$ and for **plane strain**, the problem dual to (73) is:

$$\lambda_h^{*UB} \equiv \min \ \ \tilde{\tilde{\underline{b}}}_2^{soc^T} \underline{y}_1 + \underline{b}^{t^T} \underline{y}_2$$
$$s.t. \left\{ \begin{array}{l} \left(\begin{array}{ccc} \tilde{\tilde{\underline{A}}}^{eq1^T} & \tilde{\tilde{\underline{A}}}_2^{soc^T} & \underline{\underline{0}} \\ \tilde{\tilde{\underline{A}}}^{eq2^T} & \underline{\underline{0}} & \underline{\underline{A}}^{t^T} \\ -\underline{F}_h^{eq^T} & \underline{0}^T & \underline{0}^T \end{array} \right) \left(\begin{array}{c} \tilde{\underline{u}} \\ \underline{y}_1 \\ \underline{y}_2 \end{array} \right) = \left(\begin{array}{c} \underline{0} \\ \underline{0} \\ 1 \end{array} \right) \left\} \begin{array}{l} 3 \times E \\ 4 \times |\mathcal{E}^{\mathcal{O}}| \\ 1 \end{array} \right. \\ \tilde{\underline{u}} \text{ free}, \ \underline{y}_{\mathscr{2}} \geq \underline{0}, \ \underline{y}_{\mathscr{1}} \in \tilde{\mathcal{K}} \end{array} \right. , \tag{75}$$

where $\tilde{\underline{u}} \in \Re^{r_1}$, $\underline{y}_1 \in \Re^{r_2}$ and $\underline{y}_2 \in \Re^{r_3}$.

The equations and variables in the above dual problems have useful interpretations. For instance, in problem (74), the vector $\underline{u}$ are the nodal velocities (this vector is equivalent to the variables $\underline{u}^1$ and $\underline{u}^2$ in the lower bound dual problem (53), which represented elemental and inter-element velocities, respectively), whereas the vector $\underline{y}$ collects the plastic multipliers associated to the flow rule that govern the deformation of each element. Taking this into account and the fact that the vector $\tilde{\tilde{\underline{b}}}_1^{soc}$ incorporates the yield stress, σ_y, the cost function can be seen as an approximation to the total energy dissipation rate, $D(\mathbf{u})$. Finally, the first matrix equation approximately imposes the flow rule, whereas the second equation equates the approximated external work rate to the unity.

An analogous interpretation can be performed for problem (75). The vector $\tilde{\underline{u}}$ collects the nodal velocities associated to each element, which results in a global discontinuous velocity field. The vector $\underline{y}_1$ gives the nonnegative plastic multipliers involved in the flow rule of each element. Similarly, $\underline{y}_2$ collects nonnegative scalars that can be seen as plastic multipliers of an alternative flow rule for the tractions $\underline{t}_h$. Now, as previously, the cost function is an approximation to the energy dissipation rate $D(\mathbf{u})$. Notice that, in this case, there is an additional term, $\underline{b}^{t^T} \underline{y}_2$, which corresponds to the rate of energy dissipated at the inter-element boundaries. Clearly, this is due to the discontinuities in the flow. The first equation is the classical flow rule relating the deformation with the gradient of the yield function in each element. The second equation can be seen as another flow rule, but in this case for the jump in the velocities in each internal edge $\xi_e^{e'}$. More specifically, it forces two conditions: 1) it gives the magnitude of the jump in the velocities in the tangential direction, i.e., in the direction of the edge; 2) it imposes the jump in the velocities to be zero in the direction normal to the edge. Thus if two adjacent elements have different velocities, this last condition forces their relative displacement to be tangential, therefore resulting in a velocity field which is *kinematically admissible*. Finally, the third equation makes the external work rate equal to one.

4.2.4. Reduction of the dimensions of the global problem and transformation into a pure SOCP The same arguments used to reduce the dimensions of the global lower bound problem apply

here. Indeed, considering the change of coordinates (119) (plane stress) and (121) (plane strain) applied to an elemental stress vector, $\underline{\sigma}_h^e = (\sigma_1^e, \sigma_2^e, \sigma_3^e)^T$, the equilibrium constrains (62) (plane stress) and (64) (plane strain) can be written as follows:

$$\text{plane stress}: \qquad \underline{\underline{A}}^{eq}\tilde{\underline{\underline{Q}}}_1\tilde{\underline{x}}_1^{soc} - \underline{F}_h^{eq1}\lambda = \underline{0}, \qquad \text{with } \tilde{\underline{\sigma}}_h = \tilde{\underline{\underline{Q}}}_1\tilde{\underline{x}}_1^{soc} \tag{76}$$

$$\text{plane strain}: \quad \tilde{\underline{\underline{A}}}^{eq1}\tilde{\underline{\underline{P}}}\tilde{\underline{x}}_4 + \tilde{\underline{\underline{A}}}^{eq1}\tilde{\underline{\underline{Q}}}_2\tilde{\underline{x}}_2^{soc} + \tilde{\underline{\underline{A}}}^{eq}\underline{t}_h - \tilde{\underline{F}}_h^{eq}\lambda = \underline{0}, \quad \text{with } \tilde{\underline{\sigma}}_h = \tilde{\underline{\underline{P}}}\tilde{\underline{x}}_4 + \tilde{\underline{\underline{Q}}}_2\tilde{\underline{x}}_2^{soc} \tag{77}$$

where $\tilde{\underline{\underline{Q}}}_1, \tilde{\underline{\underline{Q}}}_2$ and $\tilde{\underline{\underline{P}}}$ are as in (124), but three times smaller. This is so because, in the upper bound problem, a single stress vector is considered per element (instead of three).

Analogously, using (125) (plane stress) and (126) (plane strain), the matrix equation that imposes the membership constraint in each element is written, for $\delta = 1:2$, as follows:

$$\tilde{\underline{\underline{R}}}_\delta\tilde{\underline{x}}_\delta^{soc} = \hat{\underline{b}}_\delta^{soc}, \tag{78}$$

where $\tilde{\underline{\underline{R}}}$ and $\hat{\underline{b}}_\delta^{soc}$ are as in (127), but again three times smaller for the same sake of argument.

Finally, considering (76),(77) and (78), the global problems (72) and (73) are equivalent to the following reduced forms. For **plane stress**:

$$\lambda_h^{*UB} \equiv \max \lambda$$
$$s.t. \begin{cases} \overbrace{\begin{pmatrix} -\underline{F}_h^{eq} & \vdots & \underline{\underline{A}}^{eq}\tilde{\underline{\underline{Q}}}_1 \\ \underline{0} & \vdots & \tilde{\underline{\underline{R}}}_1 \end{pmatrix}}^{1 \quad + \quad 5\times E} \begin{pmatrix} \lambda \\ \tilde{\underline{x}}_1^{soc} \end{pmatrix} = \begin{pmatrix} \underline{0} \\ \hat{\underline{b}}_1^{soc} \end{pmatrix} \Bigg\} \begin{matrix} 2\times(N-N^{\mathcal{D}}) \\ 2\times E \end{matrix} \\ \lambda \geq 0,\ \tilde{\underline{x}}_1^{soc} \in \tilde{\mathcal{K}} \end{cases} \tag{79}$$

and for **plane strain**:

$$\lambda_h^{*UB} \equiv \max \lambda \tag{80}$$
$$s.t. \begin{cases} \overbrace{\begin{pmatrix} \tilde{\underline{\underline{A}}}^{eq} & \vdots & \tilde{\underline{\underline{A}}}^{eq1}\tilde{\underline{\underline{P}}} & \vdots & -\tilde{\underline{F}}_h{}^{eq} & \vdots & \underline{\underline{0}} & \vdots & \tilde{\underline{\underline{A}}}^{eq1}\tilde{\underline{\underline{Q}}}_2 \\ \underline{\underline{0}} & \vdots & \underline{\underline{0}} & \vdots & \underline{0} & \vdots & \underline{\underline{0}} & \vdots & \tilde{\underline{\underline{R}}}_2 \\ \underline{\underline{0}} & \vdots & \underline{\underline{A}}^t & \vdots & \underline{0} & \vdots & \underline{\underline{I}}^t & \vdots & \underline{\underline{0}} \end{pmatrix}}^{4\times|\mathcal{E}^{\mathcal{O}}| \ + \ E \ + \ 1 \ + \ 4\times|\mathcal{E}^{\mathcal{O}}| \ + \ 3\times E} \begin{pmatrix} \underline{t}_h \\ \tilde{\underline{x}}_4 \\ \lambda \\ \underline{s} \\ \tilde{\underline{x}}_2^{soc} \end{pmatrix} = \begin{pmatrix} \underline{0} \\ \hat{\underline{b}}_2^{soc} \\ \underline{\underline{b}}^t \end{pmatrix} \Bigg\} \begin{matrix} 6\times E - 4\times|\mathcal{E}^{\mathcal{D}}| \\ E \\ 4\times|\mathcal{E}^{\mathcal{O}}| \end{matrix} \\ \underline{t}_h \text{ free}, \tilde{\underline{x}}_4 \text{ free}, \ \lambda \geq 0,\ \underline{s} \geq 0,\ \tilde{\underline{x}}_2^{soc} \in \tilde{\mathcal{K}} \end{cases}$$

Notice that, in plane stress, the change of coordinates allows for a reduction of $3 \times E$ less variables and equations, whereas in plane strain the reduction is of only $2 \times E$. Clearly, the gain achieved is less important than in the lower bound problem. However, an additional gain could be obtained in plane strain by exploiting further the same general idea and expressing the tangential components of $\underline{t}_h$ in terms of $\underline{s}$, using equations (68). This would permit a further reduction of $2 \times |\mathcal{E}^{\mathcal{O}}|$.

4.3. Solution of the Bound Problems

The above problems present the canonical form of a Conic Program and, in particular, their level of complexity is that of a Second-order Cone Program (SOCP). This is important

mainly for two reasons. First, it allows for the use of state of the art primal-dual interior point algorithms that have been particularly developed for SOCP and that guarantee global convergence and efficiency in the solution process. Moreover, with these algorithms, not only the above discrete static bound problems are solved, but also their duals, which are discrete versions of the kinematic principle. In this way, collapse fields for the stresses and velocities are simultaneously obtained. Second, the bound problems can be solved using any conic programming optimization package. In particular, the public domain conic solvers SeDuMi [30] and SDPT3 [31] are the ones used here.

5. MESH ADAPTIVITY

The objective of mesh adaptivity is to efficiently refine the computational mesh, $\mathcal{T}_h$, by only dividing the elements that make the largest contribution to the overall numerical error. In the problem considered here, the numerical error is measured by the *bound gap*, $\Delta_h = \lambda_h^{*UB} - \lambda_h^{*LB}$, for which it is possible to identify the contribution of each element in the mesh. Indeed, for both the plane stress and the plane strain cases, this elemental contribution, named *elemental bound gap*, is given by

$$\Delta_h^e = \underbrace{\int_{\Omega^e} \sigma_y \varepsilon_{eq}(\mathbf{u}_{UB}^e)}_{D^e(\mathbf{u}_{UB}^e)} - \underbrace{\left(\int_{\Omega^e} (-\nabla \cdot \boldsymbol{\sigma}_{LB}^e) \cdot \mathbf{u}_{UB}^e \, dV + \int_{\partial\Omega^e} (\mathbf{n}^{\xi_e} \cdot \boldsymbol{\sigma}_{LB}^e) \cdot \mathbf{u}_{UB}^e \, dS \right)}_{F^e(\mathbf{u}_{UB}^e)}. \tag{81}$$

In (81), $\boldsymbol{\sigma}_{LB}^e$ is the linear elemental stress tensor computed in the lower bound problem (52) and $\mathbf{u}_{UB}^e$ are the linear velocities, restricted to the element Ω^e, obtained when the upper bound problem (72) or (73) is solved. These elemental stress and velocity fields are illustrated in Figure 5. Furthermore, $\mathbf{n}^{\xi_e}$ is the unit outward normal vector acting on the edge ξ_e of a particular element and ε_{eq} is a scalar known as the *effective strain rate* given by:

$$\varepsilon_{eq}(\mathbf{u}) = \sqrt{\frac{2}{3} \boldsymbol{\varepsilon}'(\mathbf{u}) : \boldsymbol{\varepsilon}'(\mathbf{u})}, \tag{82}$$

where $\boldsymbol{\varepsilon}'$ is the deviatoric component of the strain rate tensor. Note that Δ_h^e is obtained as the difference between the total elemental energy dissipation rate, $D^e(\mathbf{u}_{UB}^e)$, and the elemental external work rate, $F^e(\mathbf{u}_{UB}^e)$, in both cases for the upper bound elemental velocity, $\mathbf{u}_{UB}^e$.

The elemental gap, Δ_h^e satisfies the following two important properties:

1. It is always positive, i.e., $\Delta_h^e \geq 0, \ \forall e \in \mathcal{T}_h$.

2. Its sum over all the elements equals the total bound gap, at least in the limit. In particular, for **plane stress**, the property holds strictly for each size of the mesh, h, i.e., $\sum_{e \in \mathcal{T}_h} \Delta_h^e = \Delta_h$. On the other hand, for **plane strain**, the property only holds in the limit. In this case, the total bound gap can be decomposed in two positive terms, namely, $\Delta_h = \Delta_h^{\mathcal{O}} + \bar{\Delta}_h$; where $\Delta_h^{\mathcal{O}}$ comes from the continuum (interior of the elements) and $\bar{\Delta}_h$ comes from the inter-element boundaries. With the previous definition of Δ_h^e, one can show that the sum of all the elemental bound gaps adds up to the total contribution from the continuum, i.e., $\sum_{e \in \mathcal{T}_h} \Delta_h^e = \Delta_h^{\mathcal{O}}$. Finally, $\bar{\Delta}_h$ is found, in practice, to converge to zero as the mesh is refined, i.e., $\bar{\Delta}_h \to 0$ when $h \to 0$.

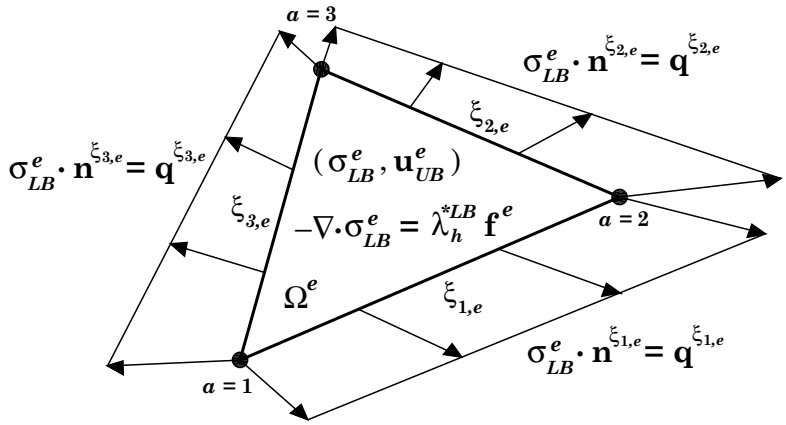

Figure 5. Notation for the elemental bound gap Δ_h^e

The above properties make Δ_h^e an effective indicator of the elemental contribution to the numerical error. Consequently, the strategy used here for mesh adaptivity consists of refining only the elements with higher Δ_h^e. In particular, *regular refinement* is used whereby the element to be refined is divided into 4 triangles by joining the midpoints of the sides. The resulting non-conformity is overcome by bisection of the adjacent triangles.

Proof of the above properties are given in the sections below.

5.1. Positiveness of Δ_h^e

Consider the individual element and the loading shown in Figure 5 as an isolated limit analysis problem. Recall that, in the lower bound problem, the stresses $\boldsymbol{\sigma}_{LB}$ are in equilibrium over the continuum and belong to the yield set B_δ, $\delta = 1:2$, at any point of the domain Therefore, the local problem shown in Figure 5 is also in equilibrium and satisfies the von Mises yield criterium. This is enough to guarantee, in accordance to the static principle, that the lower bound for this problem, $\lambda_h^{e,LB}$, is greater or equal than 1:

$$\lambda_h^{e,LB} \geq 1. \tag{83}$$

On the other hand, if the kinematic principle (13) is applied to the same elemental problem in Figure 5, using kinematically admissible velocity fields, $\mathbf{u}^e$, its upper bound, $\lambda_h^{e,UB}$, is equal to:

$$\lambda_h^{e,UB} = \inf_{\mathbf{u}^e} \frac{D^e(\mathbf{u}^e)}{F^e(\mathbf{u}^e)}. \tag{84}$$

In particular, choosing the continuous velocity field $\mathbf{u}^e_{UB}$ that results from the global upper bound problem, it is apparent that

$$\frac{D^e(\mathbf{u}^e_{UB})}{F^e(\mathbf{u}^e_{UB})} \geq \lambda_h^{e,UB}. \tag{85}$$

Finally, combining (85) with (83) one obtains:

$$\frac{D^e(\mathbf{u}^e_{UB})}{F^e(\mathbf{u}^e_{UB})} \geq \lambda_h^{e,UB} \geq \lambda_h^{e,LB} \geq 1 \implies \Delta_h^e = D^e(\mathbf{u}^e_{UB}) - F^e(\mathbf{u}^e_{UB}) \geq 0, \tag{86}$$

which proves the statement.

5.1.1. Sum of Δ_h^e To make the next proof easier to follow , it is convenient to recall first the following identities for the global upper bound, λ_h^{*UB}. In plane stress, for $\mathbf{u}_h \in X_{h,1}^{UB}$, one had:

$$\lambda_h^{*UB} = \min_{F(\mathbf{u}_h)=1} D(\mathbf{u}_h) = D(\mathbf{u}_{UB}), \tag{87}$$

being $\mathbf{u}_{UB} \in X_{h,1}^{UB}$ the optimal solution. In plane strain, the inter-element discontinuities had also to be considered in the internal work rate, as shown in (113). Therefore, for $\mathbf{u}_h \in X_{h,2}^{UB}$ and $(\boldsymbol{\sigma}_h, \mathbf{t}_h) \in Y_{h,2}^{UB}$, one had:

$$\begin{aligned}
\lambda_h^{*UB} &= \min_{F(\mathbf{u}_h)=1} \max_{\boldsymbol{\sigma}_h \in B_{h,2}, \mathbf{t}_h \in \tilde{B}_{h,2}} a(\boldsymbol{\sigma}_h, \mathbf{t}_h, \mathbf{u}_h) \\
&= \min_{F(\mathbf{u}_h)=1} \begin{cases} D(\mathbf{u}_h) + \sum_{\xi_e^{e'} \in \mathcal{E}^{\mathcal{O}}} \int_{\xi_e^{e'}} \tau_{max} |(\mathbf{u}_h^{e'} - \mathbf{u}_h^e) \cdot \boldsymbol{\tau}^{\xi_e^{e'}}| dS & \text{if} \quad (\mathbf{u}_h^{e'} - \mathbf{u}_h^e) \cdot \mathbf{n}^{\xi_e^{e'}} = 0, \ \forall \xi_e^{e'} \in \mathcal{E}^{\mathcal{O}} \\ \infty & \text{otherwise} \end{cases} \\
&= D(\mathbf{u}_{UB}) + \tau_{max} \sum_{\xi_e^{e'} \in \mathcal{E}^{\mathcal{O}}} \int_{\xi_e^{e'}} |(\mathbf{u}_{UB}^{e'} - \mathbf{u}_{UB}^e) \cdot \boldsymbol{\tau}^{\xi_e^{e'}}| dS = D(\mathbf{u}_{UB}) + \bar{D}(\mathbf{u}_{UB}),
\end{aligned} \tag{88}$$

where $\mathbf{n}^{\xi_e^{e'}}$ and $\boldsymbol{\tau}^{\xi_e^{e'}}$ represent orthonormal vectors, following the directions $x_{1'}$ and $x_{2'}$ (normal and tangential to the edge), $\tau_{max} = \frac{\sigma_y}{\sqrt{3}}$ given that the constraint $\mathbf{t}_h \in \tilde{B}_{h,2}$ implies $-\frac{1}{\sqrt{3}}\sigma_y \leq t_{2'}^{\alpha,\xi_e^{e'}} \leq \frac{1}{\sqrt{3}}\sigma_y$, for $\alpha = 1:2$ (see (68)), and $\bar{D}(\mathbf{u}_{UB})$ represents an inter-element energy dissipation rate.

In order to construct the proof, plane stress will be assumed. The proof can be easily extended to plane stress by setting to zero the inter-element terms. Adding the elemental contributions, one obtains:

$$\sum_{e \in \mathcal{T}_h} \Delta_h^e = \sum_{e \in \mathcal{T}_h} D^e(\mathbf{u}_{UB}^e) - \sum_{e \in \mathcal{T}_h} F^e(\mathbf{u}_{UB}^e) \tag{89}$$

The first term satisfies:

$$\sum_{e \in \mathcal{T}_h} D^e(\mathbf{u}_{UB}^e) = \sum_{e \in \mathcal{T}_h} \int_{\Omega^e} \sigma_y \varepsilon_{eq}(\mathbf{u}_{UB}^e) = \int_{\Omega} \sigma_y \varepsilon_{eq}(\mathbf{u}_{UB}) = D(\mathbf{u}_{UB}) = \lambda_h^{*UB} - \bar{D}(\mathbf{u}_{UB}), \tag{90}$$

where the last equality follows from (88)). For the second term, the following equalities hold:

$$\begin{aligned}
\sum_{e\in\mathcal{T}_h} F^e(\mathbf{u}^e_{UB}) &\overset{(1)}{=} \sum_{e\in\mathcal{T}_h}\left(\int_{\Omega^e}(-\nabla\cdot\boldsymbol{\sigma}^e_{LB})\cdot\mathbf{u}^e_{UB}\ dV + \int_{\partial\Omega^e}(\mathbf{n}^{\xi_e}\cdot\boldsymbol{\sigma}^e_{LB})\cdot\mathbf{u}^e_{UB}\ dS\right)\\
&\overset{(2)}{=} \sum_{e\in\mathcal{T}_h}\int_{\Omega^e}\lambda_h^{*LB}\mathbf{f}^e\cdot\mathbf{u}^e_{UB}\ dV + \sum_{e\in\mathcal{T}_h}\sum_{\xi_e\in\partial\Omega^e}\int_{\xi_e}\mathbf{q}^{\xi_e}_{LB}\cdot\mathbf{u}^e_{UB}\ dS\\
&\overset{(3)}{=} \lambda_h^{*LB}\sum_{e\in\mathcal{T}_h}\int_{\Omega^e}\mathbf{f}^e\cdot\mathbf{u}^e_{UB}\ dV + \lambda_h^{*LB}\sum_{\xi^N_e\in\mathcal{E}^{\mathcal{N}}}\int_{\xi^N_e}\mathbf{g}^{\xi^N_e}\cdot\mathbf{u}^e_{UB}\ dS +\\
&\quad + \sum_{\xi^{e'}_e\in\mathcal{E}^{\mathcal{O}}}\int_{\xi^{e'}_e}\mathbf{q}^{\xi^{e'}_e}_{LB}\cdot(\mathbf{u}^e_{UB}-\mathbf{u}^{e'}_{UB})dS\\
&\overset{(4)}{=} \lambda_h^{*LB}\left(\int_{\Omega}\mathbf{f}\cdot\mathbf{u}_{UB}\ dV + \int_{\Gamma^D}\mathbf{g}\cdot\mathbf{u}_{UB}\ dS\right) + \sum_{\xi^{e'}_e\in\mathcal{E}^{\mathcal{O}}}\int_{\xi^{e'}_e}\mathbf{q}^{\xi^{e'}_e}_{LB}\cdot(\mathbf{u}^e_{UB}-\mathbf{u}^{e'}_{UB})dS\\
&\overset{(5)}{=} \lambda_h^{*LB} + \sum_{\xi^{e'}_e\in\mathcal{E}^{\mathcal{O}}}\int_{\xi^{e'}_e} q^{\xi^{e'}_e}_{2',LB}(\mathbf{u}^e_{UB}-\mathbf{u}^{e'}_{UB})\cdot\boldsymbol{\tau}^{\xi^{e'}_e}\,dS. \qquad (91)
\end{aligned}$$

Equalities (1) and (4) are trivial. Equality (2) follows from (31). In equality (3) the integration is performed over all the edges ξ_e of all the elements. These edges can be either interior edges, $\xi^{e'}_e$, or boundary edges, ξ^D_e or ξ^N_e. For each interior edge, two integrals are computed, one for element e and another one for element e'. The inter-element stresses, $\mathbf{q}^{\xi^{e'}_e}_{LB}$, are of equal magnitude and opposite sign (see second constraint in problem (31)), which explains the third term in the equality (recall that in plane strain the displacements are discontinuous). Moreover, the integrals over the Dirichlet edges, ξ^D_e, vanish because $\mathbf{u}_{UB}$ is equal to zero. For the Neumann boundaries ξ^N_e, note that $\mathbf{q}^{\xi^N_e}_{LB} = \lambda_h^{*LB}\mathbf{g}^{\xi^N_e}$ (see third constraint in problem (31)). Finally, equality (5) holds because $F(\mathbf{u}_{UB}) = 1$ and $(\mathbf{u}^e_{UB}-\mathbf{u}^{e'}_{UB})\cdot\mathbf{n}^{\xi^{e'}_e} = 0$ ($\mathbf{u}_{UB}$ is forced to be kinematically admissible).

From (90) and (91), it is possible to conclude that:

$$\begin{aligned}
\sum_{e\in\mathcal{T}_h}\Delta^e_h &= \left(\lambda_h^{*UB}-\lambda_h^{*LB}\right) - \underbrace{\left(\bar{D}(\mathbf{u}_{UB}) + \sum_{\xi^{e'}_e\in\mathcal{E}^{\mathcal{O}}}\int_{\xi^{e'}_e} q^{\xi^{e'}_e}_{2',LB}(\mathbf{u}^e_{UB}-\mathbf{u}^{e'}_{UB})\cdot\boldsymbol{\tau}^{\xi^{e'}_e}\,dS\right)}_{\bar{\Delta}_h}\\
\sum_{e\in\mathcal{T}_h}\Delta^e_h &= \Delta_h - \bar{\Delta}_h. \qquad (92)
\end{aligned}$$

Observe that $\bar{\Delta}_h \geq 0$, since $q^{\xi^{e'}_e}_{2',LB} \leq \tau_{max}$. Now, if $\Delta^{\mathcal{O}}_h$ denotes the sum of the elemental bound gaps, it follows from (92) that $\Delta_h = \Delta^{\mathcal{O}}_h + \bar{\Delta}_h$, where $\Delta^{\mathcal{O}}_h = \sum_{e\in\mathcal{T}_h}\Delta^e_h \geq 0$. Additionally, all the computations performed show that, in practice, $\bar{\Delta}_h \to 0$ as $h \to 0$. This concludes the proof for the plane strain case.

Finally, in plane stress the velocity field is continuous, which implies that $\mathbf{u}^e_{UB} - \mathbf{u}^{e'}_{UB}|_{\xi^{e'}_e} = 0,\ \forall\xi^{e'}_e \in \mathcal{E}^{\mathcal{O}}$. Consequently, $\bar{\Delta}_h = 0$ and $\sum_{e\in\mathcal{T}_h}\Delta^e_h = \Delta_h$.

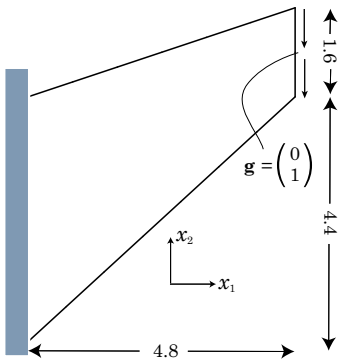

Figure 6. Geometry and loads for the cantilever problem in plane stress

6. NUMERICAL EXAMPLES

To assess the efficiency and accuracy of the method presented in the previous chapters, four two-dimensional examples are solved in plane stress and plane strain. For simplicity, and to make it possible to compare with known results, the volume forces are set to zero and the yield stress is chosen to be $\sigma_y = \sqrt{3}$. In the last section, the size of the problems and the computational time involved in the solution process are indicated.

6.1. Asymmetrical Cantilever in Plane Stress

In this example, an end-loaded wide tapered cantilever, for which an analytical solution does not seem to be known, is studied for the plane stress model. The geometry and load distribution are illustrated in Figure 6. The next sections show, first, the results obtained when the computational meshes are refined uniformly and, second, the results when mesh adaptivity is considered. Finally, the improvements of the mesh adaptive strategy are evaluated.

6.1.1. Uniform Meshing Table I summarizes the main results for five different uniform meshes that are obtained by refining the initial mesh. In each refinement, a triangle is divided into four smaller triangles. The lower and upper bound relative errors in the table are computed as

Uniform Meshing						
Number of refin.	Number of elem.	Low. Bound λ_h^{*LB}	Upp. Bound λ_h^{*UB}	Bound Gap Δ_h	Low. Bound Error (%)	Upp. Bound Error (%)
0	34	0.52186	0.75759	0.23573	23.821	10.591
1	136	0.65432	0.71936	0.06503	4.484	5.010
2	544	0.68079	0.69704	0.01624	0.620	1.752
3	2176	0.68349	0.68983	0.00634	0.226	0.699
4	8704	0.68440	0.68662	0.00223	0.093	0.231

Table I. Results for the cantilever problem in plane stress using uniform meshing

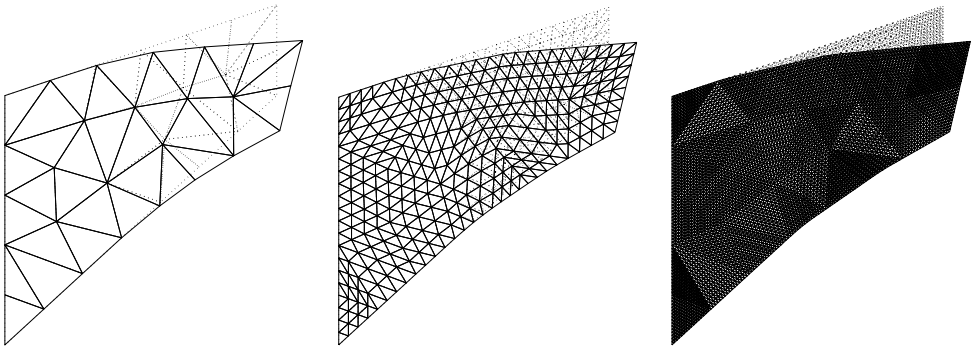

Figure 7. Cantilever problem - Deformed geometry

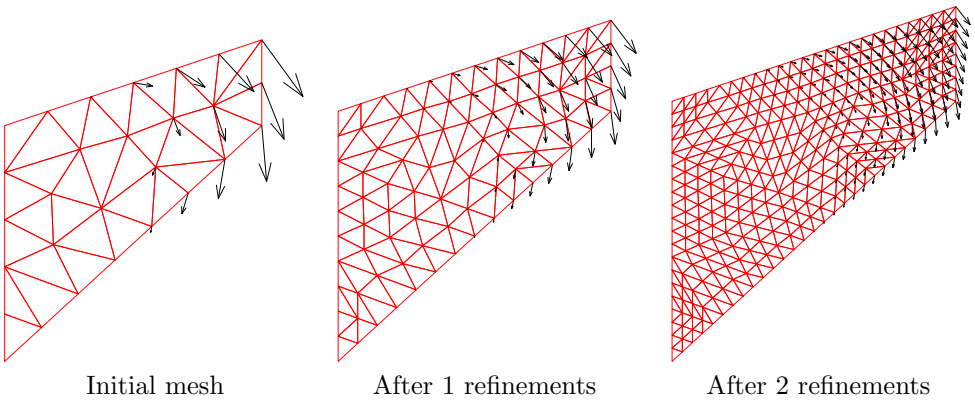

Figure 8. Cantilever problem - Nodal velocities

follows: $\frac{\lambda_h^{*UB}-\lambda^*}{\lambda^*}$ and $\frac{\lambda^*-\lambda_h^{*LB}}{\lambda^*}$, where λ^* is the unknown exact solution. In this case, λ^* has been assumed to be $\lambda^* = 0.68504$, which corresponds to the limit of convergence when very fine meshes are used.

Figure 7 illustrates the deformed geometry for different meshes, and Figure 8 shows the velocity field obtained from the upper bound computations. Notice that only the right hand side of the cantilever flows. Figure 9 shows graphically the bounds obtained for each refinement and, also, the rate of convergence for the bound errors and for the bound gap. After 4 refinements, with 8704 elements, the maximum relative error is only 0.231%. Moreover, the upper bound error presents a rate of convergence clearly higher than linear. On the other hand, the lower bound error converges linearly in the asymptotic range, despite the initial super-linear convergence.

6.1.2. Adaptive Meshing Table II shows the results obtained when the adaptive mesh procedure introduced in chapter 5 is used. In this case, five refinements of the original mesh have been performed. Notice that, with only 2450 elements, the maximum relative error is

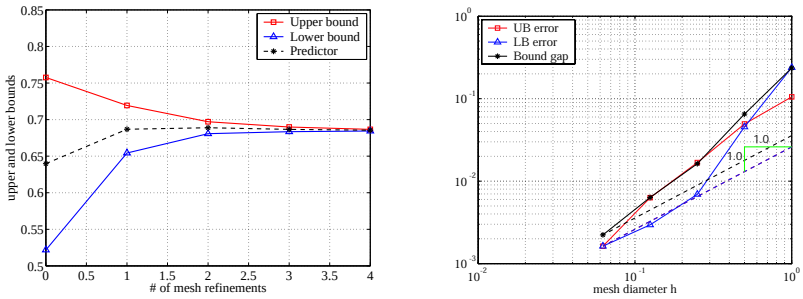

Upper and lower bounds Bound gape rate of convergence

Figure 9. Cantilever problem - Convergence

0.238%, practically the same as the one obtained previously with 8704 elements. Moreover, with 5506 elements, the error reduces to 0.066%, which can be considered negligible in practice.

Adaptive Meshing						
Number of refin.	Number of elem.	Low. Bound λ_h^{*LB}	Upp. Bound λ_h^{*UB}	Bound Gap Δ_h	Low. Bound Error (%)	Upp. Bound Error (%)
0	34	0.52186	0.75759	0.23573	23.821	10.591
1	90	0.65782	0.71951	0.06169	3.973	5.032
2	300	0.68079	0.69704	0.01625	0.620	1.752
3	882	0.68349	0.68989	0.00640	0.226	0.708
4	2450	0.68440	0.68667	0.00227	0.093	0.238
5	5506	0.68459	0.68549	0.00090	0.066	0.066

Table II. Results for the cantilever problem in plane stress using adaptive meshing

The deformed geometry is shown in Figure 10 for three different adaptive meshes. Moreover, Figure 11 shows the contribution of each element to the total bound gap. In Figure 12, the elements with higher contribution, which are the ones selected to be refined, are identified and filled in blue. As can be observed in Figure 10, the adaptive meshing strategy seems to capture very well the collapse mechanism, identifying four "slip-lines" that converge in a central plastic-hinge, thus dividing the cantilever in four regions (this mechanism is predicted by the "slip-line" theory in the symmetric cantilevers analyzed in [21]).

Figure 13 plots the upper and lower bounds computed for each mesh refinement. Note the accuracy obtained. Finally, Figure 14 compares the performance of the adaptive meshing strategy versus the uniform meshing. Clearly, the adaptive meshing outperforms the uniform refinement.

6.1.3. Comparison of the Elemental Bound Gap Adaptive Meshing Strategy with an Alternative, Deformation-based Strategy In [14], two alternative strategies for adaptive meshing are presented. The first one consists of refining only the elements whose deformation

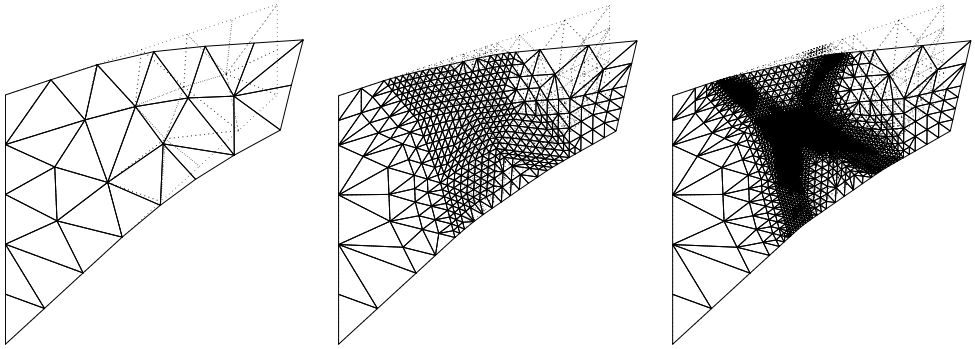

Figure 10. Cantilever problem - Deformed geometry using adaptive meshing

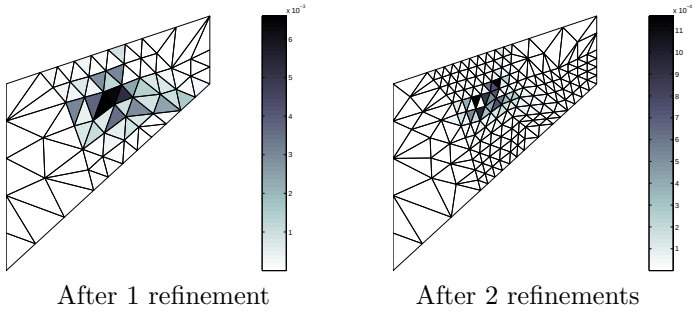

Figure 11. Cantilever problem - Elemental contribution to the bound gap Δ_h^e

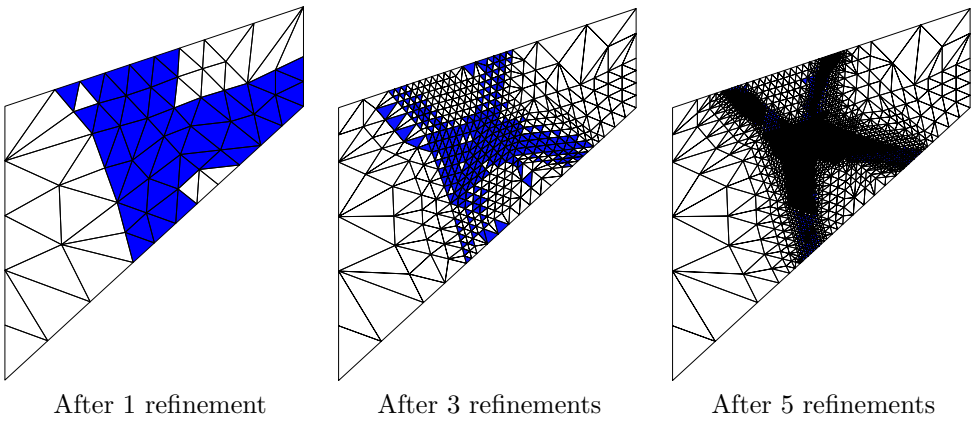

Figure 12. Cantilever problem - Adaptive meshing strategy: elements to be refined

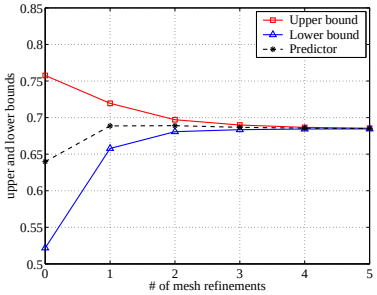

Figure 13. Cantilever problem - Bounds using adaptive meshing

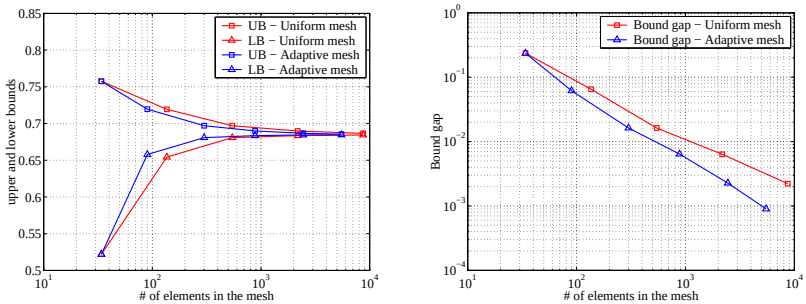

Upper and lower bounds Bound gap rate of convergence

Figure 14. Cantilever problem - Comparison of adaptive versus uniform meshing

is greater than a certain threshold. In the second strategy, a triangle is refined only if a certain number of its vertices are "sufficiently" close to the yield surface.

As mentioned in [14], the non-uniqueness of the collapse fields hampers the applicability of the above two conditions. Furthermore, the lack of a local error measure as a refinement criterium also undermines the optimality of the above strategies. On top of these two distinct strategies, two different refinement procedures are tried: the *regular refinement* (the refinement technique used in this article) and the *refinement by bisection of longest edge* [29]. The conclusion in [14] is that the strain strategy together with the regular refinement is, in practice, the best combination. Consequently, this is the adaptive meshing combination that is going to be compared with the elemental bound gap strategy presented in chapter 5.

More specifically, the strain strategy in [14] refines an element if the following inequality is satisfied:

$$||\boldsymbol{\varepsilon}_h^e|| = \sqrt{(\varepsilon_{11}^e)^2 + (\varepsilon_{22}^e)^2 + (\varepsilon_{12}^e)^2} > \delta \tag{93}$$

where $\boldsymbol{\varepsilon}_h^e$ is the strain tensor for element Ω^e and δ is a given threshold that, in this case, has been chosen to be $\delta = 0.005||\boldsymbol{\varepsilon}_h^e||_{\max}$[‡]. Figure 15 shows, for different adaptive meshes,

[‡]Similarly, in the adaptive meshing proposed in this article, the threshold chosen to refine an element has been:

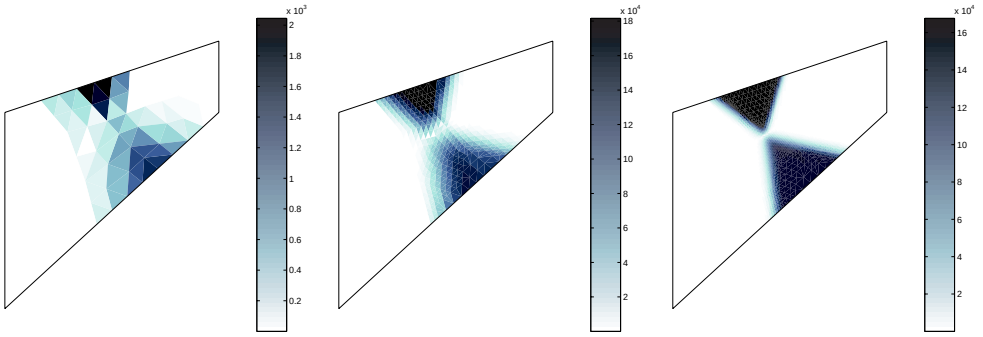

Figure 15. Cantilever problem - Elemental measure of deformation $||\boldsymbol{\varepsilon}_h^e||$

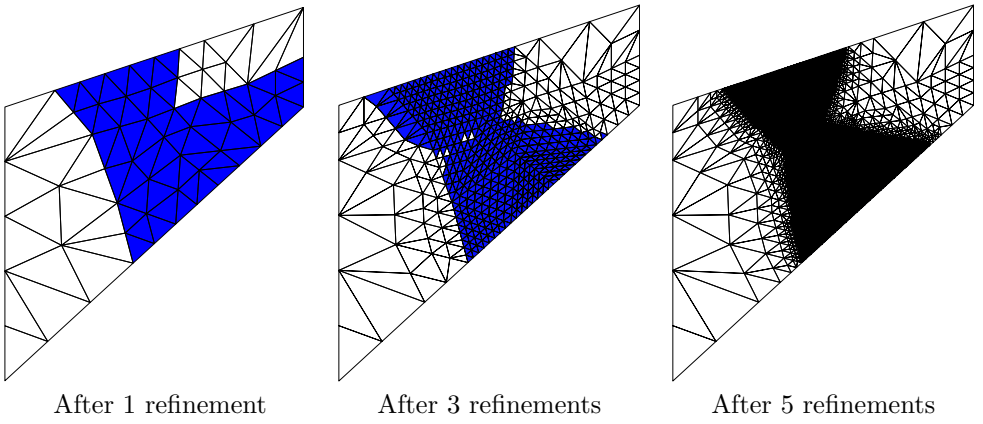

Figure 16. Cantilever problem - Alternative adaptive meshing strategy: elements to be refined

the elemental deformation measure $||\boldsymbol{\varepsilon}_h^e||$, upon which one decides the elements to be refined. Notice the difference between this figure and the equivalent one for the elemental bound gap strategy, Figure 11. As a result, the refined meshes are clearly different, as one can observe by comparing Figure 16 with Figure 12. It seems clear that the deformation-based meshing strategy is not able to capture the slip-lines in the collapse mechanism (as opposed to the elemental bound gap strategy), this way incurring in an unnecessary overrefining .

The numerical results are summarized in Table III. Additionally, Figure 17 illustrates the improved efficiency of the elemental bound gap strategy since, in all cases, fewer elements are required in the mesh to achieve a given bound gap.

$\Delta_h^e > 0.005\Delta_{h\max}^e$.

Alternative Adaptive Meshing						
Number of refin.	Number of elem.	Low. Bound λ_h^{*LB}	Upp. Bound λ_h^{*UB}	Bound Gap Δ_h	Low. Bound Error (%)	Upp. Bound Error (%)
0	34	0.52186	0.75759	0.23573	23.820	10.591
1	90	0.65782	0.71951	0.06170	3.973	5.032
2	304	0.68079	0.69704	0.01625	0.621	1.751
3	950	0.68349	0.68982	0.00634	0.227	0.698
4	3265	0.68440	0.68662	0.00223	0.094	0.231
5	11222	0.68457	0.68540	0.00083	0.069	0.053

Table III. Results for the cantilever problem in plane stress using an alternative, deformation-based, adaptive meshing strategy

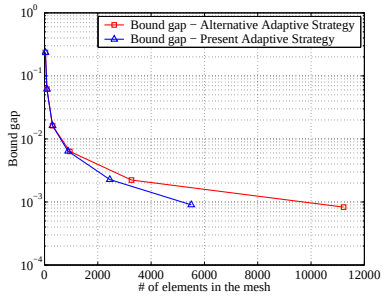

Figure 17. Cantilever problem - Bound gap rate of convergence for different adaptive meshing strategies

6.2. Slotted Square Block in Plane Stress

This example shows a square block with external thin symmetrical cuts, subject to a uniform tension in plane stress. The depth of the cut has been chosen to be 1/6 of the total height of the block. Figure 18 illustrates the problem. As in the previous example, the results corresponding to the uniform meshing approach are presented before those obtained with the proposed adaptive meshing strategy.

6.2.1. Uniform Meshing Table IV shows the bounds computed for six different uniform meshes. Notice that, in the last refinement, a very fine mesh consisting of 18432 elements is used. For this case, the resulting lower bound optimization problem has 258496 equations and 276481 variables, after reducing the original global problem by the introduction of a change of variables (see section 4.1.4). The upper bound problem results in 110816 equations and 147457 variables (without reducing the original global problem). The magnitude of these problems proves the capacity of the method to solve large, complex limit analysis problems. Since the exact collapse multiplier solution is not known for this example, the last column in the table corresponds to the maximum possible relative error, e_h, associated with the *predictor*, λ_h^{pr} (the average of the upper and lower bounds). Clearly, for each refinement, the exact solution belongs to the interval $\lambda_h^{pr} \pm e_h$.

Figures 19 and 20 illustrate the deformed geometry and the nodal velocities, respectively,

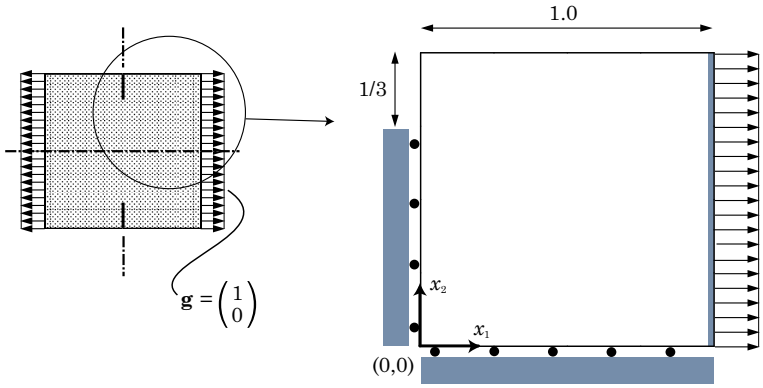

Figure 18. Geometry and loads for the slotted block problem in plane stress

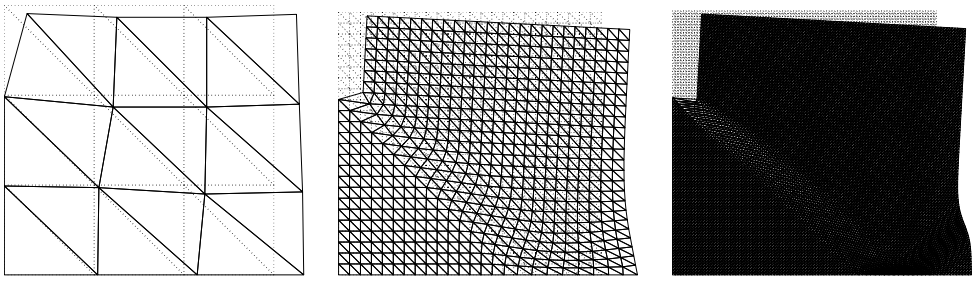

Figure 19. Slotted block problem 1 - Deformed geometry using uniform meshing

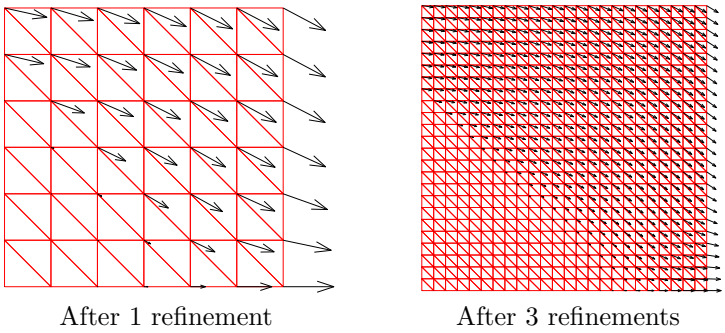

Figure 20. Slotted block problem 1 - Nodal velocities

for different computational meshes. Notice that the upper part of the domain moves as a rigid body, sliding over the lower left region, which remains static. Moreover, the lower right part is pushed horizontally by the upper region of the body. Finally, Figure 21 shows a linear rate of convergence for the bound gap, Δ_h.

Uniform meshing					
Number of refinements	Number of elements	Lower Bound λ_h^{*LB}	Upper Bound λ_h^{*UB}	Bound Gap Δ_h	Max. Rel. Error, e_h (%)
0	18	1.0414	1.5690	0.52765	20.213
1	72	1.1830	1.4408	0.25774	9.823
2	288	1.2352	1.3619	0.12662	4.876
3	1152	1.2553	1.3183	0.06303	2.449
4	4608	1.2639	1.2960	0.03206	1.252
5	18432	1.2679	1.2844	0.01643	0.644

Table IV. Results for the slotted block problem in plane stress using uniform meshing

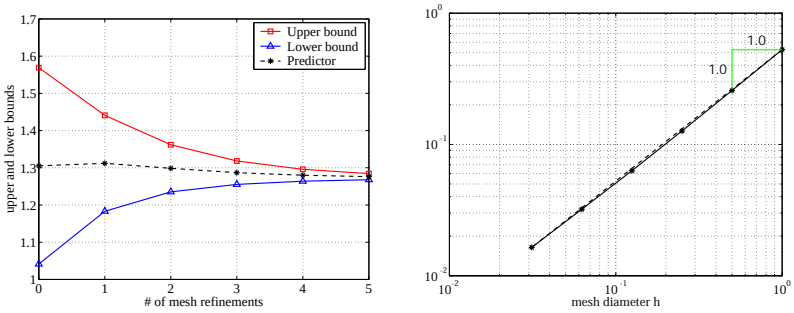

Upper and lower bounds Bound gap rate of convergence

Figure 21. Slotted block problem 1 - Convergence using uniform meshing

6.2.2. Adaptive Meshing Nine refinements of the initial mesh have been considered, for which the results are given, numerically, in Table V. These results are also shown, graphically, in Figure 24. The adaptive meshing is found to capture the collapse mechanism very accurately, as can be observed in Figures 22 and 23. Finally, Figure 25 shows the efficiency of the adaptive meshing when compared to the uniform meshing. Indeed, the rate of convergence for the bound gap is much higher in the adaptive case. Notice also that in the sixth adaptive refinement, with 1550 elements, a bound gap of only 0.01515 is obtained. In the uniform meshing, the finer mesh yielded a bound gap of 0.01643 and used 18435 elements. In the last adaptive refinement (5568 elements), the bound gap reduces to 0.00490, which translates into a maximum error of 0.192%.

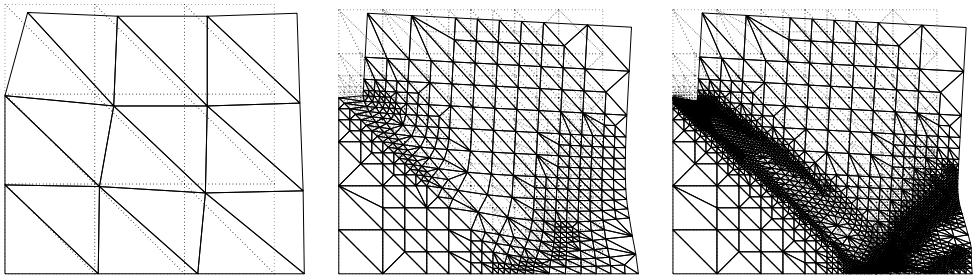

Figure 22. Slotted block problem 1 - Deformed geometry using adaptive meshing

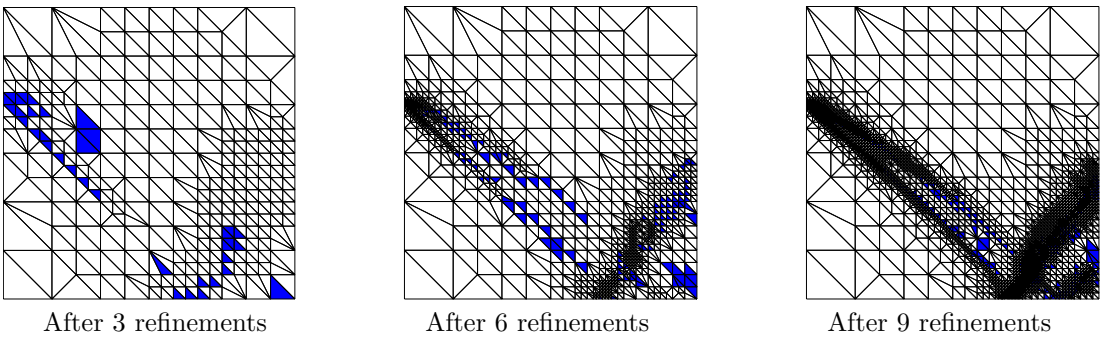

Figure 23. Slotted block problem 1 - Adaptive meshing strategy: elements to be refined

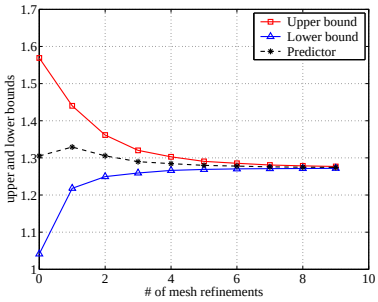

Figure 24. Slotted block problem 1 - Bounds using adaptive meshing

Adaptive meshing					
Number of refinements	Number of elements	Lower Bound λ_h^{*LB}	Upper Bound λ_h^{*UB}	Bound Gap Δ_h	Maximum Error (%)
0	18	1.0414	1.5690	0.52765	20.213
1	70	1.2181	1.4402	0.22206	8.353
2	254	1.2496	1.3615	0.11190	4.285
3	483	1.2593	1.3202	0.06095	2.363
4	714	1.2663	1.3028	0.03654	1.422
5	1082	1.2690	1.2907	0.02173	0.849
6	1550	1.2703	1.2855	0.01515	0.593
7	2538	1.2710	1.2808	0.00979	0.384
8	3564	1.2714	1.2785	0.00705	0.276
9	5568	1.2719	1.2768	0.00490	0.192

Table V. Results for the slotted block problem in plane stress using adaptive meshing

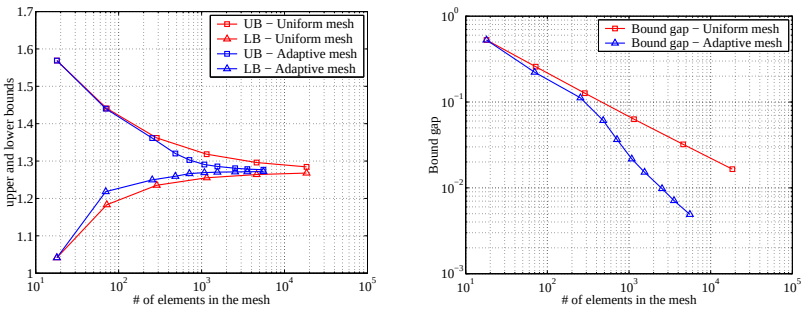

Upper and lower bounds Bound gap rate of convergence

Figure 25. Slotted block problem 1 - Comparison of adaptive versus uniform meshing

6.3. Square section with cut outs in Plane Strain

This example studies a section with cut outs subject to uniform tension in plane strain. The section is square and has two symmetrical rectangular holes. Figure 26 shows the computational domain and loads considered, as well as the initial finite element mesh. The nontrivial geometry makes this example a good test to assess the accuracy of the method in plane strain, as well as the efficiency of the adaptive meshing technique to capture the collapse mechanism. To the authors knowledge, no analytical solution is known.

6.3.1. Uniform Meshing The numerical results are given in Table VI. Notice that, for the finest mesh, e_h is only 1.012%. Figure 27 shows the deformation of the body at collapse for both the initial and the final meshes considered. Recall that, in plane strain, the velocities are interpolated using piecewise discontinuous linear spaces, but are explicitly forced to be kinematically admissible. Consequently, adjacent triangles can only slide over each other, as can be observed in the figure.

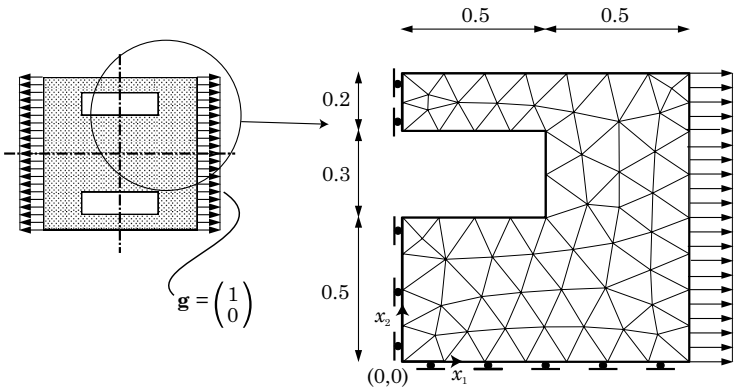

Figure 26. Geometry and loads for the square section problem in plane strain

Uniform meshing					
Number of refinements	Number of elements	Lower Bound λ_h^{*LB}	Upper Bound λ_h^{*UB}	Bound Gap Δ_h	Max. Rel. Error, e_h (%)
0	108	1.2913	1.4151	0.12379	4.574
1	432	1.3195	1.3837	0.06419	2.375
2	1728	1.3215	1.3631	0.04163	1.551
3	6912	1.3219	1.3490	0.02703	1.012

Table VI. Results for the square section problem in plane strain using uniform meshing

Finally, Figure 28 illustrates the bounds computed for the four uniform meshes under consideration, and shows, also, a sub-linear rate of convergence for the bound gap. This behavior will also appear in the next example, where plane strain is also assumed. Recall that, in plane stress, the rate of convergence for the bound gap was, at least, linear (see Figures 21 and 9). This seems to suggest that, in terms of convergence, plane stress behaves better than plane strain.

6.3.2. Adaptive Meshing When adaptive meshing is considered, the results improve substantially, as shown in Table VII. For instance, with 4788 elements (after 5 refinements), $e_h = 0.464\%$. This error is less than half of the error incurred in the finest uniform mesh, consisting of 6912 elements.

The deformed geometries in Figure 29, especially the last one, indicate that the main plastic deformations are concentrated within a thin region around a 45° inclined line, with origin in the lower right corner of the interior hole. This plastified region acts as a slip-line over which the upper part of the body flows. Also, some plastic deformations can be encountered in the thin region located over the hole. As shown in Figures 30 and 31, the adaptive mesh procedure captures very well the plastified regions and concentrates the refinement in those areas.

The upper and lower bounds obtained for each adaptive mesh are shown, graphically, in

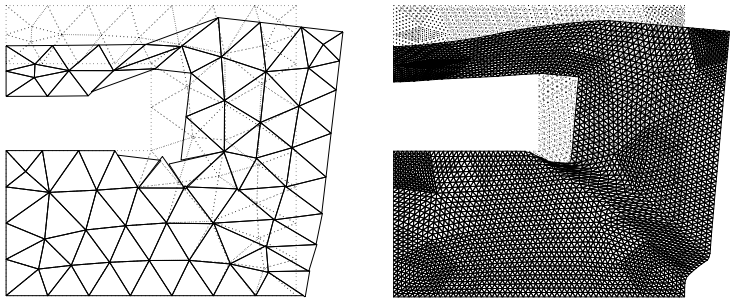

Initial mesh After 3 refinements

Figure 27. Square section problem - Deformed geometry

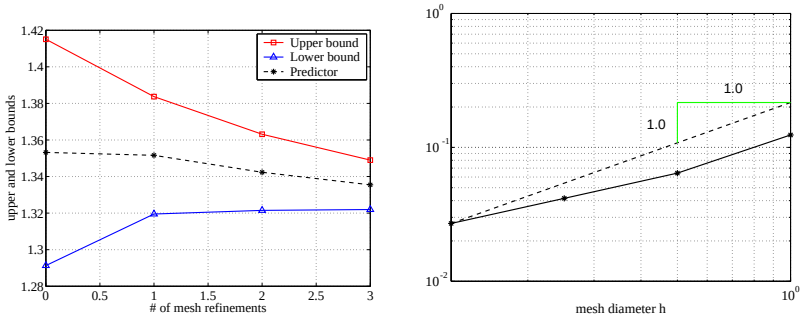

Upper and lower bounds Bound gap rate of convergence

Figure 28. Square section problem - Convergence

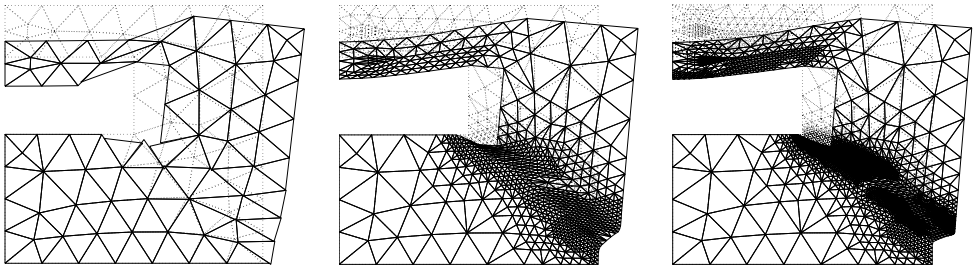

Initial mesh After 3 refinements After 5 refinements

Figure 29. Square section problem - Deformed geometry using adaptive meshing

Adaptive meshing					
Number of refinements	Number of elements	Lower Bound λ_h^{*LB}	Upper Bound λ_h^{*UB}	Bound Gap Δ_h	Max. Rel. Error (%)
0	108	1.2913	1.4151	0.12379	4.574
1	251	1.3128	1.3837	0.07088	2.628
2	645	1.3208	1.3632	0.04246	1.582
3	1354	1.3216	1.3493	0.02762	1.034
4	2444	1.3218	1.3402	0.01844	0.693
5	4788	1.3219	1.3342	0.01232	0.464

Table VII. Results for the square section problem in plane strain using adaptive meshing

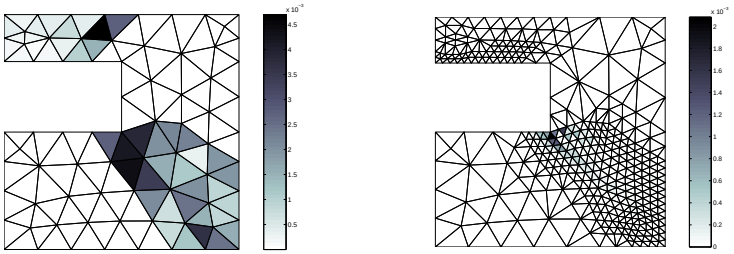

Initial mesh After 2 refinements

Figure 30. Square section problem - Elemental contribution to the bound gap Δ_h^e

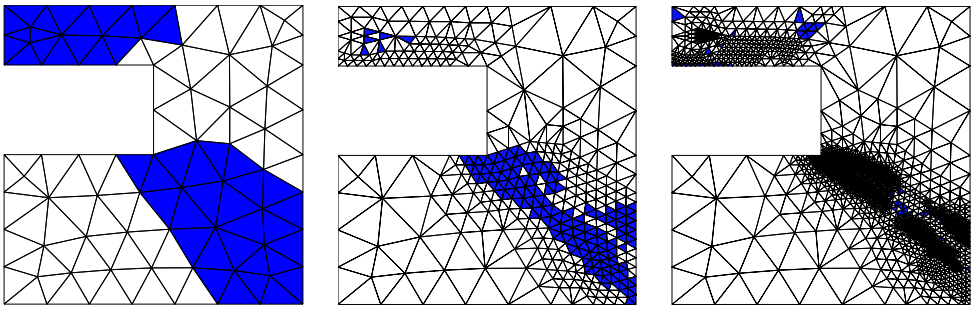

Initial mesh After 2 refinements After 5 refinements

Figure 31. Square section problem - Adaptive meshing strategy: elements to be refined

Figure 32. Although the exact solution is not known, the lower bound appears to converge faster than the upper bound. This observation is confirmed in the fourth example. Hence, it seems that, in plane strain, the lower bound has a higher rate of convergence than the upper bound. As shown in the first and second examples, this was not the case in plane stress. Finally, Figure 33 illustrates the gain obtained when mesh adaptivity is used. For instance, one can observe that the bound gap resulting from the third adaptive mesh is of the same order as that

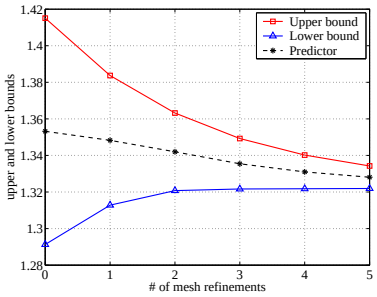

Figure 32. Square section problem - Bounds using adaptive meshing

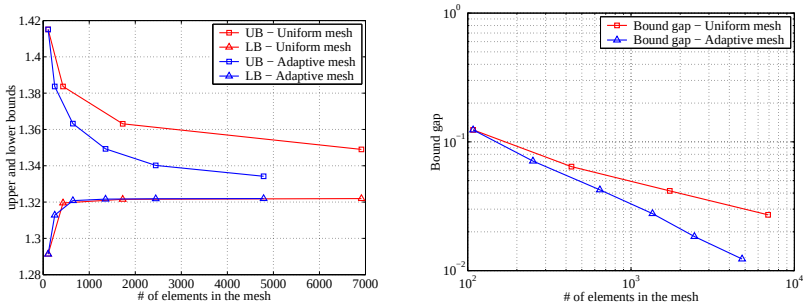

Upper and lower bounds Rate of convergence

Figure 33. Square section problem - Comparison of adaptive versus uniform meshing

obtained with the finest uniform mesh. However, in the adaptive case, the mesh has only 1354 elements, much less than the 6912 elements of the uniform mesh. Thus, with only 19.6% of the elements, the same accuracy is obtained. For the lower bound problem, this translates into 15024 equations and 16249 unknowns in the adaptive case, to be compared to 76432 equations and 82945 unknowns for the uniform case. Moreover, the gain in terms of the time involved in the solution of the optimization problems is even more dramatic.

6.4. Slotted Square Block in Plane Strain

Very similar to the second example, the slotted square block considered here has a cut of 1/4 of the total height of the block, as shown in Figure 34, and is solved assuming plane strain. This example is a classical problem and is well documented in the literature. In particular, it has been studied in [12](main reference), [10], [4], [11], [6], [14] or, more recently, in [19]. Although a rigorous exact solution is not available, the extrapolated value $\lambda^* = 1.13156$, derived in [12], is considered here as a sufficiently accurate solution. This problem is very appropriate to achieve different purposes: i) verify the correctness of the method in plane strain, ii) address convergence studies for various cases, iii) compare the results with those of other sources and iv) show the relevance that the choice of the computational mesh might have on the accuracy of the results. In particular, to illustrate the fourth point, the same problem is solved starting from three different initial meshes, which are shown in Figure 35 and denoted by $\mathcal{T}_{h,1}$, $\mathcal{T}_{h,2}$

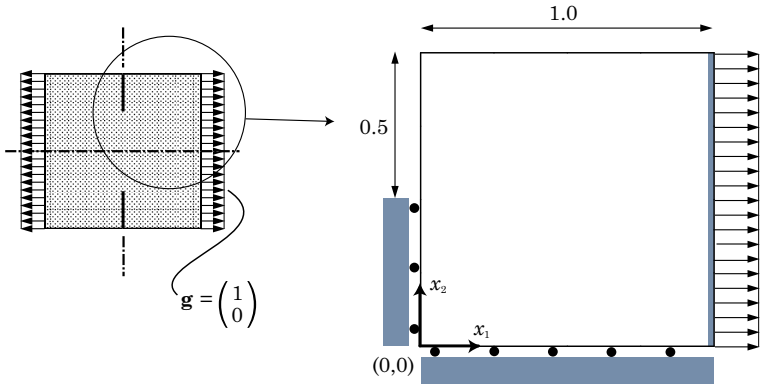

Figure 34. Geometry and loads for the slotted block problem in plane strain

and $\mathcal{T}_{h,3}$. Notice that, in all the meshes, the edges of the elements define preferential directions in the domain.

6.4.1. Uniform Meshing For the three meshes under consideration, the numerical results are summarized in Table VIII and the collapse geometries, given in Figure 35. Moreover, Figures 36 and 37 show, respectively, the upper and lower bounds obtained and, also, the rate of convergence for the bound gap as well as for the upper and lower bound relative errors. Notice that the accuracies obtained for the different meshes differ substantially. Indeed, in terms of bound gap and with only half of the elements, $\mathcal{T}_{h,3}$ outperforms $\mathcal{T}_{h,2}$ which, in turn, works better than $\mathcal{T}_{h,1}$. These results are not surprising, as explained next. Since the collapse mechanisms are typically highly localized, one can expect better solutions if the preferential directions of the meshes match, or are similar, to the slip-lines of the real mechanism. In this problem, two slip-lines exist. The main one has its origin at the end of the cut and goes down to a point near the right boundary, describing a logarithmic spiral. From this point, a second discontinuity develops following a direction perpendicular to the previous main slip-line. Then, one expects $\mathcal{T}_{h,2}$ to work better than $\mathcal{T}_{h,1}$, since its preferential direction is similar to the main slip-line of the mechanism, whereas in $\mathcal{T}_{h,1}$ the preferential direction only matches the second, less important, slip-line. Finally, $\mathcal{T}_{h,3}$ has to be the best mesh, since more flexibility is introduced and the elements can slide in both directions.

Besides the mesh phenomenon, it is also remarkable that the errors in the lower bound are clearly inferior to the upper bound ones. This agrees with the observation made in the Beam Example. In the same line, Figure 37 shows that the rate of convergence for the bound gap is, for all cases, sub-linear, as was also observed in the Beam Example. This is due to the poor convergence rate of the upper bound error, since the lower bound error converges, at least, linearly. Notice the extraordinary accuracy and rate of convergence obtained in the lower bound problem for the mesh $\mathcal{T}_{h,3}$: after 4 refinements, the lower bound error is only 0.0076% and its rate of convergence is found to be quadratic.

6.4.2. Adaptive Meshing When mesh adaptivity is used, previous observations are even more valid. In this respect, $\mathcal{T}_{h,3}$ continues to behave clearly better than $\mathcal{T}_{h,2}$ and $\mathcal{T}_{h,1}$, as can be

Uniform meshing with initial mesh $\mathcal{T}_{h,1}$						
Number of refin.	Number of elem.	Low. Bound λ_h^{*LB}	Upp. Bound λ_h^{*UB}	Bound Gap Δ_h	Low. Bound Error (%)	Upp. Bound Error (%)
0	32	0.9952	1.3688	0.37355	12.051	20.966
1	128	1.0760	1.2840	0.20797	4.910	13.472
2	512	1.1069	1.2240	0.11716	2.179	8.169
3	2048	1.1198	1.1862	0.06647	1.039	4.829
4	8192	1.1258	1.1641	0.03833	0.509	2.876

Uniform meshing with initial mesh $\mathcal{T}_{h,2}$						
Number of refin.	Number of elem.	Low. Bound λ_h^{*LB}	Upp. Bound λ_h^{*UB}	Bound Gap Δ_h	Low. Bound Error (%)	Upp. Bound Error (%)
0	32	0.9109	1.2444	0.33344	19.496	9.972
1	128	1.0341	1.2061	0.17193	8.613	6.587
2	512	1.0871	1.1784	0.09128	3.929	4.139
3	2048	1.1103	1.1601	0.04976	1.879	2.522
4	8192	1.1212	1.1489	0.02770	0.916	1.532

Uniform meshing with initial mesh $\mathcal{T}_{h,3}$						
Number of refin.	Number of elem.	Low. Bound λ_h^{*LB}	Upp. Bound λ_h^{*UB}	Bound Gap Δ_h	Low. Bound Error (%)	Upp. Bound Error (%)
0	16	1.11405	1.22888	0.114830	1.5478	8.6001
1	64	1.12690	1.20063	0.073735	0.4119	6.1044
2	256	1.13046	1.17785	0.047395	0.0973	4.0911
3	1024	1.13126	1.16057	0.029304	0.0262	2.5636
4	4096	1.13147	1.14956	0.018082	0.0076	1.5904

Table VIII. Results for the slotted block problem in plane strain using uniform meshing

observed in Table IX and in Figures 39 and 40 . Also, the upper bound is consistently less accurate than the lower bound and has a worst convergence rate. Furthermore, $\mathcal{T}_{h,3}$ yields an outstanding accuracy for the lower bound, with a final relative error of only 0.0021%. It is interesting to compare, in Figure 38, the meshes $\mathcal{T}_{h,1}$ and $\mathcal{T}_{h,2}$ after five refinements. Notice that, in the first case, the refinement is principally concentrated in a wide region around the main slip-line (the one starting from the cut and going down to the right side), and less refinement is performed around the second slip-line (the one in the lower right corner). However, in $\mathcal{T}_{h,2}$, the refinement is very thin around the main slip-line, and a dense refinement is necessary to capture the second slip-line, whose direction is perpendicular to the edges of the mesh. This clearly agrees with the expected relevance of the preferential directions.

Figure 40 compares the rate of convergence for both the lower bound error and the bound gap, for the three meshes considered under uniform and adaptive meshing. Clearly, mesh adaptivity permits gains in both accuracy and convergence. Also, the impact of the initial mesh is proved.

6.4.3. Comparison of the Results with other Approaches The results obtained for this example are now compared with those given in two recent sources, [12, 19].

In reference [12], a mixed formulation stress-velocities is used to approximate, but not bound, the collapse multiplier. Linear, continuous interpolations are chosen for both the stresses and

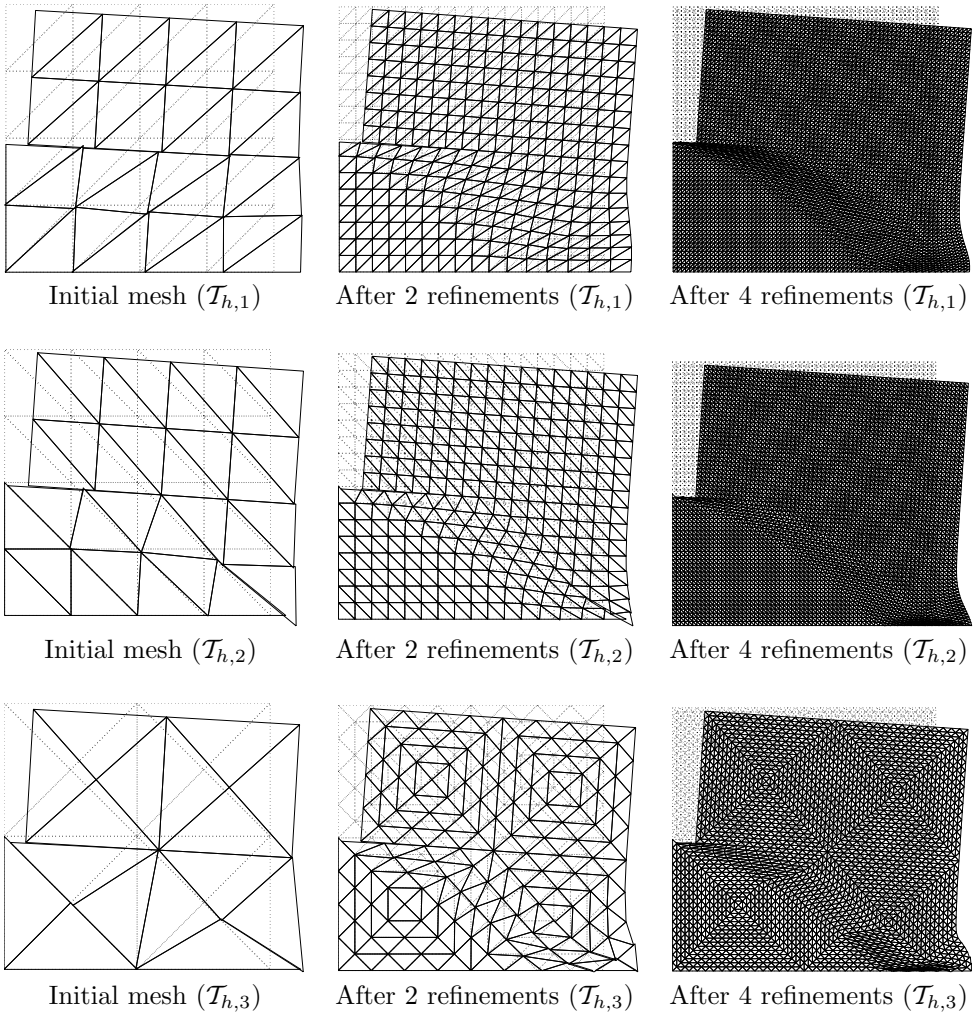

Figure 35. Slotted block problem 2 - Deformed geometry using uniform meshing

the velocities on a triangular finite element mesh whose triangles are oriented as in the mesh $\mathcal{T}_{h,2}$. The best estimate obtained for λ^* is 1.13582, for a mesh of 115200 elements. When using a coarser mesh of 7200 elements, the estimate is 1.1485. Notice that this value is worse than the upper bound obtained when adaptive meshing is applied to the initial mesh $\mathcal{T}_{h,2}$. Indeed, with only 4621 elements, the value obtained is 1.1428. Moreover, the method proposed in this article yields a strict upper bound, as opposed to just an approximation. The rate of convergence in [12] is linear, which coincides with our results.

In [19], the problem is solved using a lower bound formulation based on a discontinuous, piecewise linear interpolation of the stresses (the same formulation used here for the lower bound problem). The initial mesh considered is of the type $\mathcal{T}_{h,3}$, which explains the quadratic rate of convergence reported when refining the mesh uniformly. Recall (see Figure 37) that

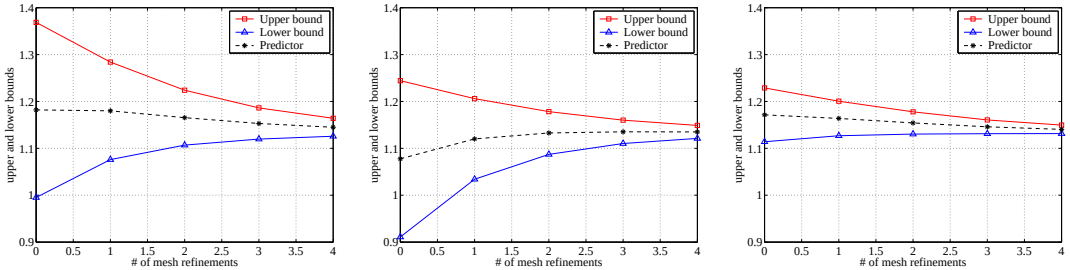

Figure 36. Slotted block problem 2 - Upper and lower bounds using uniform meshing

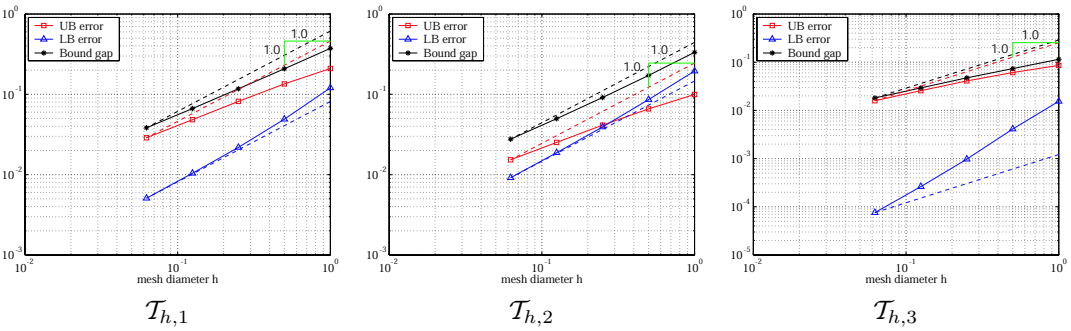

Figure 37. Slotted block problem 2 - Rates of convergence using uniform meshing

this result is only a consequence of the mesh. Indeed, for the lower bound case, the same formulation yields a linear rate of convergence when using $\mathcal{T}_{h,1}$ or $\mathcal{T}_{h,2}$, whereas $\mathcal{T}_{h,3}$ gives quadratic convergence. Since the formulation in [19] coincides with the lower bound approach presented in this article, the numerical results are the same when uniform meshing is used. However, when adaptive meshing is considered, considerable gains are obtained. For instance, with 2716 elements, the present approach yields a lower bound of 1.13153 (error of 0.0029%), whereas in [19], 5776 elements are needed to get a worse lower bound of 1.13150 (0.0052% error).

6.5. Computational Cost of Previous Examples

This section gives an indication of the computational cost required to solve both the lower and the upper bound problems for the finest uniform and adaptive meshes used in all previous examples. To solve the lower bound problems, the reduced formulations (54) (plane stress) and (55) (plane strain) have been chosen.However, the upper bound problems have been solved considering the original formulations (72) (plane stress) and (73) (plane strain) because, despite working with matrices of higher dimensions than strictly necessary, the solution process was very fast. To solve the bound problems, the free software SeDuMi 1.05R5 and SDPT3-3.02 was used in Matlab 6.5.1 on a Pentium®4 2.53GHz desktop PC. For both cases, the NT search direction was considered (see section 3).

Adaptive meshing with initial mesh $\mathcal{T}_{h,1}$						
Number of refin.	Number of elem.	Low. Bound λ_h^{*LB}	Upp. Bound λ_h^{*UB}	Bound Gap Δ_h	Low. Bound Error (%)	Upp. Bound Error (%)
0	32	0.9952	1.3688	0.37355	12.051	20.966
1	87	1.0708	1.2840	0.21321	5.370	13.472
2	291	1.1107	1.2240	0.11336	1.843	8.169
3	962	1.1213	1.1862	0.06484	0.907	4.829
4	2821	1.1265	1.1645	0.03802	0.447	2.911
5	6901	1.1290	1.1522	0.02320	0.226	1.824

Adaptive meshing with initial mesh $\mathcal{T}_{h,2}$						
Number of refin.	Number of elem.	Low. Bound λ_h^{*LB}	Upp. Bound λ_h^{*UB}	Bound Gap Δ_h	Low. Bound Error (%)	Upp. Bound Error (%)
0	32	0.9109	1.2444	0.33344	19.496	9.972
1	74	1.0514	1.2063	0.15494	7.084	6.605
2	262	1.1055	1.1784	0.07295	2.303	4.139
3	807	1.1195	1.1601	0.04063	1.066	2.522
4	2065	1.1256	1.1491	0.02346	0.527	1.550
5	4621	1.1286	1.1428	0.01421	0.261	0.993

Adaptive meshing with initial mesh $\mathcal{T}_{h,3}$						
Number of refin.	Number of elem.	Low. Bound λ_h^{*LB}	Upp. Bound λ_h^{*UB}	Bound Gap Δ_h	Low. Bound Error (%)	Upp. Bound Error (%)
0	16	1.11405	1.22888	0.114830	1.5478	8.6001
1	38	1.12425	1.20063	0.076386	0.6462	6.1044
2	114	1.13035	1.17830	0.047951	0.1068	4.1309
3	397	1.13126	1.16087	0.029602	0.0261	2.5899
4	1089	1.13147	1.15011	0.018635	0.0076	1.6392
5	2716	1.13153	1.14347	0.011947	0.0029	1.0528
6	5913	1.13154	1.13902	0.007480	0.0021	0.6589

Table IX. Results for the slotted block problem in plane strain using adaptive meshing

Table X shows, for each example, the number of elements in the meshes considered, the number of equations and variables (equivalent to the dimensions of the global matrices in problems (54), (55), (72) or (73)), as well as the time (in minutes and seconds) required to solve the optimization problems.

When solving the problems, SDPT3 was very robust and it always yielded optimal solutions. On the other hand, for some cases and always for the lower bound problem, SeDuMi ran into numerical difficulties that stopped the solution process. For the cases that SeDuMi could solve, it was systematically faster than SDPT3.

Notice that examples of considerable size can be solved. For instance, the finest uniform mesh in the second example (Block1) consists of 18432 elements resulting in matrices of dimensions $(258496, 276481)$ (lower bound) and $(110816, 147457)$ (upper bound), leading to the bound problems being solved in only 11 minutes 12 seconds and 1:22 seconds, respectively. For the adaptive case, matrices of dimensions $(78058, 83521)$ and $(33461, 44545)$ were addressed in 1:07 and 0:14 seconds.

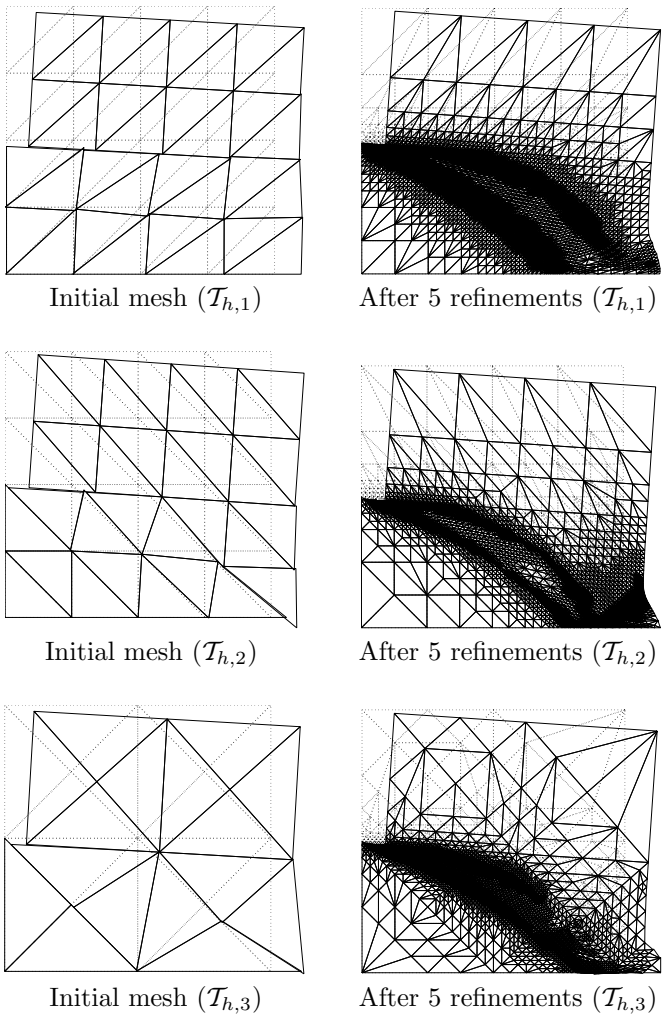

Figure 38. Slotted block problem 2 - Deformed geometry using adaptive meshing

ACKNOWLEDGEMENTS

The authors acknowledge the financial support of the Singapore-MIT Alliance and DARPA-AFOSR, through grant F49620-03-1-0439, which made possible the work presented in this article.

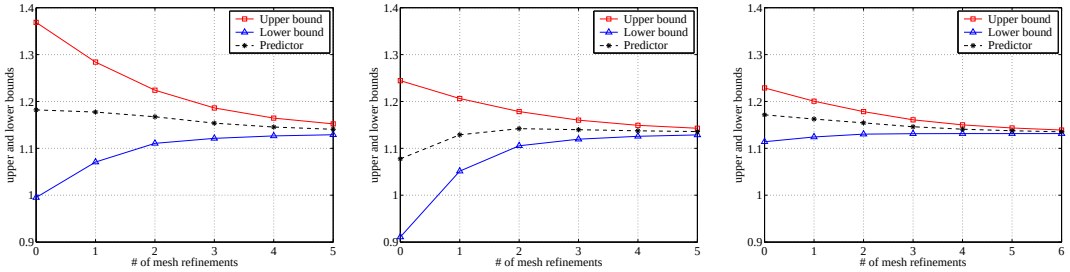

$\mathcal{T}_{h,1}$ $\mathcal{T}_{h,2}$ $\mathcal{T}_{h,3}$

Figure 39. Slotted block problem 2 - Bounds using adaptive meshing

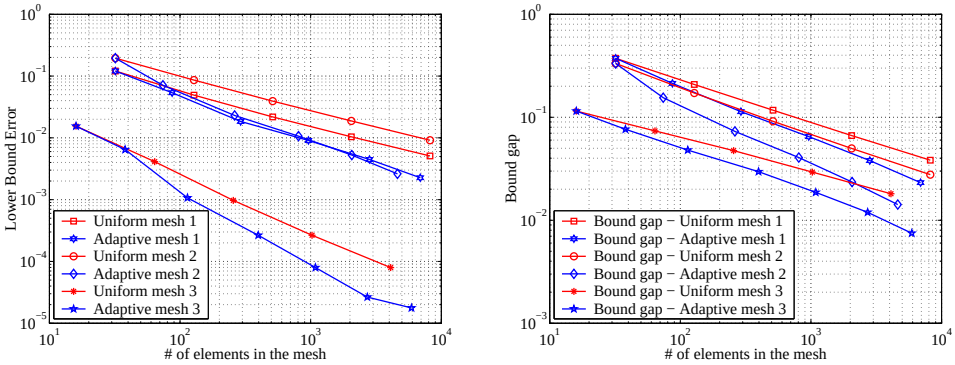

Lower bound error convergence Bound gap convergence

Figure 40. Slotted block problem 2 - Comparison of adaptive versus uniform meshing

APPENDIX A. PURELY STATIC AND KINEMATIC NATURE OF THE LOWER AND UPPER BOUND INTERPOLATION SPACES

A.1. Lower Bound Interpolation Spaces

A.1.1. Satisfaction of equilibrium over the continuum The objective is to show that when the weak form of equilibrium (3) is discretized using the interpolation spaces introduced in section 4.1.1, $X_h^{LB} \times Y_h^{LB}$, one obtains a set of discrete equations that, if satisfied, guarantee that equilibrium holds over the continuum (and not only discretely).

Since the stresses $\boldsymbol{\sigma}_h \in X_h^{LB}$ are piecewise discontinuous, we express the internal work rate as follows:

$$a(\boldsymbol{\sigma},\mathbf{u}) = -\sum_{e=1}^{E}\int_{\Omega^e}(\nabla\cdot\boldsymbol{\sigma}^e)\cdot\mathbf{u}^e\,dV + \sum_{\xi_e^{e'}\in\mathcal{E}^{\mathcal{O}}}\int_{\xi_e^{e'}}\mathbf{n}^{\xi_e^{e'}}\cdot(\boldsymbol{\sigma}^e-\boldsymbol{\sigma}^{e'})\cdot\mathbf{u}^{\xi_e^{e'}}\,dS + \sum_{\xi_e^N\in\mathcal{E}^{\mathcal{N}}}\int_{\xi_e^N}(\mathbf{n}^{\xi_e^N}\cdot\boldsymbol{\sigma}^e)\cdot\mathbf{u}^{\xi_e^N}\,dS, \tag{94}$$

where $\mathbf{n}^{\xi}$ is the outward normal unit vector on the edge ξ.

Example	Meshing	# elem.	Lower Bound Problem				Upper Bound Problem		
			# eq.	# var.	SeDuMi	SDPT3	# eq.	# var.	SeDuMi
Cantilever	unif.	8704	122176	130561	1:57	4:18	52384	69633	0:21
	adap.	5506	77252	82591	1:07	1:27	33120	44049	0:14
Block1	unif.	18432	258496	276481	-	11:12	110816	147457	1:22
	adap.	5568	78058	83521	1:07	1:27	33461	44545	0:14
Beam	unif.	6912	76432	82945	2:35	10:26	102864	123201	1:31
	adap.	4788	52858	57457	1:51	7:05	71538	85713	0:53
Block2-$\mathcal{T}_{h,1}$	unif.	8192	90432	98305	-	25:09	122176	146433	1:38
	adap.	6901	75979	82813	-	21:43	103243	123879	1:10
Block2-$\mathcal{T}_{h,2}$	unif.	8192	90432	98305	-	26:27	122176	146433	1:36
	adap.	4621	50929	55453	-	11:31	69073	82839	0:43
Block2-$\mathcal{T}_{h,3}$	unif.	4906	45216	49153	-	8:16	61088	73217	0:38
	adap.	5913	65079	70957	-	14:30	88559	106263	0:56

Note: For the cases not solved, SeDuMi ran into numerical problems.

Table X. Computational cost of solving the lower and upper bound problems for the finest uniform and adaptive meshes used in all previous examples

We rewrite expression (1) as a sum of elemental contributions:

$$F(\mathbf{u}) = \sum_{e=1}^{E} \int_{\Omega^e} \mathbf{f}^e \cdot \mathbf{u}^e \, dV + \sum_{\xi_e^N \in \mathcal{E}^{\mathcal{N}}} \int_{\xi_e^N} \mathbf{g}^{\xi_e^N} \cdot \mathbf{u}^{\xi_e^N} \, dS, \tag{95}$$

where $\mathbf{f}^e$ (assumed to be constant) and $\mathbf{g}^{\xi_e^N}$ (assumed to vary, at most, linearly) are the restrictions of $\mathbf{f}$ and $\mathbf{g}$ to Ω^e and $\partial\Omega^e \cap \Gamma^N$, respectively.

We introduce the interpolation spaces in expressions (94) and (95). For the integrals over the elements, $\nabla \cdot \boldsymbol{\sigma}_h{}^e$ and $\mathbf{f}^e$ are constant, as is the case for $\mathbf{u}_h^e$. Regarding the integrals over the edges, the terms $\mathbf{n}^{\xi_e^{e'}} \cdot (\boldsymbol{\sigma}_h^e - \boldsymbol{\sigma}_h^{e'})$ and $\mathbf{u}_h^{\xi_e^{e'}}$, as well as $\mathbf{n}^{\xi_e^{e'}} \cdot \boldsymbol{\sigma}_h^e$, $\mathbf{g}^{\xi_e^N}$ and $\mathbf{u}_h^{\xi_e^N}$ are all, at most, linear. Consequently, the equation $a(\boldsymbol{\sigma}_h, \mathbf{u}_h) = \lambda F(\mathbf{u}_h)$, $\forall \mathbf{u}_h \in Y_h^{LB}$, is equivalent to the following system of equations:

$$\nabla \cdot \boldsymbol{\sigma}_h^e + \lambda \mathbf{f}^e = \mathbf{0}, \qquad \text{in } \Omega^e, \forall e \in \mathcal{T}_h \tag{96}$$

$$(\boldsymbol{\sigma}_h^e - \boldsymbol{\sigma}_h^{e'}) \cdot \mathbf{n}^{\xi_e^{e'}} = \mathbf{0}, \qquad \forall \xi_e^{e'} \in \mathcal{E}^{\mathcal{O}} \tag{97}$$

$$\boldsymbol{\sigma}_h^e \cdot \mathbf{n}^{\xi_e^N} = \lambda \mathbf{g}^{\xi_e^N}, \quad \forall \xi_e^N \in \mathcal{E}^{\mathcal{N}} \tag{98}$$

where (96) imposes internal equilibrium on each element; (97) forces continuity of tractions in the internal edges; and (98) makes the tractions on the Neuman boundary edges coincide with the external surface loads, $\lambda \mathbf{g}$.

We see that the interpolation space Y_h^{LB} is rich enough, when compared to X_h^{LB}, to make implication (18) hold. However, it is still necessary to show that the equations (96-98) can be satisfied exactly with the linear interpolation space X_h^{LB}.

Let us start with (96). Since the stresses vary linearly, the divergence of the stress tensor is constant in each element. Given that the elemental body force, $\mathbf{f}^e$, is constant, the equation can be satisfied exactly. Let us now move to the edge equations (97) and (98). In both cases, for each edge, they impose two scalar equations (in x_1 and x_2) that must hold for all the points lying on the edge. However, given that $\boldsymbol{\sigma}_h^e$ varies linearly in the element, it is enough to make them hold only in two points of the edge, for instance, at the nodes. Therefore, if each scalar equation is imposed twice, one per node of the edge, one ends up with four nodal scalar equations which, if satisfied, guarantee that (97) and (98) hold over the whole edge.

Thus, by imposing $2 \times E$ discrete equations for (96) and $4 \times (|\mathcal{E}^{\mathcal{O}}| + |\mathcal{E}^{\mathcal{N}}|)$ nodal equations for (97) and (98) -where the symbol $|\cdot|$ stands for the cardinality of a set- the system of equations (96-98) is satisfied exactly.

The last detail to address concerns the feasibility of the discrete equilibrium equations. The idea is to analyze if the $9 \times E$ nodal stresses (unknowns) introduced by the interpolation space X_h^{LB} bring enough degrees of freedom to satisfy the total number of equations: $2 \times E + 4 \times (|\mathcal{E}^{\mathcal{O}}| + |\mathcal{E}^{\mathcal{N}}|)$. This feasibility study is complex since it depends on the degree of linear independence of the equations as well as on the particular geometry of the mesh. However, some indications can be made. For instance, assuming linearly independence of the equations, a necessary and sufficient condition for feasibility is that the number of unknowns be greater or equal than the total number of equations. This translates into the following condition on the mesh (see [15] for details):

$$E \geq 2 \times (|\mathcal{E}^{\mathcal{N}}| - |\mathcal{E}^{\mathcal{D}}|). \tag{99}$$

Notice that the above inequality might be violated for trivial meshes composed of very few elements. However, for larger meshes, the inequality always holds, since the number of elements E grows with $1/h^2$, whereas the number of boundary edges grows like $1/h$. Therefore, it seems reasonable to conclude that, for non trivial examples, the feasibility of the discrete equilibrium equations is guaranteed. This is supported by experience, since all the examples tested were always feasible.

There is a case, however, that may cause infeasibility in the system of equations, even if (99) is satisfied. This occurs when an element is in a corner of the domain and two of its edges belong to $\mathcal{E}^{\mathcal{N}}$. Then, for the corner node, 4 scalar equations derived from (97) are imposed. Since the node only has 3 independent unknowns (the 3 stresses), the system may become infeasible. However, this problem can be solved easily by identifying the problematic elements in the mesh and, then, postprocessing the mesh so that there is always an internal edge incident to every corner of the domain.

A.1.2.Satisfaction of the Yield Condition over the Continuum We consider here the plane stress case for simplicity. The plane strain analysis is analogous. Recall that, to obtain a lower bound, the yield condition must hold at every point of the domain, that is, $\boldsymbol{\sigma}_h(\mathbf{x}) \in B_{1,h},\ \forall \mathbf{x} \in \Omega$. However, when computing lower bounds in practice, this pointwise property is only explicitly imposed over the nodes of each triangle, by means of $3 \times E$ inequalities of the following form

$$\boldsymbol{\sigma}^{a,e} \in B_{1,h} \Rightarrow (\sigma_1^{a,e} - \sigma_2^{a,e})^2 + (\sigma_1^{a,e})^2 + (\sigma_2^{a,e})^2 + 6(\sigma_3^{a,e})^2 \leq 2\sigma_y^2;\ \forall e \in \mathcal{T}_h,\ a = 1:3. \tag{100}$$

For a given element Ω^e we want to proves that:

$$(\sigma_1(\mathbf{x}) - \sigma_2(\mathbf{x}))^2 + \sigma_1(\mathbf{x})^2 + \sigma_2(\mathbf{x})^2 + 6\sigma_3(\mathbf{x})^2 \leq 2\sigma_y^2, \quad \forall \mathbf{x} \in \Omega^e. \tag{101}$$

Inserting the linear interpolation (28) into the left-hand side of (101), gives:

$$LHS = \left(\sum_{a=1}^{3}(\sigma_1^a - \sigma_2^a)N_a(\mathbf{x})\right)^2 + \left(\sum_{a=1}^{3}\sigma_1^a N_a(\mathbf{x})\right)^2 + \left(\sum_{a=1}^{3}\sigma_2^a N_a(\mathbf{x})\right)^2 + 6\left(\sum_{a=1}^{3}\sigma_3^a N_a(\mathbf{x})\right)^2 \tag{102}$$

After expanding, doing the necessary algebra and regrouping terms, one has:

$$LHS = \alpha N_1(\mathbf{x})^2 + \beta N_2(\mathbf{x})^2 + \gamma N_3(\mathbf{x})^2 + \delta\ 2N_1(\mathbf{x})N_2(\mathbf{x}) + \epsilon\ 2N_1(\mathbf{x})N_3(\mathbf{x}) + \zeta\ 2N_2(\mathbf{x})N_3(\mathbf{x}), \tag{103}$$

where

$$\begin{aligned}
\alpha &= (\sigma_1^1 - \sigma_2^1)^2 + (\sigma_1^1)^2 + (\sigma_2^1)^2 + 6(\sigma_3^1)^2 && (104)\\
\beta &= (\sigma_1^2 - \sigma_2^2)^2 + (\sigma_1^2)^2 + (\sigma_2^2)^2 + 6(\sigma_3^2)^2 && (105)\\
\gamma &= (\sigma_1^3 - \sigma_2^3)^2 + (\sigma_1^3)^2 + (\sigma_2^3)^2 + 6(\sigma_3^3)^2 && (106)\\
\delta &= (\sigma_1^1 - \sigma_2^1)(\sigma_1^2 - \sigma_2^2) + \sigma_1^1\sigma_1^2 + \sigma_2^1\sigma_2^2 + 6\sigma_3^1\sigma_3^2 && (107)\\
\epsilon &= (\sigma_1^1 - \sigma_2^1)(\sigma_1^3 - \sigma_2^3) + \sigma_1^1\sigma_1^3 + \sigma_2^1\sigma_2^3 + 6\sigma_3^1\sigma_3^3 && (108)\\
\zeta &= (\sigma_1^2 - \sigma_2^2)(\sigma_1^3 - \sigma_2^3) + \sigma_1^2\sigma_1^3 + \sigma_2^2\sigma_2^3 + 6\sigma_3^2\sigma_3^3 && (109)
\end{aligned}$$

From (100), it is apparent that $\alpha \leq 2\sigma_y^2$, $\beta \leq 2\sigma_y^2$ and $\gamma \leq 2\sigma_y^2$. Combining equation (100) for $a = 1, 2$ gives:

$$\left[(\sigma_1^1 - \sigma_2^1)^2 + (\sigma_1^2 - \sigma_2^2)^2\right] + \left[(\sigma_1^1)^2 + (\sigma_1^2)^2\right] + \left[(\sigma_2^2)^2 + (\sigma_2^1)^2\right] + 6\left[(\sigma_3^1)^2 + (\sigma_3^2)^2\right] \leq 4\sigma_y^2. \quad (110)$$

Using the following simple inequality $2ab \leq a^2 + b^2$ in (110), one obtains:

$$\left[2(\sigma_1^1 - \sigma_2^1)(\sigma_1^2 - \sigma_2^2)\right] + \left[2\sigma_1^1\sigma_1^2\right] + \left[2\sigma_2^2\sigma_2^1\right] + 6\left[2\sigma_3^1\sigma_3^2\right] \leq 4\sigma_y^2, \quad (111)$$

which shows that $\delta \leq 2\sigma_y^2$. Using an analogous argument we can prove that $\epsilon \leq 2\sigma_y^2$ and $\zeta \leq 2\sigma_y^2$. Since all the coefficients in (103) are bounded by $2\sigma_y^2$, we have:

$$\begin{aligned} LHS &\leq 2\sigma_y^2\left[N_1(\mathbf{x})^2 + N_2(\mathbf{x})^2 + N_3(\mathbf{x})^2 + 2N_1(\mathbf{x})N_2(\mathbf{x}) + 2N_1(\mathbf{x})N_3(\mathbf{x}) + 2N_2(\mathbf{x})N_3(\mathbf{x})\right] \\ &= 2\sigma_y^2\left[N_1(\mathbf{x}) + N_2(\mathbf{x}) + N_3(\mathbf{x})\right]^2 \equiv 2\sigma_y^2 \end{aligned} \quad (112)$$

where the identity: $N_1(\mathbf{x}) + N_2(\mathbf{x}) + N_3(\mathbf{x}) = 1$ has been used.

A.2. Upper Bound Interpolation Spaces

For the **plane stress** case, the proof is straightforward and is based on (21). Since $Y_{h,1}^{UB}$ is a linear function space, the strain rate tensor $\varepsilon_{ij}(\mathbf{u})$ in (2) is constant on each element. Therefore, the $\max_{\boldsymbol{\sigma}\in B} a(\boldsymbol{\sigma}; \mathbf{u}_h)$ is going to be attained for a stress field $\boldsymbol{\sigma}^* \in B$ that is elementally piecewise constant, that is, $\boldsymbol{\sigma}^* \in X_h$. Consequently, $\boldsymbol{\sigma}^* \in B \cap X_h = B_h$, that is, $\boldsymbol{\sigma}^* = \boldsymbol{\sigma}_h$, which proves the statement.

For **plane strain**, we need to incorporate the junps into the expression for the internal work rate:

$$a(\boldsymbol{\sigma}, \mathbf{t}, \mathbf{u}) = \int_\Omega \boldsymbol{\sigma} : \boldsymbol{\varepsilon}(\mathbf{u})\, dV + \sum_{\xi_e^{e'} \in \mathcal{E}^{\mathcal{O}}} \int_{\xi_e^{e'}} \mathbf{t}^{\xi_e^{e'}} \cdot (\mathbf{u}^{e'} - \mathbf{u}^e)\, dS \quad (113)$$

$$= \int_\Omega \sum_{i,j=1}^{2} \sigma_{ij} \frac{\partial u_i}{\partial x_j}\, dV + \sum_{\xi_e^{e'} \in \mathcal{E}^{\mathcal{O}}} \int_{\xi_e^{e'}} \sum_{i'=1}^{2} t_{i'}^{\xi_e^{e'}} (u_{i'}^{e'} - u_{i'}^e)\, dS \quad (114)$$

The tractions, $\mathbf{t}_h$, are not constrained to belong to $B_{h,2}$, but to a larger admissible set, $\tilde{B}_{h,2}$. Now, to show the purely kinematic nature of $X_{h,2}^{UB} \times Y_{h,2}^{UB}$, we note that:

$$\max_{\boldsymbol{\sigma}\in B_2; \mathbf{t}\in B_2} a(\boldsymbol{\sigma},\ \mathbf{t}, \mathbf{u}_h) = \max_{\boldsymbol{\sigma}\in B_2} \int_\Omega \boldsymbol{\sigma} : \boldsymbol{\varepsilon}(\mathbf{u}_h)\, dV + \max_{\mathbf{t}\in B_2} \sum_{\xi_e^{e'} \in \mathcal{E}^{\mathcal{O}}} \int_{\xi_e^{e'}} \mathbf{t}^{\xi_e^{e'}} \cdot (\mathbf{u}_h^{e'} - \mathbf{u}_h^e)\, dS \quad (115)$$

By the same argument given in the plane stress case, the following holds for the first term in (115),

$$\max_{\boldsymbol{\sigma}\in B_2} \int_\Omega \boldsymbol{\sigma} : \boldsymbol{\varepsilon}(\mathbf{u}_h)\, dV = \max_{\boldsymbol{\sigma}_h \in B_{h,2}} \int_\Omega \boldsymbol{\sigma}_h : \boldsymbol{\varepsilon}(\mathbf{u}_h)\, dV; \quad \forall \mathbf{u}_h \in Y_{h,2}^{UB} \quad (116)$$

Regarding the second term, since $Y_{h,2}^{UB}$ is a linear interpolation of the displacements and $B_{h,2} \subset \tilde{B}_{h,2}$, then

$$\max_{\mathbf{t}\in B_2} \sum_{\xi_e^{e'} \in \mathcal{E}^{\mathcal{O}}} \int_{\xi_e^{e'}} \mathbf{t}^{\xi_e^{e'}} \cdot (\mathbf{u}_h^{e'} - \mathbf{u}_h^e)\, dS \leq \max_{\mathbf{t}_h \in \tilde{B}_{h,2}} \sum_{\xi_e^{e'} \in \mathcal{E}^{\mathcal{O}}} \int_{\xi_e^{e'}} \mathbf{t}_h^{\xi_e^{e'}} \cdot (\mathbf{u}_h^{e'} - \mathbf{u}_h^e)\, dS; \quad \forall \mathbf{u}_h \in Y_{h,2}^{UB}. \quad (117)$$

Finally, considering (116) and (117), it is apparent that:

$$\max_{\boldsymbol{\sigma}\in B_2;\ \mathbf{t}\in B_2} a(\boldsymbol{\sigma}, \mathbf{t}, \mathbf{u}_h) \leq \max_{\boldsymbol{\sigma}_h \in B_{h,2};\ \mathbf{t}_h \in \tilde{B}_{h,2}} a(\boldsymbol{\sigma}_h, \mathbf{t}_h, \mathbf{u}_h), \quad \forall \mathbf{u}_h \in Y_{h,2}^{UB} \quad (118)$$

Therefore, condition (22) holds, which shows that $X_{h,2}^{UB} \times Y_{h,2}^{UB}$ are purely kinematic spaces.

APPENDIX B. REDUCTION OF THE DIMENSIONALITY OF THE LOWER BOUND PROBLEM

The goal is to reduce the dimensionality of the lower bound problem (52), by directly formulating the equilibrium equations in terms of the additional variables $\underline{x}^{soc}$, instead of using the nodal stresses, $\underline{\sigma}_h$. To this end, the relationship between the two set of variables must be established.

For plane stress, using (48) for all nodes a and elements $e \in \mathcal{T}_h$, this can be achieved as follows:

$$\left\{\begin{array}{lcl} \sigma_1^{a,e} &=& x_2^{a,e} \\ \sigma_2^{a,e} &=& x_3^{a,e} \\ \sigma_3^{a,e} &=& \frac{1}{\sqrt{6}} x_4^{a,e} \end{array}\right. \longrightarrow \left(\begin{array}{c} \sigma_1^{a,e} \\ \sigma_2^{a,e} \\ \sigma_2^{a,e} \end{array}\right) = \left(\begin{array}{ccccc} 0 & 1 & 0 & 0 & 0 \\ 0 & 0 & 1 & 0 & 0 \\ 0 & 0 & 0 & \frac{1}{\sqrt{6}} & 0 \end{array}\right) \left(\begin{array}{c} x_1^{a,e} \\ x_2^{a,e} \\ x_3^{a,e} \\ x_4^{a,e} \\ x_5^{a,e} \end{array}\right) \longrightarrow \underline{\sigma}_h^{a,e} = \underline{\underline{Q}}^{ae} \underline{x}_1^{a,e} \tag{119}$$

For plane strain the additional variables introduced in (48) are not enough to express the nodal stresses $\underline{\sigma}_h^{a,e}$ in terms of $\underline{x}^{a,e}$. For this reason, it is necessary to include one more additional variable and extend (48) for plane strain as follows:

$$\left\{\begin{array}{rcl} x_1^{a,e} &=& \frac{2}{\sqrt{3}}\sigma_y \\ -2\sigma_3^{a,e} + x_2^{a,e} &=& 0 \\ -\sigma_1^{a,e} + \sigma_2^{a,e} + x_3^{a,e} &=& 0 \\ -\sigma_1^{a,e} + x_4^{a,e} &=& 0 \end{array}\right. \tag{120}$$

Considering (120), the equivalent expression to (119) is:

$$\left\{\begin{array}{lcl} \sigma_1^{a,e} &=& x_4^{a,e} \\ \sigma_2^{a,e} &=& x_4^{a,e} - x_3^{a,e} \\ \sigma_3^{a,e} &=& \frac{1}{2} x_2^{a,e} \end{array}\right. \rightarrow \left(\begin{array}{c} \sigma_1^{a,e} \\ \sigma_2^{a,e} \\ \sigma_2^{a,e} \end{array}\right) = \left(\begin{array}{c} 1 \\ 1 \\ 0 \end{array}\right) x_4^{a,e} + \left(\begin{array}{ccc} 0 & 0 & 0 \\ 0 & 0 & -1 \\ 0 & \frac{1}{2} & 0 \end{array}\right) \left(\begin{array}{c} x_1^{a,e} \\ x_2^{a,e} \\ x_3^{a,e} \end{array}\right) \rightarrow \underline{\sigma}_h^{a,e} = \underline{P}^{ae} x_4^{a,e} + \underline{\underline{Q}}^{ae}_2 \underline{x}_2^{a,e} \tag{121}$$

Now, using the matrix notation (119) and (121), the equilibrium constraints can be written as:

$$\text{plane stress} \quad \left\{\begin{array}{lcl} \underline{\underline{A}}^{eq1} \underline{\underline{Q}}_1 \underline{x}_1^{soc} + \underline{F}_h^{eq1} \lambda &=& \underline{0} \\ \underline{\underline{A}}^{eq2} \underline{\underline{Q}}_1 \underline{x}_1^{soc} + \underline{F}_h^{eq2} \lambda &=& \underline{0}, \end{array}\right. \text{with } \underline{\sigma}_h = \underline{\underline{Q}}_1 \underline{x}_1^{soc} \tag{122}$$

$$\text{plane strain} \quad \left\{\begin{array}{lcl} \underline{\underline{A}}^{eq1} \underline{\underline{P}} \underline{x}_4 + \underline{\underline{A}}^{eq1} \underline{\underline{Q}}_2 \underline{x}_2^{soc} + \underline{F}_h^{eq1} \lambda &=& \underline{0} \\ \underline{\underline{A}}^{eq2} \underline{\underline{P}} \underline{x}_4 + \underline{\underline{A}}^{eq2} \underline{\underline{Q}}_2 \underline{x}_2^{soc} + \underline{F}_h^{eq2} \lambda &=& \underline{0}, \end{array}\right. \text{with } \underline{\sigma}_h = \underline{\underline{P}} \underline{x}_4 + \underline{\underline{Q}}_2 \underline{x}_2^{soc} \tag{123}$$

where, for $\delta = 1:2$,

$$\underline{\underline{Q}}_\delta = \left(\begin{array}{ccccc} \underline{\underline{Q}}_\delta^{ae} & \underline{\underline{0}} & \cdots & \cdots & \underline{\underline{0}} \\ \underline{\underline{0}} & \underline{\underline{Q}}_\delta^{ae} & \underline{\underline{0}} & \cdots & \underline{\underline{0}} \\ \vdots & & \ddots & & \vdots \\ \vdots & & & \ddots & \vdots \\ \underline{\underline{0}} & \cdots & \cdots & \cdots & \underline{\underline{Q}}_\delta^{ae} \end{array}\right), \quad \underline{x}_\delta^{soc} = \left(\begin{array}{c} \underline{x}_\delta^{1,1} \\ \vdots \\ \underline{x}_\delta^{a,e} \\ \vdots \\ \underline{x}_\delta^{3,E} \end{array}\right), \quad \underline{\underline{P}} = \left(\begin{array}{ccccc} \underline{P}^{ae} & \underline{\underline{0}} & \cdots & \cdots & \underline{\underline{0}} \\ \underline{\underline{0}} & \underline{P}^{ae} & \underline{\underline{0}} & \cdots & \underline{\underline{0}} \\ \vdots & & \ddots & & \vdots \\ \vdots & & & \ddots & \vdots \\ \underline{\underline{0}} & \cdots & \cdots & \cdots & \underline{P}^{ae} \end{array}\right), \quad \underline{x}_4 = \left(\begin{array}{c} x_4^{1,1} \\ \vdots \\ x_4^{a,e} \\ \vdots \\ x_4^{3,E} \end{array}\right) \tag{124}$$

To impose the membership constraints in the three nodes of all the elements, it is still necessary to add the two remaining nodal equations in (48), for plane stress, and the first equation in (120), for

plane strain. This can be done as follows:

$$\text{plane stress} \quad \left\{ \begin{array}{rcl} x_1^{a,e} & = & \sqrt{2}\sigma_y \\ x_5^{a,e} & = & x_2^{ae} - x_3^{ae} \end{array} \right. \quad \Longrightarrow \overbrace{\left(\begin{array}{ccccc} 1 & 0 & 0 & 0 & 0 \\ 0 & 1 & -1 & 0 & -1 \end{array} \right)}^{\underline{\underline{R}}_1^{ae}} \left(\begin{array}{c} x_1^{a,e} \\ x_2^{a,e} \\ x_3^{a,e} \\ x_4^{a,e} \\ x_5^{a,e} \end{array} \right) = \overbrace{\left(\begin{array}{c} \sqrt{2}\sigma_y \\ 0 \end{array} \right)}^{\underline{\tilde{b}}_1^{ae}} \tag{125}$$

$$\text{plane strain} \qquad x_1^{a,e} = \tfrac{2}{\sqrt{3}}\sigma_y \qquad \Longrightarrow \overbrace{\left(\begin{array}{ccc} 1 & 0 & 0 \end{array} \right)}^{\underline{\underline{R}}_2^{ae}} \left(\begin{array}{c} x_1^{a,e} \\ x_2^{a,e} \\ x_3^{a,e} \end{array} \right) = \overbrace{\frac{2}{\sqrt{3}}\sigma_y}^{\tilde{b}_2^{ae}}, \tag{126}$$

which results, for $\delta = 1:2$, in the following global matrix equation:

$$\underline{\underline{R}}_\delta \underline{x}_\delta^{soc} = \underline{\tilde{b}}_\delta^{soc}, \quad \text{where} \quad \underline{\underline{R}}_\delta = \left(\begin{array}{ccccc} \underline{\underline{R}}_\delta^{ae} & \underline{\underline{0}} & \cdots & \cdots & \underline{\underline{0}} \\ \underline{\underline{0}} & \underline{\underline{R}}_\delta^{ae} & \underline{\underline{0}} & \cdots & \underline{\underline{0}} \\ \vdots & & \ddots & & \vdots \\ \vdots & & & \ddots & \vdots \\ \underline{\underline{0}} & \cdots & \cdots & \cdots & \underline{\underline{R}}_\delta^{ae} \end{array} \right), \quad \underline{\tilde{b}}_\delta^{soc} = \left(\begin{array}{c} \underline{\tilde{b}}_\delta^{ae} \\ \underline{\tilde{b}}_\delta^{ae} \\ \vdots \\ \vdots \\ \underline{\tilde{b}}_\delta^{ae} \end{array} \right). \tag{127}$$

APPENDIX C. DISCRETIZATION OF THE EQUILIBRIUM EQUATIONS FOR THE UPPER BOUND PROBLEM

C.1. Equilibrium Constraint in Plane Stress

To discretize the equilibrium equation $a(\boldsymbol{\sigma}, \mathbf{u}) = \lambda F(\mathbf{u}), \forall \mathbf{u} \in Y$, where $a(\boldsymbol{\sigma}, \mathbf{u})$ is given in (2), one replaces the stresses, $\boldsymbol{\sigma}$, and velocities, $\mathbf{u}$, by their global interpolations (56) and (58) , respectively:

$$a(\boldsymbol{\sigma}, \mathbf{u}) = \lambda F(\mathbf{u}) \implies \sum_{i,j=1}^{2} \int_\Omega \sigma_{ij} \frac{\partial u_i}{\partial x_j} \, dV = \lambda \sum_{i=1}^{2} \left(\int_\Omega f_i u_i \, dV + \int_{\Gamma^N} g_i u_i \, dS \right), \tag{128}$$

$$\sum_{e=1}^{E} \sum_{A=1}^{N} \sum_{i,j=1}^{2} \int_\Omega \sigma_{ij}^e \psi_e(\mathbf{x}) u_i^A \frac{\partial \phi_A(\mathbf{x})}{\partial x_j} \, dV = \lambda \sum_{A=1}^{N} \sum_{i=1}^{2} u_i^A \left(\int_\Omega f_i \phi_A(\mathbf{x}) \, dV + \int_{\Gamma^N} g_i \phi_A(s) \, dS \right), \tag{129}$$

where $\phi_A(s)$ is the restriction of $\phi_A(\mathbf{x})$ to the boundary Γ^N. Taking into account that the stress shape function $\psi_e(\mathbf{x})$ is equal to 1 inside the element Ω^e and vanishes outside, (129) can be simplified as shown next:

$$\sum_{e=1}^{E} \sum_{A=1}^{N} \sum_{i,j=1}^{2} \int_{\Omega^e} \sigma_{ij}^e u_i^A \frac{\partial N_A^e(\mathbf{x})}{\partial x_j} \, dV = \lambda \sum_{A=1}^{N} \sum_{i=1}^{2} u_i^A \sum_{e=1}^{E} \left(\int_{\Omega^e} f_i N_A^e(\mathbf{x}) \, dV + \int_{\xi_e^N} g_i N_A^e(s) \, dS \right) \tag{130}$$

Notice that $\phi_A(\mathbf{x})$ has been substituted by $N_A^e(\mathbf{x})$ because the integrals are now restricted to the elements. To avoid a cumbersome notation, the global nodal index A has been maintained in the local shape functions. In matrix form, and using the notation $N_{a,i}^e = \frac{\partial N_a^e(\mathbf{x})}{\partial x_i}$ where $i = 1:2$, (130) reads as follows:

$$\sum_{e=1}^{E} \sum_{A=1}^{N} \left(u_1^A, u_2^A \right) \left(\begin{array}{cc} \int_{\Omega^e} N_{A,1}^e \, dV & 0 \\ 0 & \int_{\Omega^e} N_{A,2}^e \, dV \end{array} \right. \left. \begin{array}{c} \int_{\Omega^e} N_{A,2}^e \, dV \\ \int_{\Omega^e} N_{A,1}^e \, dV \end{array} \right) \left(\begin{array}{c} \sigma_{11}^e \equiv \sigma_1^e \\ \sigma_{22}^e \equiv \sigma_2^e \\ \sigma_{12}^e \equiv \sigma_3^e \end{array} \right) = \tag{131}$$

$$= \lambda \sum_{A=1}^{N} \left(u_1^A, u_2^A \right) \left(\begin{array}{c} \sum_{e=1}^{E} \left(\int_{\Omega^e} f_1 N_A^e(\mathbf{x}) \, dV + \int_{\xi_e^N} g_1 N_A^e(\mathbf{x}) \, dS \right) \\ \sum_{e=1}^{E} \left(\int_{\Omega^e} f_2 N_A^e(\mathbf{x}) \, dV + \int_{\xi_e^N} g_2 N_A^e(\mathbf{x}) \, dS \right) \end{array} \right), \tag{132}$$

or, equivalently,

$$\sum_{e=1}^{E}\sum_{A=1}^{N}(\underline{u}_h^A)^T\underline{\underline{B}}_A^e\tilde{\underline{\sigma}}_h^e=\lambda\sum_{A=1}^{N}(\underline{u}_h^A)^T\underline{F}_h^A \tag{133}$$

Finally, the above expression can be expressed in a more compact form by using global matrices and vectors:

$$(\underline{u}_h)^T\underline{\underline{A}}^{eq}\tilde{\underline{\sigma}}_h=\lambda(\underline{u}_h)^T\underline{F}_h^{eq}, \tag{134}$$

where

$$\underline{\underline{A}}^{eq}=\begin{pmatrix}\underline{\underline{B}}_1^1 & \underline{\underline{B}}_1^2 & \cdots & \cdots & \underline{\underline{B}}_1^E\\ \underline{\underline{B}}_2^1 & \underline{\underline{B}}_2^2 & \cdots & \cdots & \underline{\underline{B}}_2^E\\ \vdots & & \ddots & & \vdots\\ \vdots & & & \ddots & \vdots\\ \underline{\underline{B}}_A^1 & \cdots & \cdots & \cdots & \underline{\underline{B}}_A^E\end{pmatrix};\quad \underline{u}_h=\begin{pmatrix}\underline{u}_h^1\\ \vdots\\ \underline{u}_h^A\\ \vdots\\ \underline{u}_h^N\end{pmatrix};\quad \tilde{\underline{\sigma}}_h=\begin{pmatrix}\tilde{\underline{\sigma}}_h^1\\ \vdots\\ \tilde{\underline{\sigma}}_h^e\\ \vdots\\ \tilde{\underline{\sigma}}_h^E\end{pmatrix};\quad \underline{F}_h^{eq}=\begin{pmatrix}\underline{F}_h^1\\ \vdots\\ \underline{F}_h^A\\ \vdots\\ \underline{F}_h^N\end{pmatrix}. \tag{135}$$

Clearly, the dimensions of the matrix $\underline{\underline{A}}^{eq}$ are $(2\times A, 3\times E)$. Since equation (134) must be satisfied $\forall\mathbf{u}_h\in Y_h^{UB}$, one can eliminate the nodal displacement vector $\underline{u}_h$, thereby obtaining the following global equilibrium equation:

$$\underline{\underline{A}}^{eq}\tilde{\underline{\sigma}}_h=\lambda\underline{F}_h^{eq}. \tag{136}$$

C.2. Equilibrium Constraint in Plane Strain

In plane strain, the weak form of equilibrium is given by:

$$\begin{aligned} a(\boldsymbol{\sigma},\mathbf{t},\mathbf{u}) &= \lambda F(\mathbf{u}),\ \forall\mathbf{u}\in Y \\ \underbrace{\sum_{i,j=1}^{2}\int_\Omega\sigma_{ij}\frac{\partial u_i}{\partial x_j}\,dV}_{1}+\underbrace{\sum_{\xi_e^{e'}\in\mathcal{E}^{\mathcal{O}}}\sum_{i'=1}^{2}\int_{\xi_e^{e'}}t_{i'}^{\xi_e^{e'}}\,(u_{i'}^{e'}-u_{i'}^{e})\,dS}_{2} &= \underbrace{\lambda\sum_{i=1}^{2}\left(\int_\Omega f_iu_i\,dV+\int_{\Gamma^N}g_iu_i\,dS\right)}_{3},\ \forall\mathbf{u}\in Y \end{aligned} \tag{137}$$

To discretize (137), one inserts the interpolations (59) (for $\mathbf{u}_h$), (60) (for $\boldsymbol{\sigma}_h$) and (61) (for $\mathbf{t}_h$). Notice that the terms (1) and (3) in the above equation are the same as in the plane stress case.

Using (59) and (60), term (1) results in the following expression:

$$\sum_{e=1}^{E}\sum_{a=1}^{3}(u_1^{a,e},u_2^{a,e})\begin{pmatrix}\int_{\Omega^e}N_{a,1}^e\,dV & 0 & \int_{\Omega^e}N_{a,2}^e\,dV\\ 0 & \int_{\Omega^e}N_{a,2}^e\,dV & \int_{\Omega^e}N_{a,1}^e\,dV\end{pmatrix}\begin{pmatrix}\sigma_1^e\\ \sigma_2^e\\ \sigma_3^e\end{pmatrix}=$$

$$=\sum_{e=1}^{E}\left(\sum_{a=1}^{3}(\underline{u}_h^{a,e})^T\underline{\underline{B}}_a^e\right)\tilde{\underline{\sigma}}_h^e=\sum_{e=1}^{E}(\underline{u}^{1,e},\underline{u}^{2,e},\underline{u}^{3,e})\begin{pmatrix}\underline{\underline{B}}_1^e\\ \underline{\underline{B}}_2^e\\ \underline{\underline{B}}_3^e\end{pmatrix}\tilde{\underline{\sigma}}_h^e=\sum_{e=1}^{E}\underline{u}^e\underline{\underline{B}}^e\tilde{\underline{\sigma}}_h^e=(\tilde{\underline{u}}_h)^T\tilde{\underline{\underline{A}}}^{eq1}\tilde{\underline{\sigma}}_h, \tag{138}$$

where $\tilde{\underline{u}}_h$ is a vector collecting the $6\times E$ nodal displacements, $\tilde{\underline{\underline{A}}}^{eq1}$ is a matrix of dimensions $(6\times E, 3\times E)$ and $\tilde{\underline{\sigma}}_h$ is a $3\times E$ vector of elemental stresses (the same as in (135)).

Regarding term (3), using (59) one obtains:

$$\sum_{e=1}^{E}\sum_{a=1}^{3}(u_1^{a,e},u_2^{a,e})\begin{pmatrix}\int_{\Omega^e}f_1^eN_A^e(\mathbf{x})\,dV+\int_{\xi_e^N}g_1^{\xi_e^N}N_A^e(\mathbf{x})\,dS\\ \int_{\Omega^e}f_2^eN_A^e(\mathbf{x})\,dV+\int_{\xi_e^N}g_2^{\xi_e^N}N_A^e(\mathbf{x})\,dS\end{pmatrix}=\sum_{e=1}^{E}\left(\sum_{a=1}^{3}(\underline{u}_h^{a,e})^T\underline{F}_{ha}^{\ e}\right)=$$

$$= \sum_{e=1}^{E} \left(\underline{u}^{1,e}, \underline{u}^{2,e}, \underline{u}^{3,e}\right) \begin{pmatrix} \underline{F}_{h\,1}^{\ e} \\ \underline{F}_{h\,2}^{\ e} \\ \underline{F}_{h\,3}^{\ e} \end{pmatrix} = \sum_{e=1}^{E} \underline{u}^{e}\, \underline{F}_{h}^{\ e} = (\underline{\tilde{u}}_h)^T\, \underline{\tilde{F}}_{h}^{\ eq}, \tag{139}$$

where $\underline{\tilde{F}}_{h}^{\ eq}$ is a vector of $6 \times E$ discontinuous nodal forces.

Let $\mathbf{n}^{\xi_e^{e'}}$ and $\boldsymbol{\tau}^{\xi_e^{e'}}$ be orthonormal vectors, following the directions $x_{1'}$ and $x_{2'}$ respectively, but expressed in the conventional rectangular coordinates $x_1 - x_2$. Thus, term (2) can be rewritten as:

$$\sum_{\xi_e^{e'} \in \mathcal{E}^{\mathcal{O}}} \int_{\xi_e^{e'}} (t_{1'}^{\xi_e^{e'}}, t_{2'}^{\xi_e^{e'}}) \begin{pmatrix} (\mathbf{u}_h^{e'} - \mathbf{u}_h^{e}) \cdot \mathbf{n}^{\xi_e^{e'}} \\ (\mathbf{u}_h^{e'} - \mathbf{u}_h^{e}) \cdot \boldsymbol{\tau}^{\xi_e^{e'}} \end{pmatrix} dS = \sum_{\xi_e^{e'} \in \mathcal{E}^{\mathcal{O}}} \int_{\xi_e^{e'}} (t_{1'}^{\xi_e^{e'}}, t_{2'}^{\xi_e^{e'}}) \underbrace{\begin{pmatrix} n_1^{\xi_e^{e'}} & n_1^{\xi_e^{e'}} \\ \tau_1^{\xi_e^{e'}} & \tau_1^{\xi_e^{e'}} \end{pmatrix}}_{\underline{\underline{M}}^{\xi_e^{e'}}} \begin{pmatrix} u_1^{e'} - u_1^{e} \\ u_2^{e'} - u_2^{e} \end{pmatrix} dS \tag{140}$$

To simplify the notation in the next expressions, the edge $\xi_e^{e'}$ will be denoted as ξ. Moreover, the interpolation of the displacements on the edge considered will be expressed as follows:

$$u_i^e(s) = u_i^{\alpha_1} N_1^{\xi}(s) + u_i^{\alpha_2} N_1^{\xi}(s); \qquad u_i^{e'}(s) = u_i^{\beta_1} N_1^{\xi}(s) + u_i^{\beta_2} N_1^{\xi}(s); \qquad i = 1:2 \tag{141}$$

Now, introducing in (140) the interpolations (61) for $\mathbf{t}_h$, and (141) for $\mathbf{u}_h^e$ and $\mathbf{u}_h^{e'}$, one has:

$$\int_{\xi} (t_{1'}^{1,\xi} N_1^{\xi} + t_{1'}^{2,\xi} N_2^{\xi}, t_{2'}^{1,\xi} N_1^{\xi} + t_{2'}^{2,\xi} N_2^{\xi}) \underline{\underline{M}}^{\xi} \begin{pmatrix} \left(u_1^{\beta_1} - u_1^{\alpha_1}\right) N_1^{\xi} + \left(u_1^{\beta_2} - u_1^{\alpha_2}\right) N_2^{\xi} \\ \left(u_2^{\beta_1} - u_2^{\alpha_1}\right) N_1^{\xi} + \left(u_2^{\beta_2} - u_2^{\alpha_2}\right) N_2^{\xi} \end{pmatrix} dS \tag{142}$$

Expanding (142), one obtains:

$$\begin{aligned} &(t_{1'}^{1,\xi}, t_{2'}^{1,\xi}) \underline{\underline{B}}_{11}^{\xi} \begin{pmatrix} u_1^{\beta_1} - u_1^{\alpha_1} \\ u_2^{\beta_1} - u_2^{\alpha_1} \end{pmatrix} + (t_{1'}^{1,\xi}, t_{2'}^{1,\xi}) \underline{\underline{B}}_{12}^{\xi} \begin{pmatrix} u_1^{\beta_2} - u_1^{\alpha_2} \\ u_2^{\beta_2} - u_2^{\alpha_2} \end{pmatrix} + \\ &(t_{1'}^{2,\xi}, t_{2'}^{2,\xi}) \underline{\underline{B}}_{12}^{\xi} \begin{pmatrix} u_1^{\beta_1} - u_1^{\alpha_1} \\ u_2^{\beta_1} - u_2^{\alpha_1} \end{pmatrix} + (t_{1'}^{2,\xi}, t_{2'}^{2,\xi}) \underline{\underline{B}}_{22}^{\xi} \begin{pmatrix} u_1^{\beta_2} - u_1^{\alpha_2} \\ u_2^{\beta_2} - u_2^{\alpha_2} \end{pmatrix}, \end{aligned} \tag{143}$$

where $\underline{\underline{B}}_{ij}^{\xi} = \underline{\underline{M}}^{\xi} \int_{\xi} N_i^{\xi} N_j^{\xi}\, dS$, for $i, j = 1:2$. Now, the local displacements have to be related to the global vector of displacements $\underline{\tilde{u}}_h$. This is done by means of two matrices, $\underline{\underline{A}}_1^{\xi}$ and $\underline{\underline{A}}_2^{\xi}$, of dimensions $(2, 6 \times E)$:

$$\begin{pmatrix} u_1^{\beta_1} - u_1^{\alpha_1} \\ u_2^{\beta_1} - u_2^{\alpha_1} \end{pmatrix} = \underline{\underline{A}}_1^{\xi} \underline{\tilde{u}}_h; \qquad \begin{pmatrix} u_1^{\beta_2} - u_1^{\alpha_2} \\ u_2^{\beta_2} - u_2^{\alpha_2} \end{pmatrix} = \underline{\underline{A}}_2^{\xi} \underline{\tilde{u}}_h. \tag{144}$$

Finally, doing the necessary algebra, (143) results in the following expression:

$$(\underline{\tilde{u}}_h)^T \underbrace{\left((\underline{\underline{A}}_1^{\xi})^T \quad (\underline{\underline{A}}_2^{\xi})^T\right) \begin{pmatrix} (\underline{\underline{B}}_{11}^{\xi})^T & (\underline{\underline{B}}_{12}^{\xi})^T \\ (\underline{\underline{B}}_{12}^{\xi})^T & (\underline{\underline{B}}_{22}^{\xi})^T \end{pmatrix}}_{\underline{\underline{A}}_{\xi}^{eq2}} \begin{pmatrix} t_{1'}^{1,\xi} \\ t_{2'}^{1,\xi} \\ t_{1'}^{2,\xi} \\ t_{2'}^{2,\xi} \end{pmatrix} = (\underline{\tilde{u}}_h)^T \underline{\underline{A}}_{\xi}^{eq2} \underline{t}_h^{\xi}. \tag{145}$$

Expression (145) gives the contribution of the edge $\xi_e^{e'}$ to the term (2). The last step is to sum over all the internal edges, as follows:

$$\sum_{\xi_e^{e'} \in \mathcal{E}^{\mathcal{O}}} (\underline{\tilde{u}}_h)^T \underline{\underline{A}}_{\xi_e^{e'}}^{eq2} \underline{t}_h^{\xi_e^{e'}} = (\underline{\tilde{u}}_h)^T \underline{\underline{\tilde{A}}}^{eq2} \underline{t}_h, \tag{146}$$

where $\tilde{\underline{\underline{A}}}^{eq2}$ is a $(6 \times E, 4 \times |\mathcal{E}^{\mathcal{O}}|)$ global matrix and $\underline{t}_h$ is a $4 \times |\mathcal{E}^{\mathcal{O}}|$ vector collecting the nodal tractions for each interior edge.

Finally, considering (138), (139) and (146), the discretization of the equilibrium constraint (137) takes the following form:

$$(\tilde{\underline{u}}_h)^T \tilde{\underline{\underline{A}}}^{eq1} \tilde{\underline{\sigma}}_h + (\tilde{\underline{u}}_h)^T \tilde{\underline{\underline{A}}}^{eq2} \underline{t}_h = \lambda (\tilde{\underline{u}}_h)^T \tilde{\underline{F}}_h^{\,eq}, \quad \forall \tilde{\underline{u}}_h \in Y_h^{UB}. \tag{147}$$

Since (147) must hold for all $\mathbf{u}_h$ in Y_h^{UB}, the displacement vector can be removed from the equation, thereby obtaining:

$$\tilde{\underline{\underline{A}}}^{eq1} \tilde{\underline{\sigma}}_h + \tilde{\underline{\underline{A}}}^{eq2} \underline{t}_h = \lambda \tilde{\underline{F}}_h^{\,eq}. \tag{148}$$

REFERENCES

1. Alizadeh F, Haeberly JA, Overton M. A new primal-dual interior point method for semidefinite programming. In *Proceed. Fifth SIAM Conf. Applied Linear Algebra* Lewis JG, editor. SIAM, Philadelphia, 1994; 113–117.
2. Anderheggen E, Knöpfel H. Finite element limit analysis using linear programming. *International Journal of Solids and Structures* 1972; **8**:1413–1431.
3. Andersen E. The MOSEK optimization tools version 3.0. User's manual and reference, 2002. *Available from http://www.mosek.com.* [April 2005]
4. Andersen KD, Christiansen E. Limit analysis with the dual affine scaling algorithm. *Journal of Computational and Applied Mathematics* 1995; **59**:233–243.
5. Andersen KD, Christiansen E. Minimizing a sum of norms subject to linear equality constraints. *Computational Optimization and Applications* 1998; **11**:65–79.
6. Andersen KD, Christiansen E, Overton ML. Computing limit loads by minimizing a sum of norms. *SIAM Journal on Scientific Computing* 1998; **19**(3):1046-1062.
7. Andersen KD, Christiansen E, Conn AR, Overton ML. An efficient primal-dual interior-point method for minimizing a sum of euclidian norms. *SIAM Journal on Scientific Computing* 2000; **22**(1):243–263.
8. Ben-Tal A, Nemirovski A. *Lectures on modern convex optimization: Analysis, algorithms and engineering applications*. SIAM: Philadelphia, 2001.
9. Capurso M. Limit analysis of continuous media with piecewise linear yield condition. *Meccanica - Journal of the Italian Association for Theoretical and Applied Mechanics* 1971; **6**:53–58.
10. Christiansen E. Computation of limit loads. *International Journal for Numerical Methods in Engineering* 1981; **17**:1547–1570.
11. Christiansen E. Limit analysis of collapse states. In *Handbook of Numerical Analysis, vol (4)* Ciarlet PG, Lions JL (eds). North-Holland: Amsterdam, 1996; 193–312.
12. Christiansen E, Andersen KD. Computation of collapse states with von Mises type yield condition. *International Journal for Numerical Methods in Engineering* 1999; **46**:1185–1202.
13. Christiansen E, Kortanek KO. Computation of the collapse state in limit analysis using the LP primal affine scaling algorithm. *Journal of Computational and Applied Mathematics* 1991; **34**:47–63.
14. Christiansen E, Pedersen OS. Automatic mesh refinement in limit analysis. *International Journal for Numerical Methods in Engineering* 2001; **50**(6):1331–1346.
15. Ciria H. *Computation of upper and lower bounds in limit analysis using second-order cone programming and mesh adaptivity*. M.S. thesis 2004 (May), Massachusetts Institute of Technology, Cambridge, MA 02139.
16. Ciria H., Peraire J., *Computation of upper and lower bounds in limit analysis using second-order cone programming and mesh adaptivity*, *9th ASCE Special Conference on Probabilistic Mechanics and Structural Reliability*, Alburquerque, 2004.
17. Helmberg C, Rendl F, Vanderbei RJ, Wolkowicz H. An interior-point method for semidefinite programming.*SIAM J. Optimization* 1996; **6**:342–361.
18. Karmarkar N. A new polynomial-time algorithm for Linear Programming. *Combinatorica* 1984; **4**:373–395.
19. Krabbenhoft K, Damkilde L. A general non-linear optimization algorithm for lower bound limit analysis. *International Journal for Numerical Methods in Engineering* 2003; **56**:165–184.
20. Krabbenhoft K, Lyamin AV, Hjiad Mhd, Sloan SW, A new discontinuous upper bound formulation, *International Journal for Numerical Methods in Engineering* 2005; **63**:1069–1088.
21. Lubliner J. *Plasticity Theory*. Macmillan Publishing Company: New York, 1990.
22. Lyamin AV, Sloan SW. Lower bound limit analysis using non-linear programming. *International Journal for Numerical Methods in Engineering* 2002; **55**:573–611.

23. Lyamin AV, Sloan SW. Upper bound limit analysis using linear finite elements and non-linear programming. *International Journal for Numerical and Analytical Methods in Geomechanics* 2002; **26**:181–216.
24. Maier G. A matrix structural theory of piecewise-linear plasticity with interacting yield planes. *Meccanica* 1970; **5**:55–66.
25. Makrodimopoulos A., Martin C.M., Lower bound limit analysis of cohesive-frictional materials using second order programming, *Int. J. Num. Meth. Engrg.* **66**(4), 2006, pp. 604–634.
26. Makrodimopoulos A., Martin C.M., Upper bound limit analysis of cohesive-frictional materials using second order programming, Technical Report OUEL 2288/05, Department of Engineering Science University of Oxford, 2005.
27. Nesterov Y, Nemirovskii A. *Interior point polynomial algorithms in convex programming.* SIAM: Philadelphia, 1994.
28. Nesterov Y, Todd MJ. Self-scaled barriers and interior point methods for convex programming. *Mathematics of Operations Research* 1997; **22(1)**:1–42.
29. Rivara MC. Algorithms for refining triangular grids suitable for adaptive and multigrid techniques .*International Journal for Numerical Methods in Engineering* 1984; **20**:745–756.
30. Sturm JF. Using SeDuMi 1.02, a Matlab toolbox for optimization over symmetric cones (Updated for version 1.05), 2001. *Available from http://fewcal.kub.nl/∼sturm* [April 2005].
31. Tütüncü RH, Toh KC, Todd MJ. SDPT3 - a MATLAB software package for semidefinite-quadratic-linear programming, version 3.0, 2001. *Available from http://www.math.cmu.edu/∼reha/sdpt3.html* [April 2005].